Forschungszentrum Karlsruhe

in der Helmholtz-Gemeinschaft

Wissenschaftliche Berichte

FZKA 6739

On the thermo-physical properties of Zircaloy-4 and ZrO_2 at high temperatures

Part 1: Experimental and modelling results on cool-down of Zircaloy-4 rods in various atmospheres. Thermal and thermo-mechanical effects

J. Stuckert, M. Steinbrück, U. Stegmaier

Institut für Materialforschung

Part 2: Determination of Zircaloy and ZrO_2 emissivities using experimental data of empty rods cool-down tests

A. V. Palagin

Nuclear Safety Institute
Russian Academy of Science, Moscow

Forschungszentrum Karlsruhe GmbH, Karlsruhe
2002

Impressum der Print-Ausgabe:

Als Manuskript gedruckt

Forschungszentrum Karlsruhe GmbH
Postfach 3640, 76021 Karlsruhe

Mitglied der Hermann von Helmholtz-Gemeinschaft
Deutscher Forschungszentren (HGF)

ISSN 0947-8620

Abstract

Results of thirty separate-effects tests recently performed within the scope of the QUENCH Program are presented. The aim of the work was the validation of heat transfer and oxidation modules of the SVECHA/QUENCH code, which was developed for the detailed description of fuel rod quenching. The influence of the different gas mixtures in the gas channel on the temporal temperature development of the cladding tube surface was investigated. The results of these tests allow also the calculation of the emissivity of metallic as well as oxidised Zircaloy tube surface.

Untersuchung der thermophysikalischen Eigenschaften von Zircaloy-4 und ZrO_2 bei hohen Temperaturen

Zusammenfassung

Es werden die Resultate der neuen dreißig Einzeleffekttests innerhalb des QUENCH-Programms dargestellt. Das Ziel der Arbeit war die Validierung des Wärmeübertragungsmoduls und des Oxidationsmoduls des SVECHA-Codes, der für die detaillierte Beschreibung des Abschreckens von Brennstäben entwickelt wurde. Es wurde der Einfluss der unterschiedlichen Gasmischungen in der Gasführung auf die zeitliche Temperaturentwicklung der Hüllrohroberfläche untersucht. Die Resultate dieser Versuche haben auch die Bestimmung der Emissivität der metallischen und der oxidierten Rohroberfläche ermöglicht.

Content

Part 1: Experimental and modelling results on cool-down of Zircaloy-4 cladding in various atmospheres. Thermal and thermo-mechanical effects

List of Tables

List of Figures

1. Introduction

The exact description of gas mixture properties, the cladding surface emissivity properties and thermo-mechanical properties of cladding is very important for the modeling of the cladding tube behavior at high temperatures. A series of 30 cool-down tests in inert, oxidising and hydrogen-containing atmospheres were performed in order to improve the understanding of the phenomena and to deliver data for modeling.

2. Experimental facility and procedure

The experimental facility (Fig. 1) used for the cool-down tests was the FZK Quench rig [1]. The empty rod specimen of a length of 150 mm (in the case of tests with non-oxidised Zry cladding tube) or 105 mm (in the case of tests with oxidised Zry cladding tube) was suspended inside a quartz tube. The initial diameter of the rod specimen is 10.75 mm, the initial cladding thickness 0.725 mm. The specimen was suspended by a thin Zry capillary tube inside a quartz tube (non-oxidised Zry tube) or by a solid Zry rod (oxidised Zry cladding tube). Heating was provided by an induction coil around the section of the quartz tube. Power was supplied to the coil from a 20 kW generator, at a frequency of 700 kHz, which induced currents in the bulk of the metal with consequent Joule heating. The feedback regulation of generator was performed by means of a pyrometer, focused on the specimen surface at the center of the rod.

The test matrix is shown in Table 1.

In the case of tests without oxidation (Fig. 2) the Zry rod was heated up to the temperature 1200°C (measured by the TC located at the outer surface in the middle of the rod; temperature at the upper and lower ends was smaller by 50-100 K), kept at this temperature for 60 seconds and, after switching off the power, cooled down in gas flow on the following compositions: pure argon, pure helium, argon+hydrogen mixture and helium+hydrogen mixture.

In the case of tests with oxidation the Zry rod was oxidised at the temperatures between 1300-1500°C during different time intervals in argon+oxygen mixture under oxygen partial starvation conditions (30+6 l/h for the first series and 20+20 l/h for the second series) with resulting oxide thicknesses from 4 µm to 40 µm (first oxidation test series) and from 60 µm to 600 µm (second oxidation test series). The Zry rod was cooled down after switching off the power without changing the gas mixture. The Zry tubes were hermetically sealed in the first test series and had a hole of 1 mm diameter at the bottom in the second series.

The temperature of the rod outer surface was continuously measured. In the case of non-oxidised rod tests three Pt/Rh TCs located at 20 mm (TCl), 75 mm (TCm) and 130 mm (TCu) elevations were used; TCs were insulated from metallic cladding surface by means of a thin Rhenium foil.

In the case of oxidised rod tests one TC located in the middle of the rod (52 mm) was used. The specimens had been pre-oxidised to a small extent to prevent eutectic interactions between thermocouples and cladding surface before the tests. This thin oxide scale was also formed in the QUENCH rig by exposing specimens at 1000°C in argon+oxygen (40+10 l/h or 0.02+0.004 g/s) flow for one minute. The resulting protection oxide layer thickness was ~10 µm.

The off-gas composition was measured by a “Balzers GAM-300” mass spectrometer (MS). GAM-300 is a completely computer-controlled quadrupole MS with 8 mm rod

system which allows quantitative measurements of gas concentrations as low as about 10 vppm. The main task of the MS was to measure the hydrogen rate in the off-gas.

3. Experimental and modeling results

3.1. Cool-down tests with non-oxidised rods

The cool-down process was recorded by a video system. The different records were synchronised after the tests with the help of special software. Three different frame sequences from the tests in argon, argon+hydrogen and helium+hydrogen were combined in one film (Fig. 3), allowing to compare the cool-down process in the different gas mixtures. As one can see from this film, the presence of hydrogen in the flowing gas mixture led to a delay of the rod cooling due to exothermal absorption of hydrogen by zirconium. The hot region on the rod surface (visible by its bright color) moved upwards along the rod following the movement of hydrogen absorption rate maximum.

Fig. 4 – Fig. 5 show the thermocouples readings during the cool-down period for the rods filled with pellets. The comparison of the temperature curves (Fig. 6) in the pure inert gas with the temperature curves in Ar+H_2 and He+H_2 mixtures clearly shows a delay of cooling because of the hydrogen absorption influence. The comparison of the middle thermocouples readings (Fig. 7) shows, that in the gas mixture with argon the cooling process is slower than that in helium mixture. This can be explained by the lower thermal conductivity of argon in comparison with helium.

A number of tests on cool-down of empty Zircaloy rods in hydrogen-containing gas mixtures were performed for a better understanding of the exothermic influence of the hydrogen uptake by zirconium (Fig. 8 – Fig. 11). The increase of the hydrogen solubility with decreasing temperature causes a delay of the cool-down process and even a temperature increase during the cool-down phase in helium+hydrogen atmosphere (Fig. 12). The fast cooling in helium-containing atmosphere provides better conditions for a quick hydrogen local absorption in comparison with cool-down in the argon-containing atmosphere. Therefore, almost all injected hydrogen is consumed in the lower part of the rod. That causes the local warm-up only in the lower part of the rod in the helium-hydrogen atmosphere. The rod in argon-hydrogen mixture absorbs the hydrogen axially more homogeneously and thus cools more slowly. This fact leads to bigger total absorption of H2 in the whole rod. The hydrogen starvation causes a movement of the hot zone upwards along the rod.

The hydrogen flow at the outlet was measured during the tests with the mass spectrometer (Fig. 13 – Fig. 16). The difference between the measured hydrogen mass and injected one is the absorbed mass of hydrogen. These values of total absorbed hydrogen are between ~35 at% for the cool-down in helium+hydrogen atmosphere and ~45 at% for the cool-down in argon+hydrogen atmosphere. This large quantity of absorbed hydrogen causes extreme high brittleness of the material: at the end of the cool-down phase the Zircaloy capillary tubes broke under the weight of the rod, the rods fell down and brocked (Fig. 17 – Fig. 18).

3.2. SVECHA-modelling of the Zircaloy rod tests on the cool-down in the inert gas-hydrogen atmosphere

The tests described above provide a good experimental base for the verification of the mechanistical SVECHA-code, which was developed for the description of single rod quench phenomena [4]. Fig. 19 shows the comparison of test and modelling results for three cases – cool-down in argon, argon-hydrogen, and helium-hydrogen atmospheres. The comparison of the curves for the argon atmosphere shows the perfect correspondence between experimental and model results. But, for the cool-down in the hydrogen-containing gas mixture one can see only a qualitative presentation of the cool-down delay due to the exothermal hydrogen absorption. The possible explanation of that deviation from the test results can be the underestimation of the convection in the gas channel: for modelling the cool-down processes in the gas mixture the Nusselt number from the tests on the cool-down in the pure argon was used.

3.3. Cool-down tests with oxidised rods

A number of tests was performed in argon-oxygen atmosphere for the investigation of the cool-down processes for rods with oxidized surface. Hermetically sealed rods with air atmosphere inside were used for the first test series (Fig. 20 – Fig. 22). There were no experimental problems during the tests below 1400°C. But the first test at the 1400°C led to unexpected results: the rod collapsed after the temperature of 1400°C was reached (Fig. 23). An explanation is the exhaustion of oxygen and nitrogen from the inner atmosphere because of their absorption by zirconium during the warm-up. The plasticity of Zircaloy at 1400°C is relatively high, and the tube is no longer withstand the pressure difference of 1 bar.

Therefore, unsealed rods were used to prevent the collapse. Five tests at different temperatures and different oxidation phases were performed with these rods (Fig. 24 – Fig. 27).

The beginning of the oxidation shows no exothermal effect by the reaction between oxygen and zirconium because of the high radiation heat losses through the quartz glass in the QUENCH rig.

Fig. 28 shows a comparison of the cool-down curves. The temperature lines of the various tests are shifted to each other start from a reference temperature point (1330°C). One can see that the tubes with the oxide layer thickness with more than 100 µm cool slower than the tubes with the thinner oxide layer. The cool-down curves for the samples with the oxide layer thickness 60, 70 and 105 µm practically coincide with each other. I. e., the thermal resistivity of the oxide layer up to the thickness of 100 µm has small effect on the rod behaviour under cool-down conditions.

Fig. 29 compares the cool-down of the oxidised tubes in the $Ar+O_2$ gas mixture with the cool-down of unoxidised tubes in the inert gases. One can see that despite of the high thermal conductivity of helium the oxidised rod in argon-oxygen atmosphere cools faster than the pure metallic sample in the helium atmosphere. The explanation of this fact is the higher emissivity of the oxidized surface.

Fig. 30 – Fig. 31 present the results of metallographic investigations of cladding cross-sections. The measured oxide layer thicknesses were used for comparison with SVECHA-modeling results. One can note the typical effects of the Zircaloy oxidation. Firstly, the segregation of the oxide in the two sub-layers because of the

not fully understood mechanism of the tin redistribution. One can see this process with the formation of circumferential cracks between the sub-layers at the cross-section of the cladding from the test 2805015. Such kind of the segregation wasn't seen at the quench tests with the Zr-Nb claddings [5]. Secondly, the formation of the substoichiometric cubic oxide layer, which is formed at temperatures higher than ~1520°C was observed. The cubic phase disintegrates during cool-down into two phases: tetragonal ZrO_2 and metallic α-Zr(O). One can also note the absence of the cladding through-wall cracks, which are typical for the quenching of oxidized cladding [6].

3.4. SVECHA-modelling of the Zircaloy rod tests on the cool-down in oxidising atmosphere

For tests 2805011-2805015 corresponding SVECHA calculations were performed. The power profiles were chosen so that the resulting temperature profiles correspond to the test temperature profiles. The results of these calculations are summarised in Table 3.

Fig. 32 shows that for the case of a cladding surface oxidation at temperatures lower than 1500°C and with a relative thin resulting oxide layer of <100 µm the calculation and test results coincide well.

Modelling of the tests with the cladding surface temperature above 1500°C and with an oxide layer thickness of ~100 µm gives some overestimation of the layer thickness (Fig. 33). The analysis of the modelled radial oxygen distribution in the cladding at the onset of cool-down shows that the model overestimates the growth of the cubic ZrO_{2-x} phase (Fig. 33 - Fig. 34). Furthermore, the appearance of the thick cubic ZrO_{2-x} phase (Fig. 36) is erroneously calculated for the test with a surface temperature slightly higher than 1400°C (Fig. 35). The test shows no formation of such phase at all. The situation is reverse for the thick oxide layer of the test with oxidation temperature above 1500°C (Fig. 37): the calculated oxide layer thickness is underestimated. The analysis of the calculated radial oxygen distribution at the onset of the cool-down (Fig. 38) shows the strong underestimation of the thickness of the cubic phase layer.

The reason of such deviations of modelling results from the test results could be that a very rough experimental correlation for the oxygen diffusion coefficient in the cubic oxide phase is used in the model. Also, the thermodynamic parameters, e.g. the thermal conductivity of the oxide layer at temperatures above 1500°C, are not exactly known. An experimental database for this temperature region is practically unavailable [7].

3.5. Measurements of the specific heat and thermal conductivity of Zry–4

For the description of the physical properties of the cladding tube the SVECHA model uses data from the MATPRO database [7]. The dependence of the specific heat capacity of Zircaloy on the temperature in this database is essentially based on measurements for Zry-2. Therefore, the measurement of this dependence for Zry-4 was necessary. Such measurement was performed in detail with the help of the thermoanalytical device NETZSCH DSC 404. A Zircaloy-4 disc (diameter 4.96 mm, thickness 2.04 mm) was heated with a rate of 0.33 K/s. The temperature step during the measurement was 10 K. The result of the measurement is shown in Fig. 40. A comparison with Zry-2 data shows some curve shifting in the phase transition region.

To verify the thermal conductivity data of Zircaloy the thermal diffusivity of Zry-4 was measured. The measurement was performed with a laser flash diffusivity apparatus and a Zry-4 disc sample (Fig. 41). The thermal conductivity is the product of measured thermal diffusivity, measured specific heat capacity, and density of the material. The result of this calculations is shown in Fig. 42. A comparison of these data with data from former measurements [8] shows satisfactory agreement.

4. General conclusions

- Thirty cool-down tests with fuel rod simulators for the verification of the SVECHA-code have been performed in different gas mixtures with cool-down onset temperatures between 1200°C and 1600°C. Five gas mixtures were used: argon, helium, argon + hydrogen, helium + hydrogen, argon + oxygen.

- The cool-down process, which was recorded by a video system, shows the influence of the hydrogen: there is a delay of the cool-down because of exothermic uptake of hydrogen by zirconium. The hydrogen starvation results in the formation of the hot zone, which moves upwards along the rod.

- The axial hydrogen distribution in the cladding tube is inhomogeneous and depends on the gas mixture in the channel. The total hydrogen amount, which was dissolved in Zircaloy rod, is between 330 mg (gas mixture with helium) and 500 mg (gas mixture with argon) leading to mean hydrogen concentrations in the specimens of 35 at% and 45 at%, respectively.

- The Zircaloy cladding tube collapsed at 1400°C due to the exhaustion of oxygen and nitrogen from the inner atmosphere because of their absorption by zirconium during the warm-up.

- The exact description of the gas mixture properties in the channel is very important for modeling the cladding tube behavior at high temperatures, especially the convection in the gas (Nusselt number). The SVECHA-code simulates well the cool-down process in the inert gas, but the simulation is not satisfactory for gas mixtures “inert gas + hydrogen” and “inert gas + oxygen”.

- The SVECHA-code simulation shows good results for the formation of oxide layers by the oxidation at the temperatures up to 1450°C measured at the outer surface of the cladding. The simulated oxide layer thickness at the oxidation temperature above 1450°C is not satisfactory because of insufficient knowledge of oxygen diffusion coefficients in the cubic ZrO_{2-x} phase.

- The specific heat capacity and thermal conductivity of Zircaloy-4 were measured for temperatures between 500°C and 1100°C.

Acknowledgements

The authors thank Dr. M. Rohde and Ms. P. Willing for the conduct of the measurements of thermodynamic and transport properties of Zircaloy-4.

We are very grateful to Mr. L. Sepold for the careful review of the manuscript.

References

1. P. Hofmann, V. Noack, M.S. Veshchunov, A.V. Berdyshev, A.V. Boldyrev, L.W. Matweev, A.V. Palagin, V.E. Shestak. Physico-chemical Behavior of Zircaloy Fuel Rod Cladding Tubes during LWR Severe Accident Reflood. FZKA 5846, May 1997
2. P. Hofmann, A. Miassoedov, L. Steinbock, M. Steinbrück, A.V. Berdyshev, A.V. Boldyrev, A.V. Palagin, V.E. Shestak, M.S. Veshchunov. Quench Behavior of Zircaloy Fuel Rod Cladding Tubes. Small-Scale Experiments and Modelling of the Quench Phenomena. FZKA 6208, March 1999
3. TAPP Database, Version 2.2, E. S. Microware, Hamilton, OH, 1996
4. A.V. Berdyshev, A.V. Boldyrev, A.V. Palagin, V.E. Shestak, M.S. Veshchunov, SVECHA/QUENCH Code for the Modeling of Reflooding Phenomena in Severe Accidents Conditions. Proceedings of the Ninth International Topical Meeting on Nuclear Reactor Thermal Hydraulics (NURETH-9), paper Log_19 (CD-ROM edition), San Francisco, California, 1999
5. J. Stuckert, M. Steinbrück, U. Stegmaier. Single rod Quench tests with Zr-1Nb cladding. Comparison with Zircaloy-4 cladding tests and modelling. Wissenschaftliche Berichte, FZKA-6604, Karlsruhe, Juni 2001
6. L. Steinbock, J. Stuckert. Determination of the crack pattern of quenched Zircaloy tubes. Wissenschaftliche Berichte, FZKA-6013, Karlsruhe, November 1997
7. L. J. Siefken, E. W. Coryell, E. A. Harvego. J. K. Hohorst, S.A. Arndt. MATPRO – A Library of Materials Properties for Light-Water-Reactor Accident Analysis. NUREG/CR-6150, Vol. 4, Rev. 2. INEL-96/0422. Washington, January 2001
8. International Nuclear Safety Center (INSC) Material Properties Database. October 1999 (http://www.insc.anl.gov/matprop/#prop)

test	ZrO_2 pellets	onset of cool-down, °C	isolation of TC	emissivity preset	H_2 or O_2 supply duration before cool-down, s	gas mixture during cool-down
10221a	yes	1200	Re foil	0.4	200	Ar(102l/h)
10221b	yes	1200	Re foil	0.4	200	Ar(102l/h)
10221c	yes	1200	Re foil	0.4	650	Ar(45l/h)+H_2(45l/h)
10222a	no	1200	Re foil	0.4	50	Ar(102l/h)
10222b	no	1200	Re foil	0.4	50	Ar(102l/h)
10222c	no	1200	Re foil	0.4	860	Ar(45l/h)+H_2(45l/h)
10223a	yes	1200	Re foil	0.4	150	He(102l/h)
10223b	yes	1200	Re foil	0.4	150	He(102l/h)
10223c	yes	1200	Re foil	0.4	670	He(45l/h)+H_2(45l/h)
10223d	no	1200	Re foil	0.4	150	He(102l/h)
10223e	no	1200	Re foil	0.4	150	He(102l/h)
10223f	no	1200	Re foil	0.4	540	He(45l/h)+H_2(45l/h)
10301a	no	1200	Re foil	0.4	80	Ar(102l/h)
10301b	no	1200	Re foil	0.4	80	Ar(102l/h)
10301c	no	1200	Re foil	0.4	610	Ar(45l/h)+H_2(45l/h)
10301d	no	1200	Re foil	0.4	80	He(102l/h)
10301e	no	1200	Re foil	0.4	80	He(102l/h)
10301f	no	1200	Re foil	0.4	560	He(45l/h)+H_2(45l/h)
150501	no	1400	no	0.25	20+3*	Ar(30l/h)+O_2(6l/h)
160501	no	1400	Re foil	0.4	25+3*	Ar(30l/h)+O_2(6l/h)
1705011	no	1300	Re foil	0.4	25+3*	Ar(30l/h)+O_2(6l/h)
1705012	no	1400	Re foil	0.4	26+3*	Ar(30l/h)+O_2(6l/h)
1805010	no	1400	Re foil	0.4	50	Ar(30l/h)
1805011	no	1300	Re foil	0.4	85+3*	Ar(30l/h)+O_2(6l/h)
1805012	no	1300	Re foil	0.4	85+3*	Ar(30l/h)+O_2(6l/h)
2805011	no	1400	pre-oxide#	0.7	50+60**	Ar(20l/h)+O_2(20l/h)
2805012	no	1330	pre-oxide#	0.7	50+60**	Ar(20l/h)+O_2(20l/h)
2805013	no	1600	pre-oxide#	0.7	360+60**	Ar(20l/h)+O_2(20l/h)
2805014	no	1500	pre-oxide#	0.7	60+60**	Ar(20l/h)+O_2(20l/h)
2805015	no	1400	pre-oxide#	0.7	1320+60**	Ar(20l/h)+O_2(20l/h)

* 3 s – duration of oxygen supply during the cool-down phase (for all other tests the gas mixture was constant during the cool-down)

\# pre-oxidation at 1000°C during 1 min. in O_2 (10 l/h) + Ar (40 l/h)

** 60 s transient phase from 1000°C

Table 1. Test matrix

test	tube surface	tube weight gain, mg	mass-spectr. absorbed hydrogen, mg	oxide layer thickness μm	α-Zr(O) layer thickness μm
10221a	metallic				
10221b	metallic				
10221c	metallic				
10222a	metallic				
10222b	metallic				
10222c	metallic	>460[#]	500 (44at%)		
10223a	metallic				
10223b	metallic				
10223c	metallic				
10223d	metallic				
10223e	metallic				
10223f	metallic		370 (37at%)		
10301a	metallic				
10301b	metallic				
10301c	metallic		490		
10301d	metallic				
10301e	metallic				
10301f	metallic		330		
150501	grey oxide	43		4	11
160501*	grey oxide	<90			
1705011	grey oxide	69		11	39
1705012*	grey oxide				
1805010*	metallic				
1805011	grey oxide	195		41	33
1805012	grey oxide	196			
2805011	grey oxide	426		71	83
2805012	grey oxide	375		58	85
2805013	white oxide			123	446
2805014	grey oxide	598		106	103
2805015	white oxide			298	513

[#] - for comparison: cladding tube mass is 26.811 g
* - collapse of cladding tube

Table 2. Post-test appearance

test	onset of cool-down, °C	const. temperature duration before cool-down, s	oxide layer thickness meas., μm	oxide layer thickness SVECHA, μm	α-Zr(O) layer thickness meas., μm	α-Zr(O) layer thickness SVECHA, μm
2805011	1400	50	71	65	83	86
2805012	1330	50	58		85	
2805013	1600	360	123	320	446	490
2805014	1500	60	106	118	103	137
2805015	1400	1320	298	528	513	381

Table 3. Comparison of the experimental results for oxidised rods with the results of corresponding SVECHA calculations.

Test on the cool-down in oxidising gas mixture (20l/h argon + 20l/h oxygen)

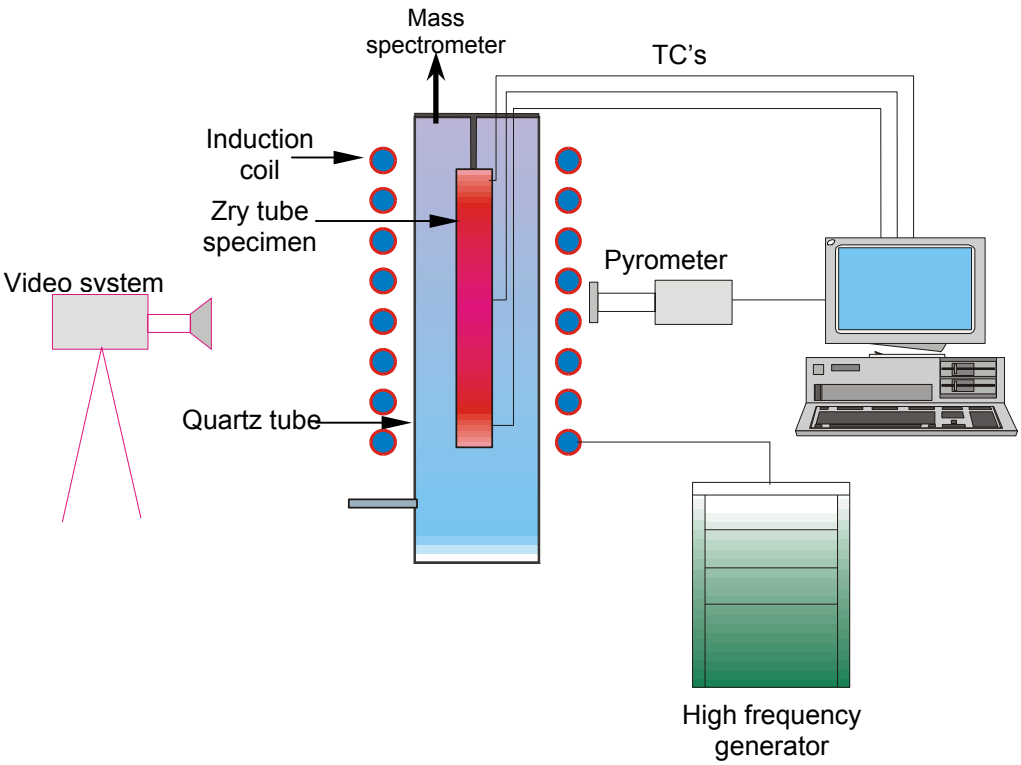

Fig. 1: Test facility

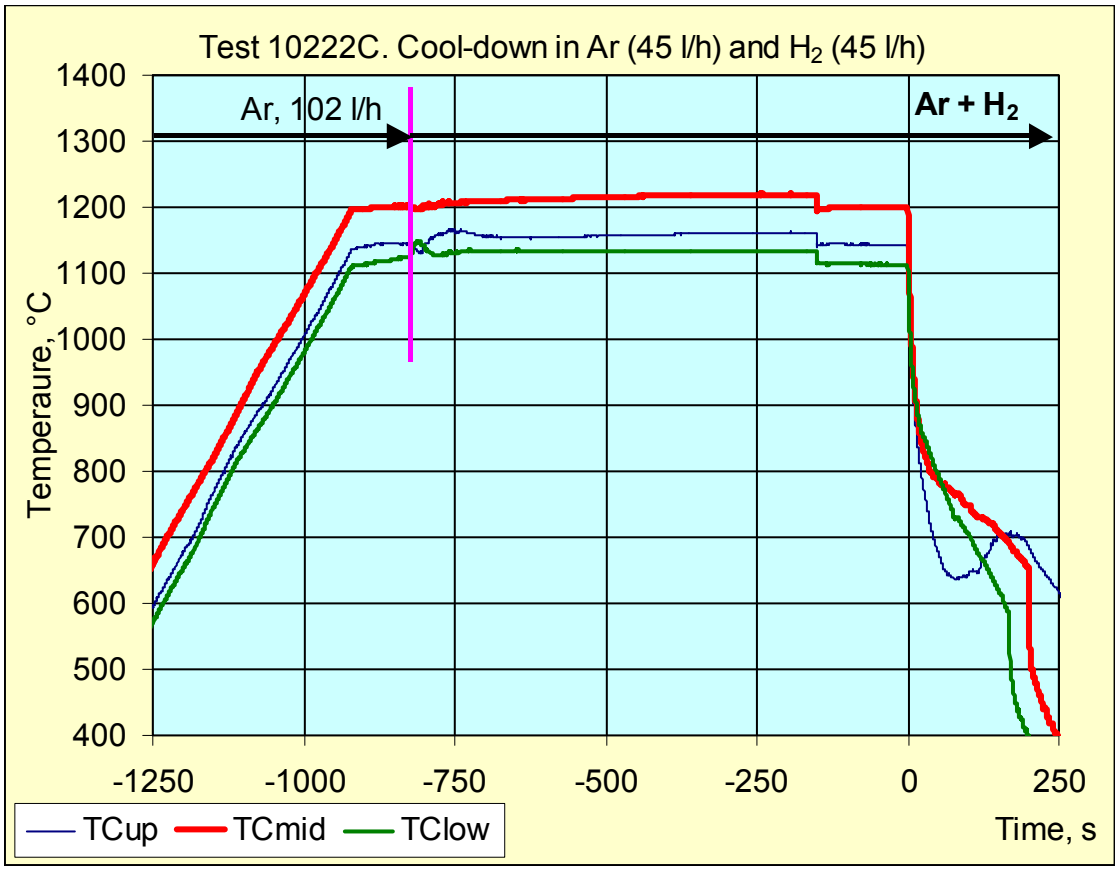

Fig. 2: Typical test conduct

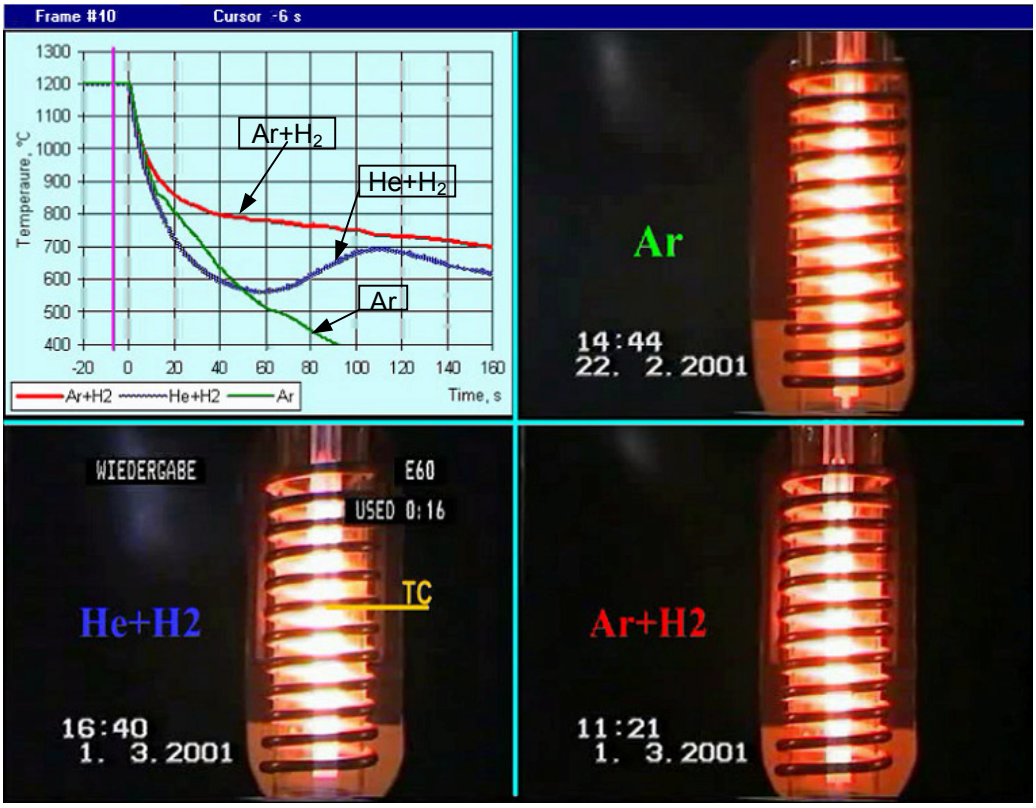

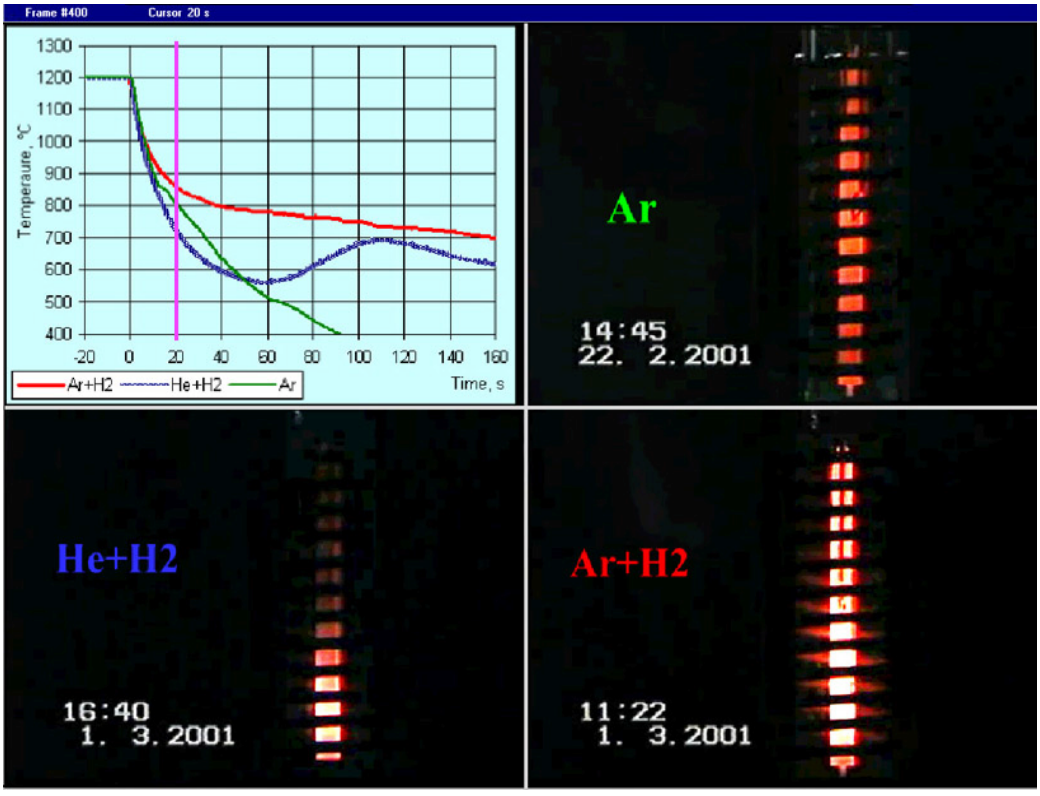

Fig. 3: Cooldown behavior in different atmospheres (two frames of the video film are given).

An inhomogeneous axial temperature distribution is caused by an exothermic hydrogen absorption

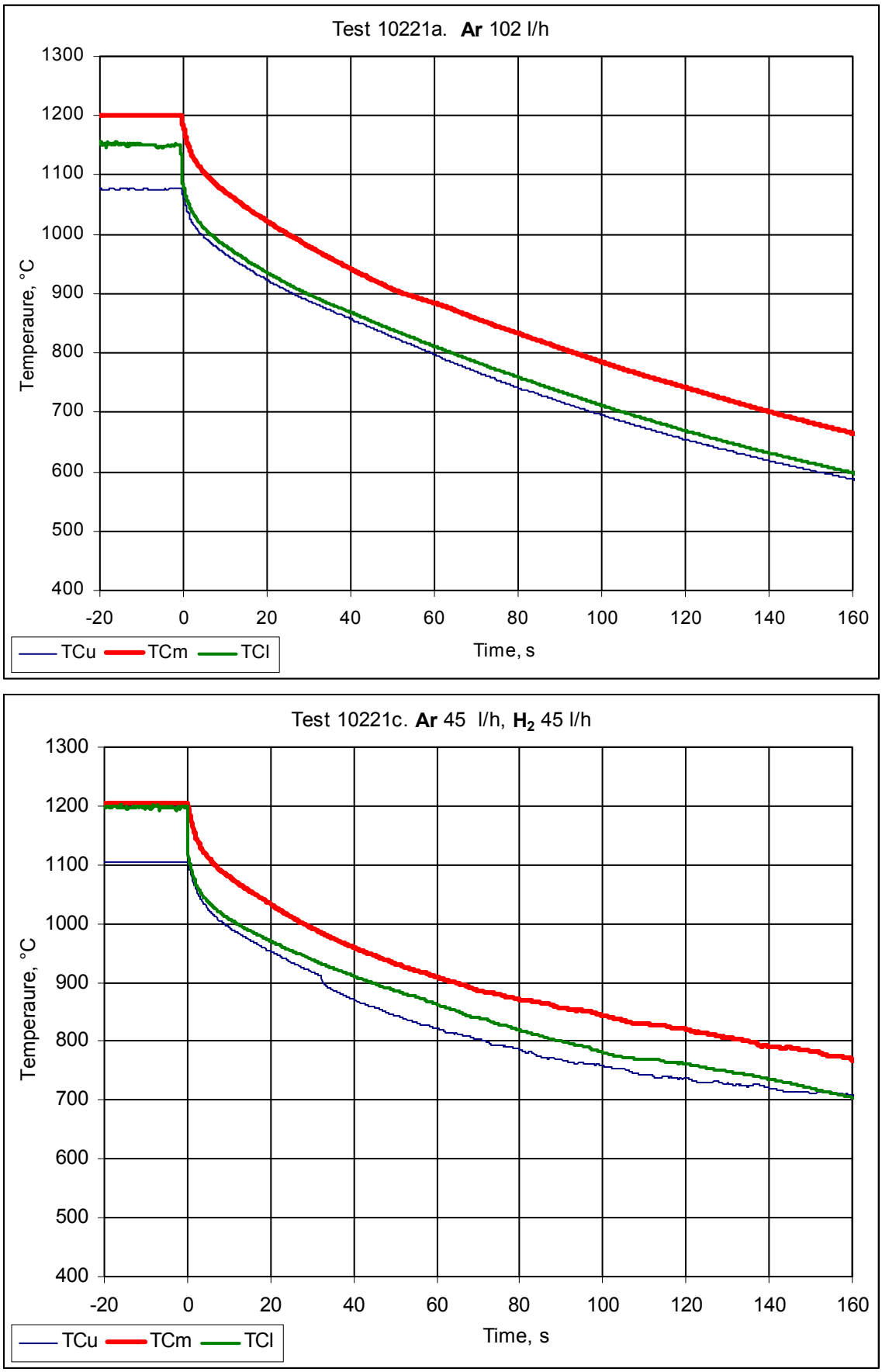

Fig. 4: Cool-down of a Zry-tube with ZrO_2 pellets in the Ar and Ar+H_2 gas mixture.

TCu → 130 mm, TCm → 75 mm, TCl → 20 mm

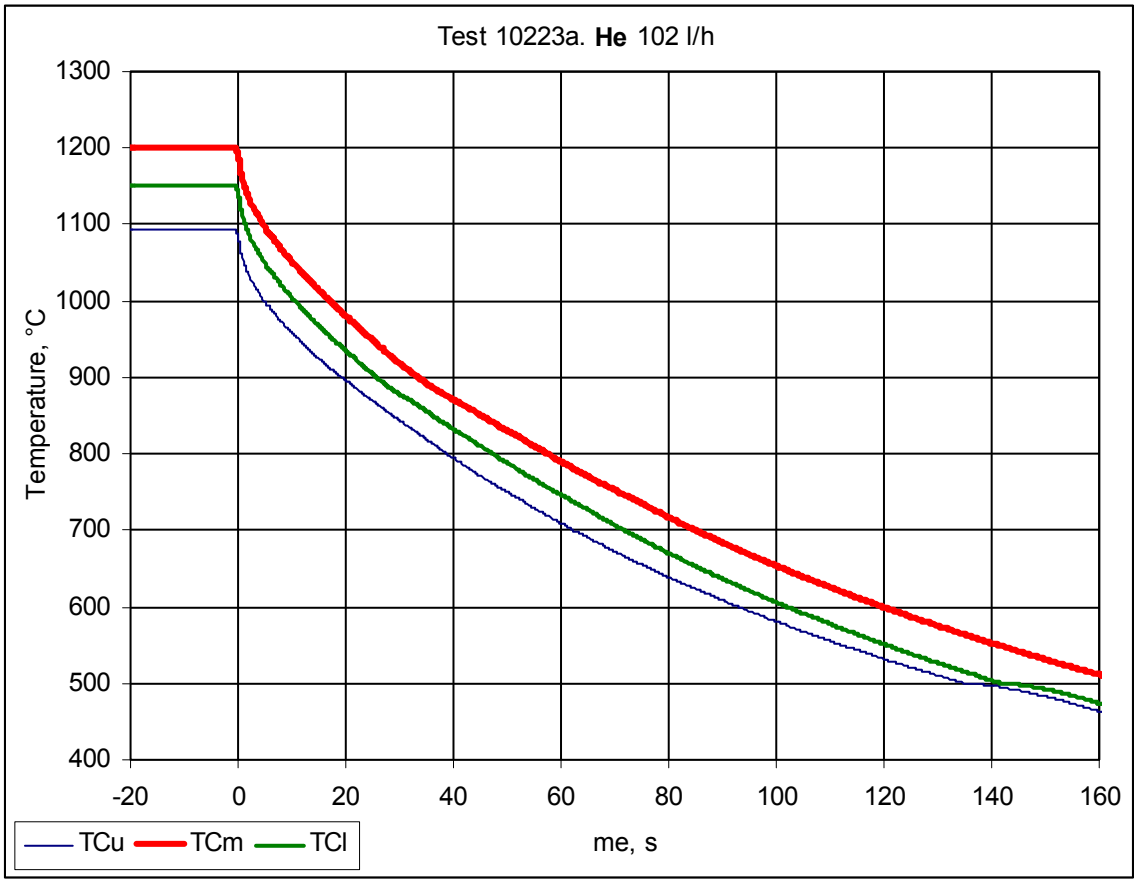

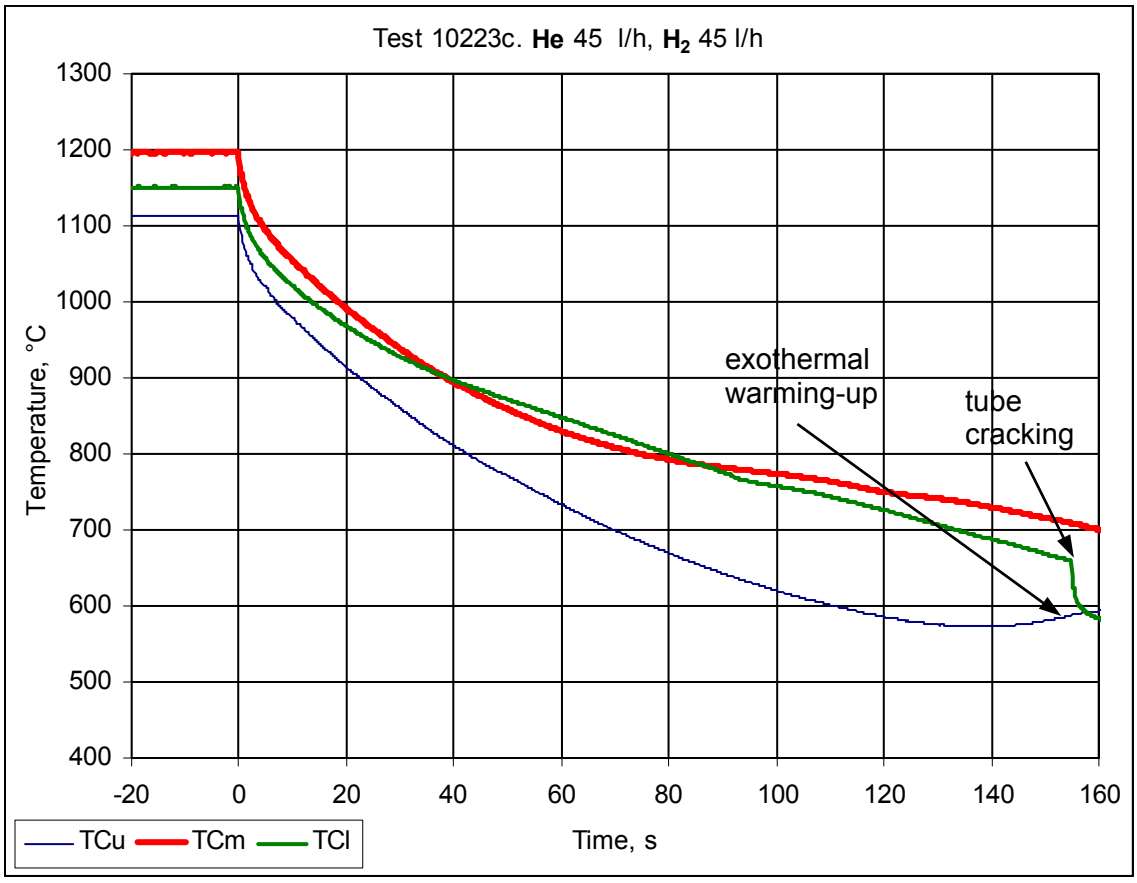

Fig. 5: Cool-down of a Zry-tube with ZrO_2 pellets in He and He+H_2 gas mixture.

TCu → 130 mm, TCm → 75 mm, TCl → 20 mm

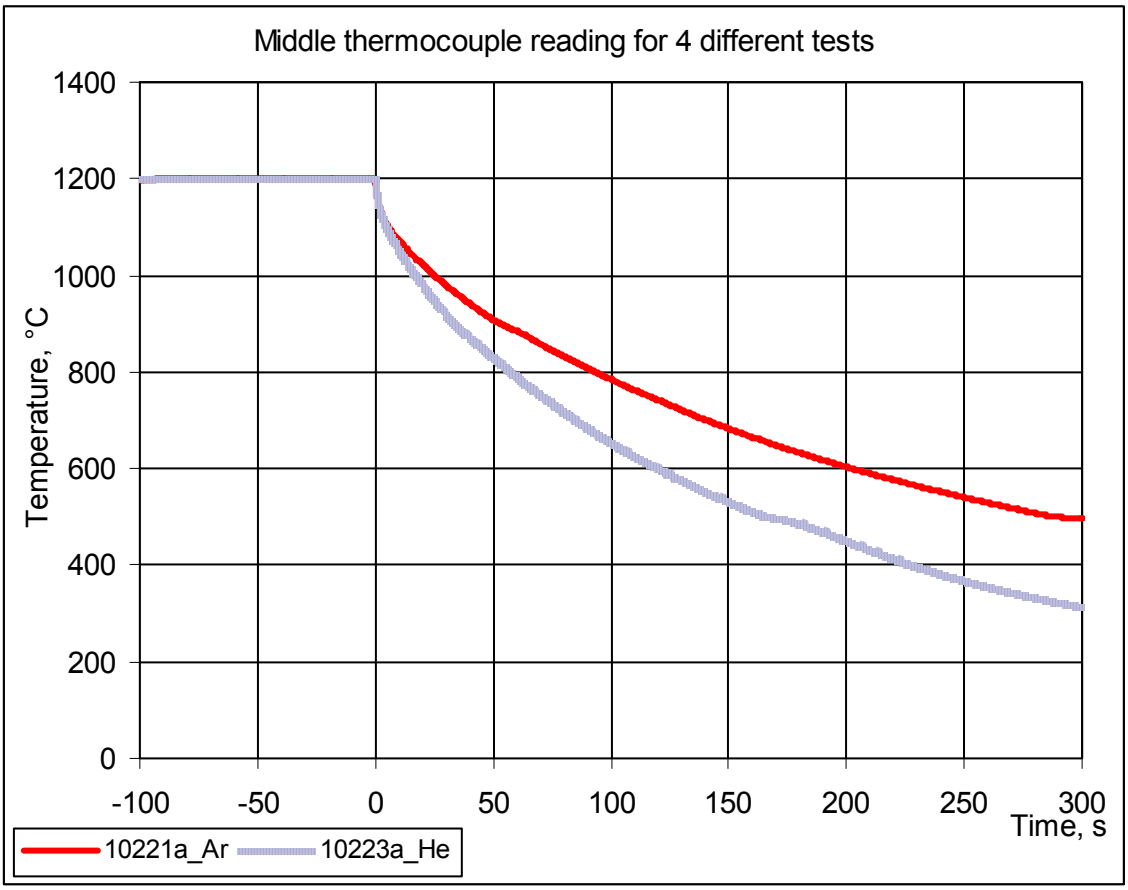

Fig. 6: Comparison of cool-down tests for two different inert gases.

The rod in He atmosphere cools faster because of higher thermal conductivity of He (430 mW/(m*K) at 1000°C) in comparison to Ar (49 mW/(m*K) at 1000°C)

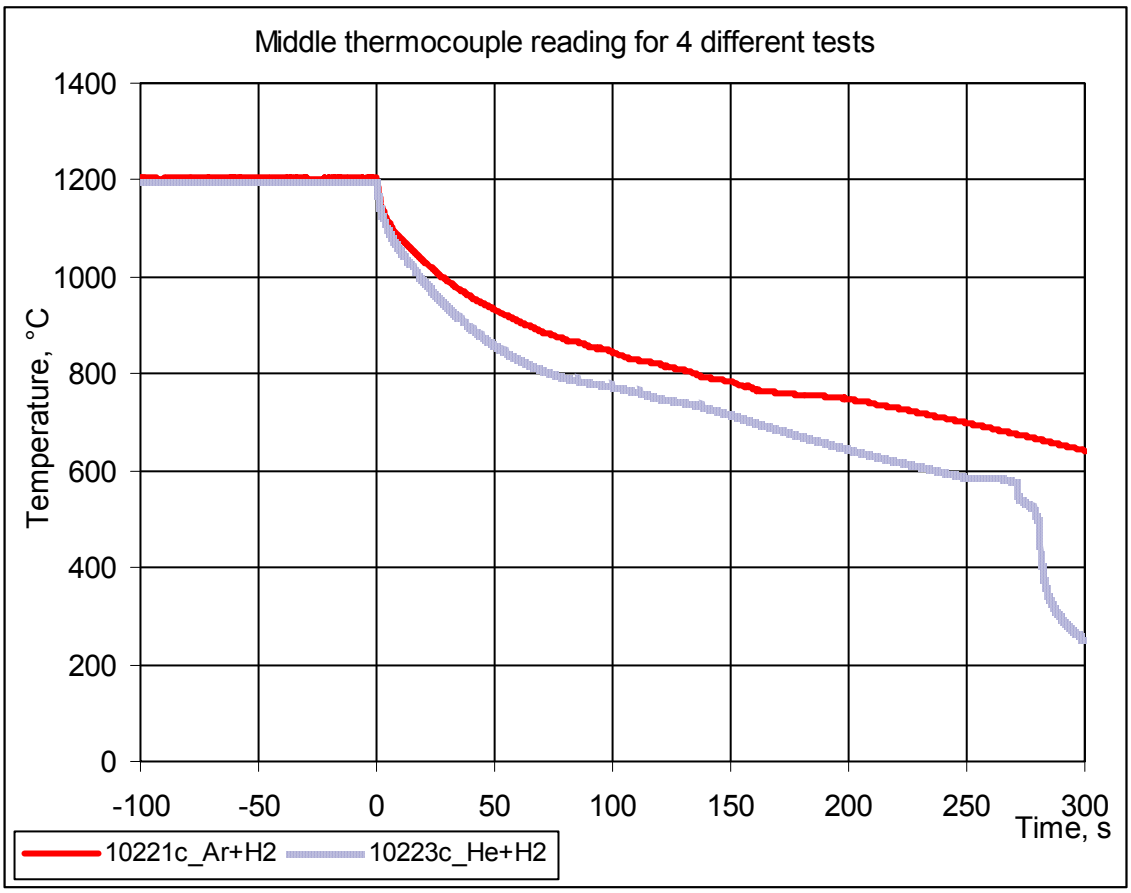

Fig. 7: Comparison of cool-down tests for two different gas mixtures.

Exothermic reaction between H_2 and Zr delays the cool-down and causes local warming-up

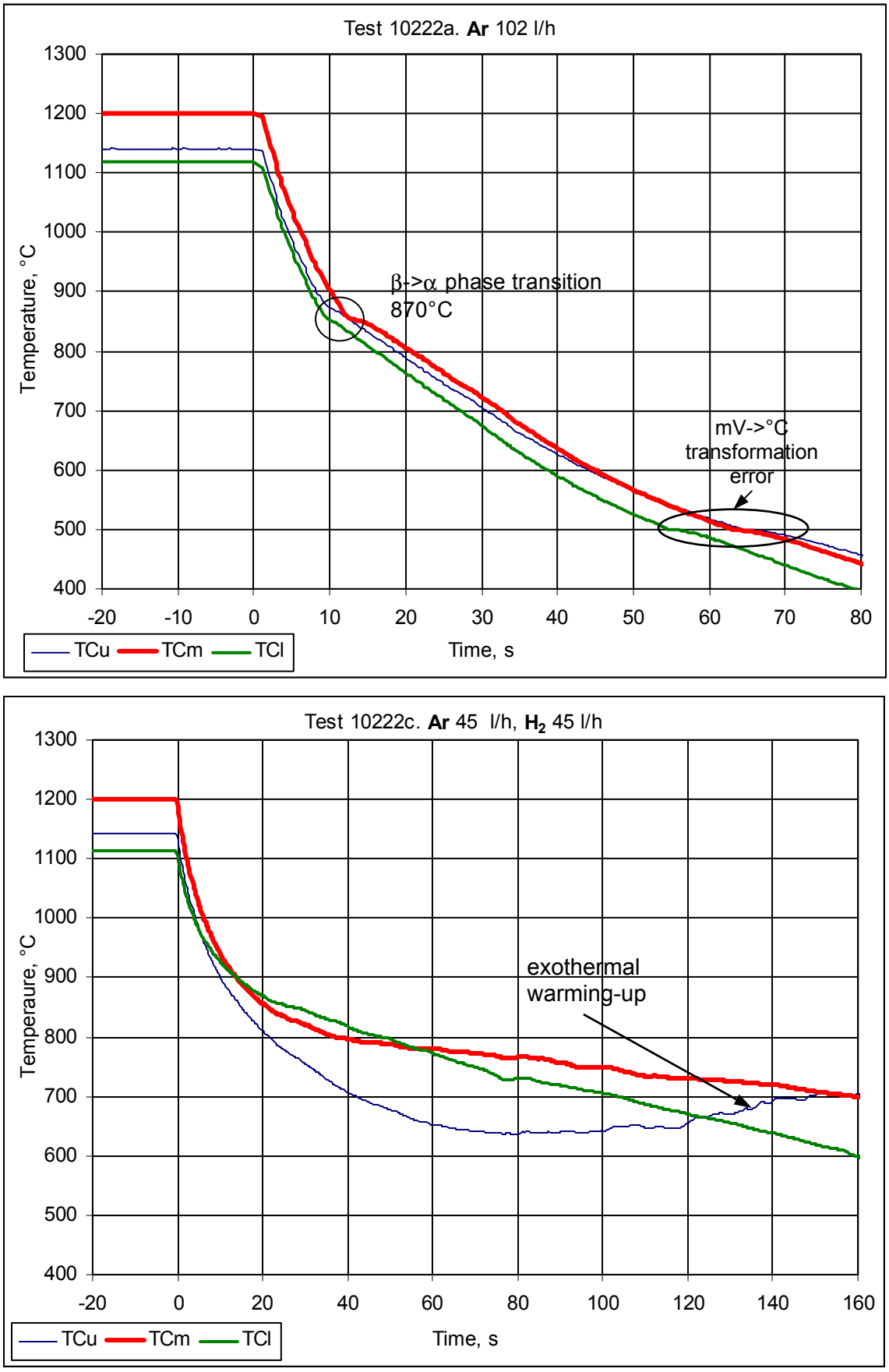

Fig. 8: Cool-down of an empty Zry-tube (test 10222) in Ar and Ar+H_2 gas mixture.

Exothermic reaction between H_2 and Zr delays the cool-down and causes the local warming-up

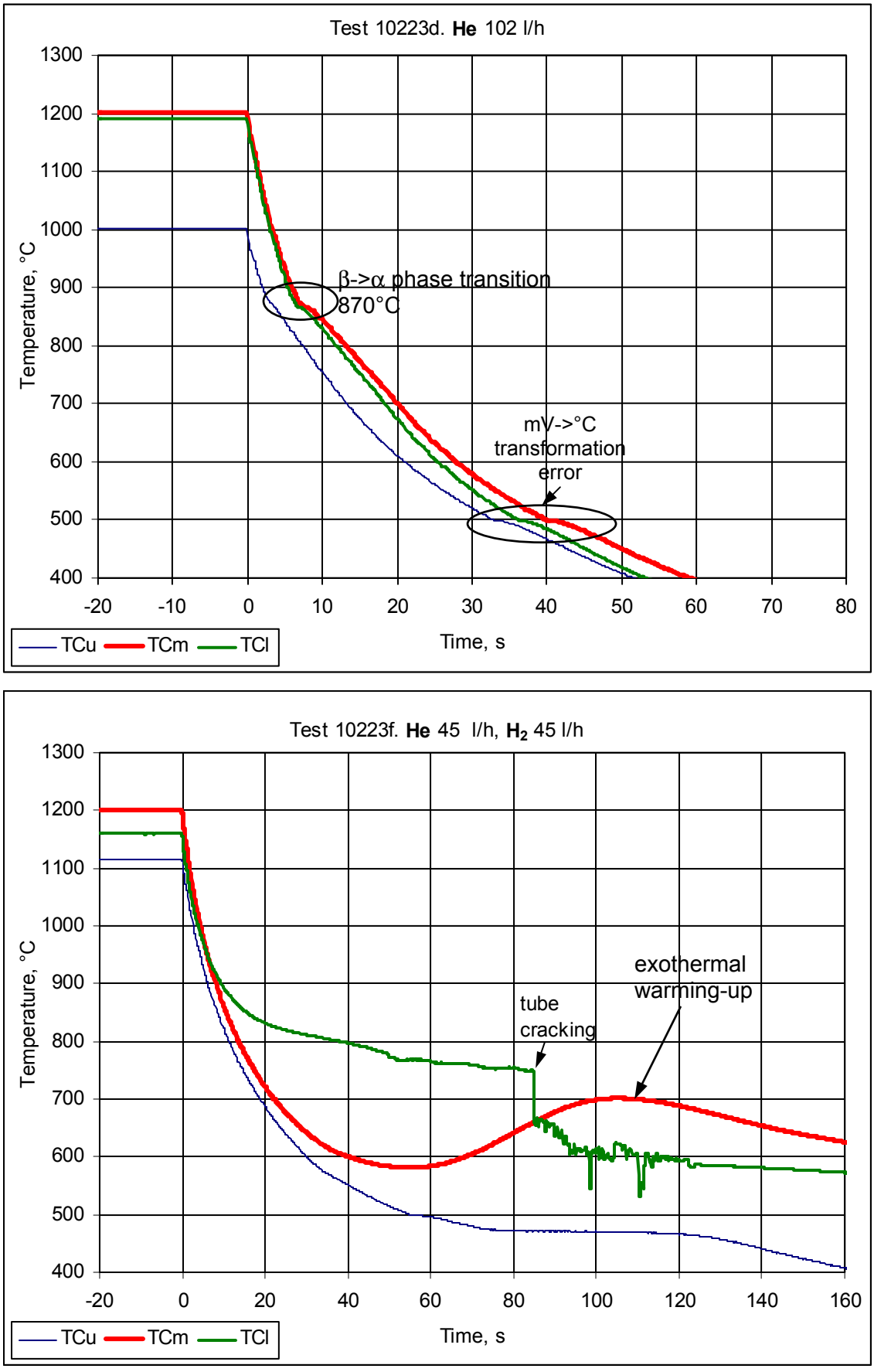

Fig. 9: Cool-down of an empty Zry-tube (tests 10223) in He and He+H_2 gas mixture.

Exothermic reaction between H_2 and Zr delays the cool-down and causes the local warming-up

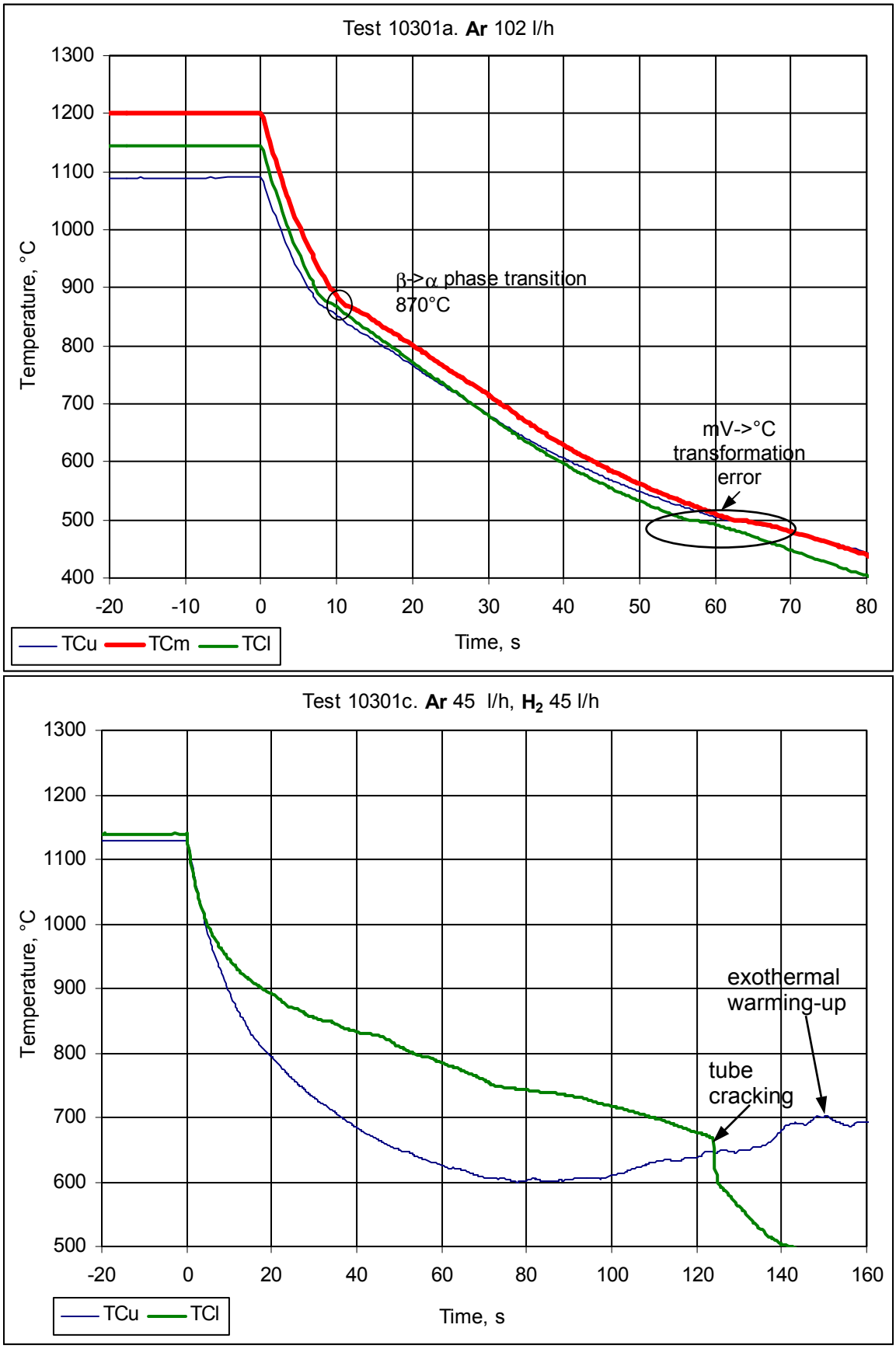

Fig. 10: Cool-down of an empty Zry-tube (tests 10301) in Ar and Ar+H_2 gas mixture.

Exothermic reaction between H_2 and Zr delays the cool-down and causes the local warming-up

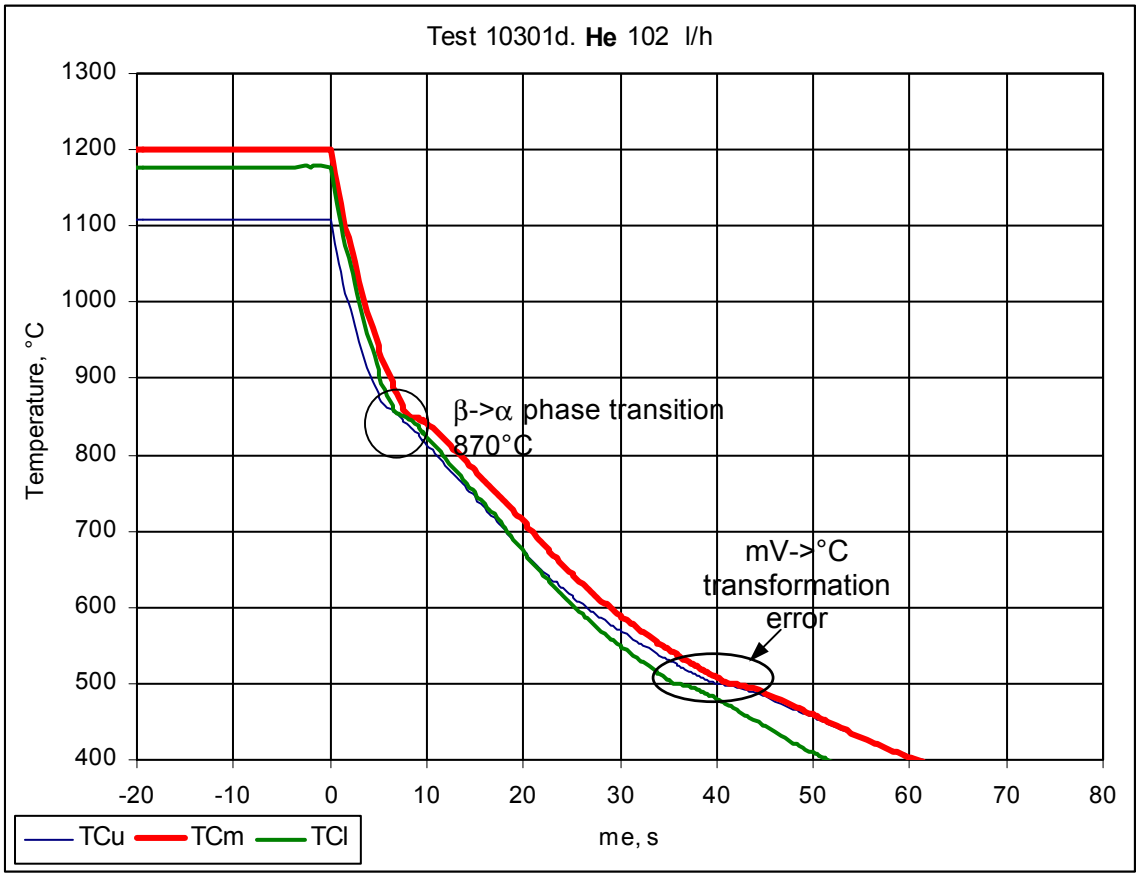

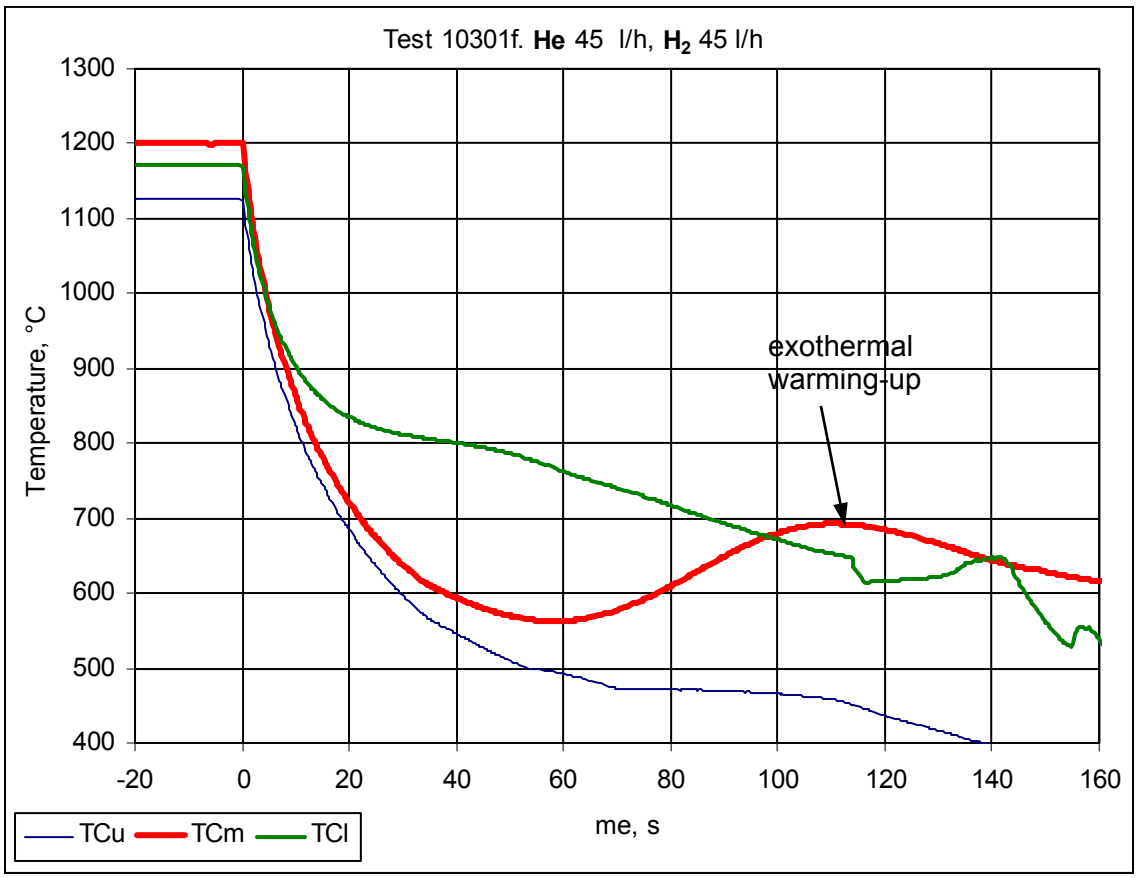

Fig. 11: Cool-down of an empty Zry-tube (tests 10301) in He and He+H_2 gas mixture.

Exothermic reaction between H_2 and Zr delays the cool-down and causes the local warming-up

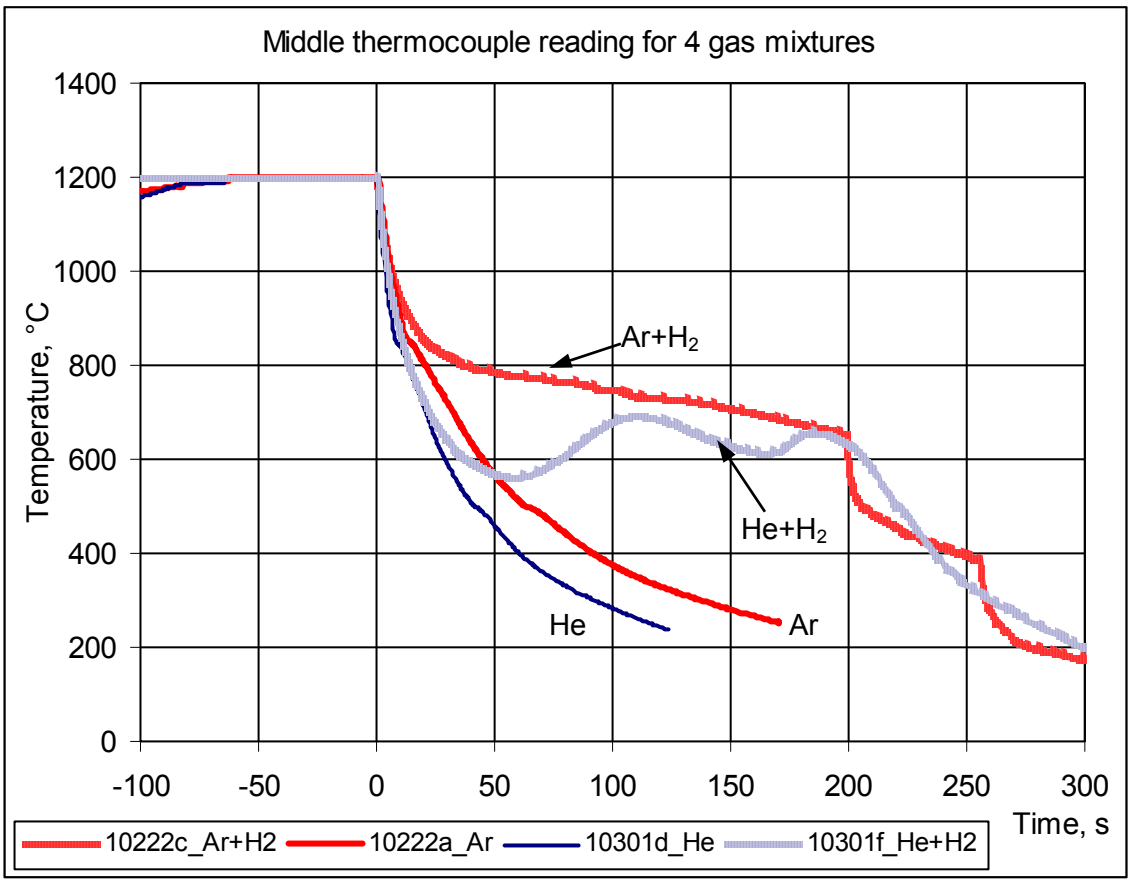

Fig. 12: Comparison of cool-down tests in 4 different gas mixtures.

Two effects:

1) The rod in He atmosphere cools faster because of higher thermal conductivity of He in comparison to Ar
2) Exothermic reaction between H_2 and Zr delays the cool-down and causes a local warming-up

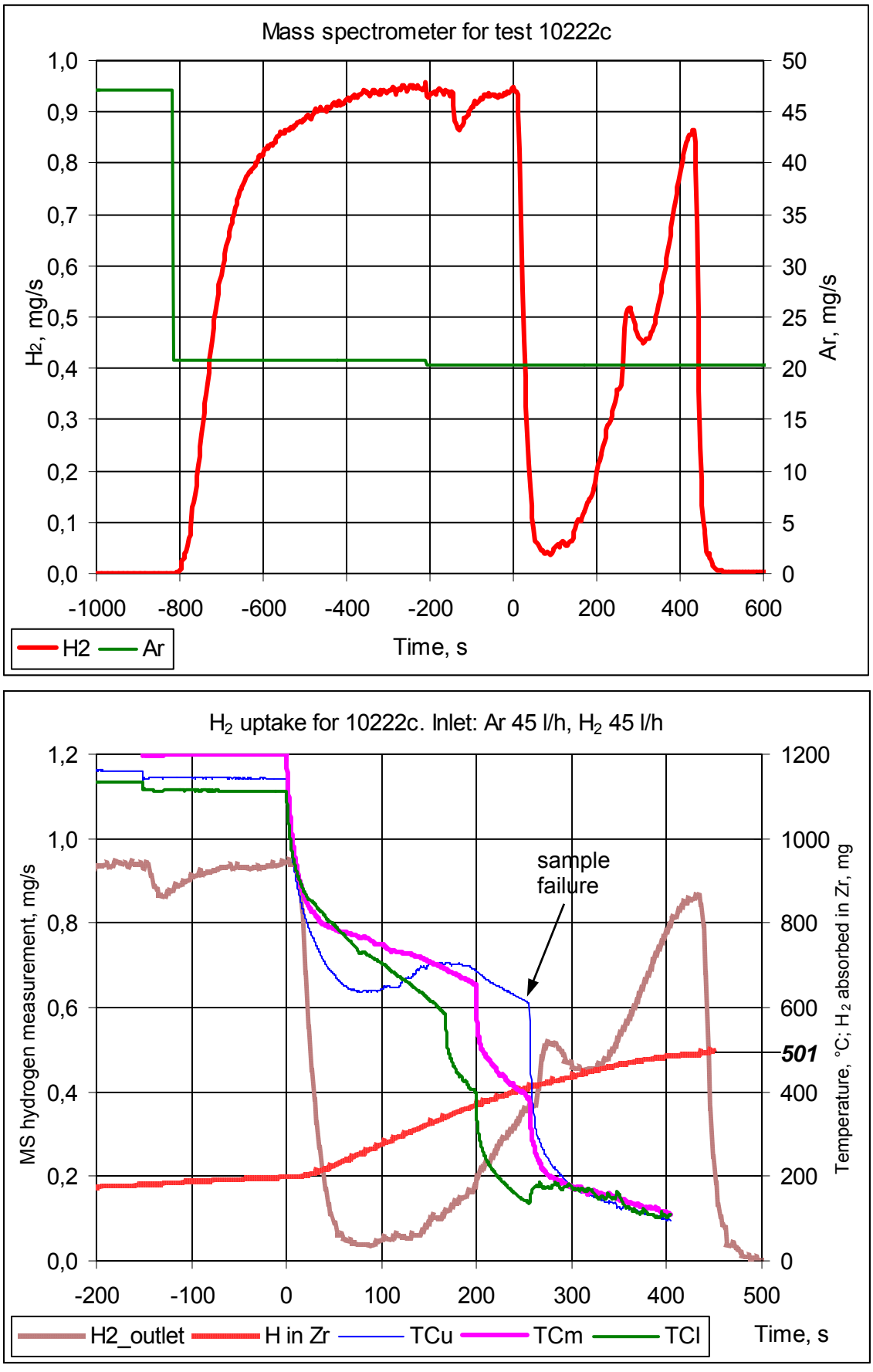

Fig. 13: Hydrogen measurement at the outlet of the gas channel and hydrogen uptake by Zr during the test 10222C (Ar+H_2).

The mass of absorbed hydrogen is calculated from total hydrogen input rate (45 l/h ~ 1 mg/s) and measured hydrogen outlet rate. The final value of 501 mg corresponds well with the sample weight gain during the test (460 mg)

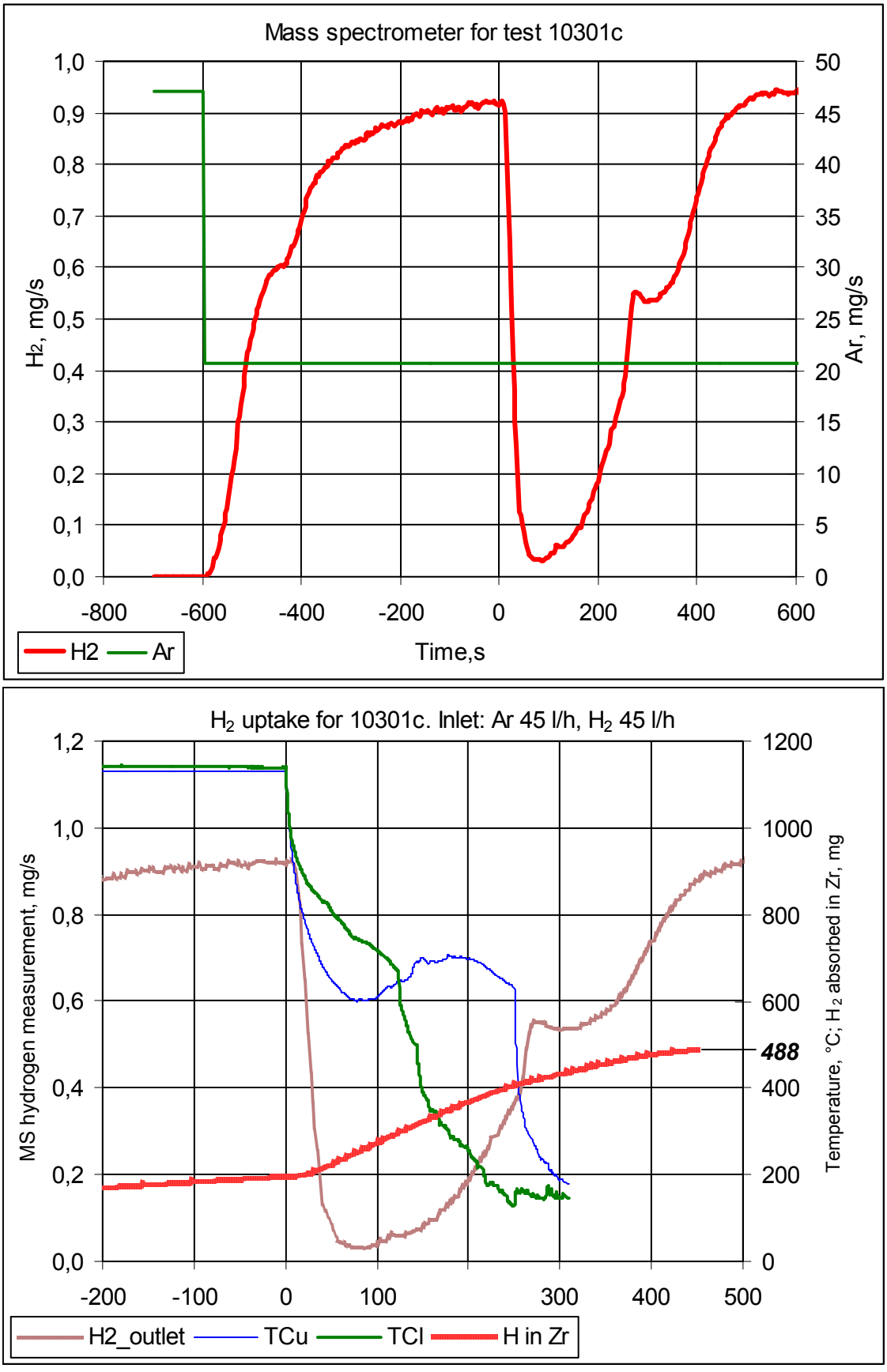

Fig. 14: Hydrogen measurement at the outlet of the gas channel and hydrogen uptake from Zr during the test 10301c (Ar+H_2)

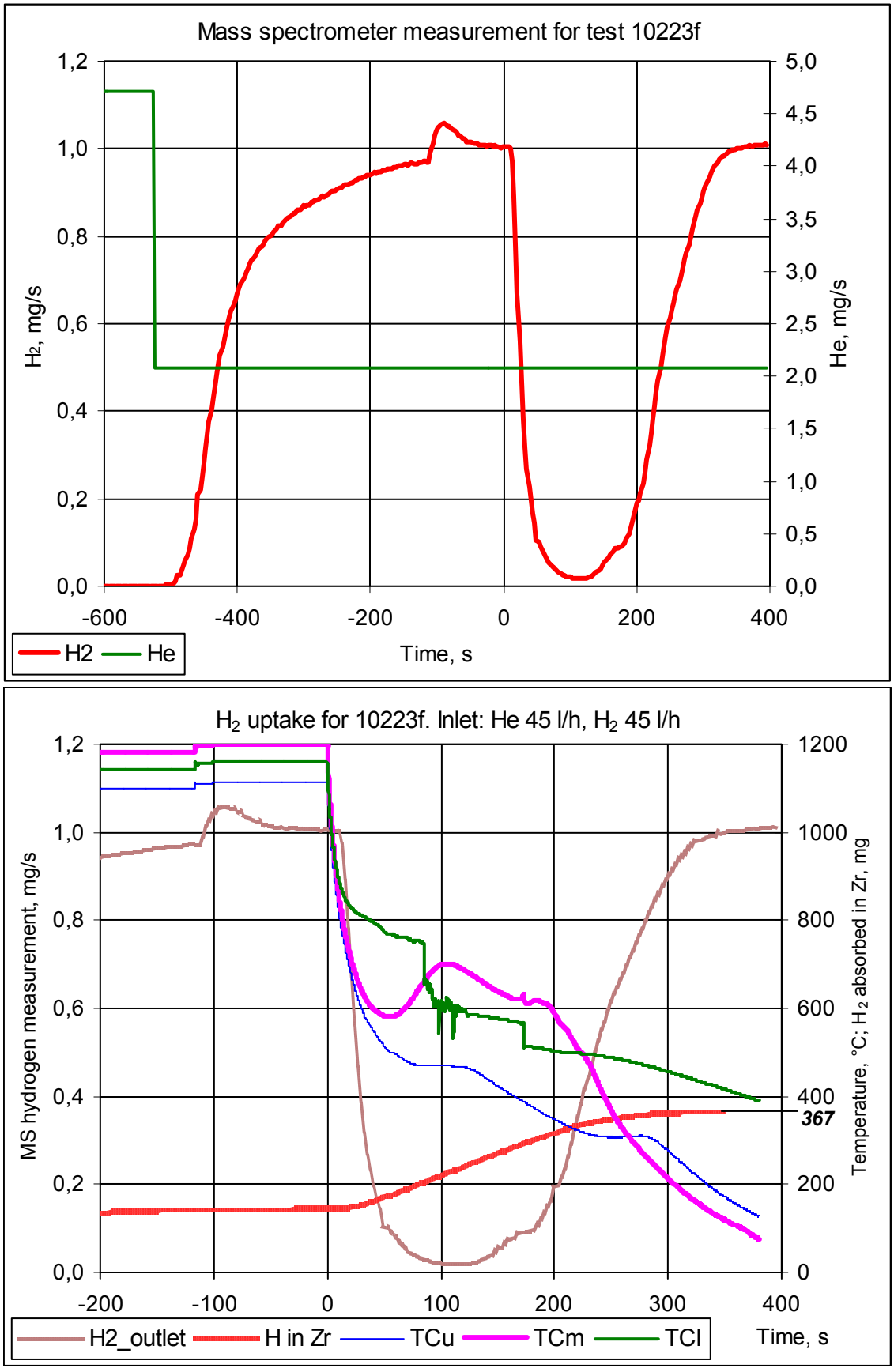

Fig. 15: Hydrogen measurement at the outlet of the gas channel and hydrogen uptake from Zr during the test 10223f ($He+H_2$)

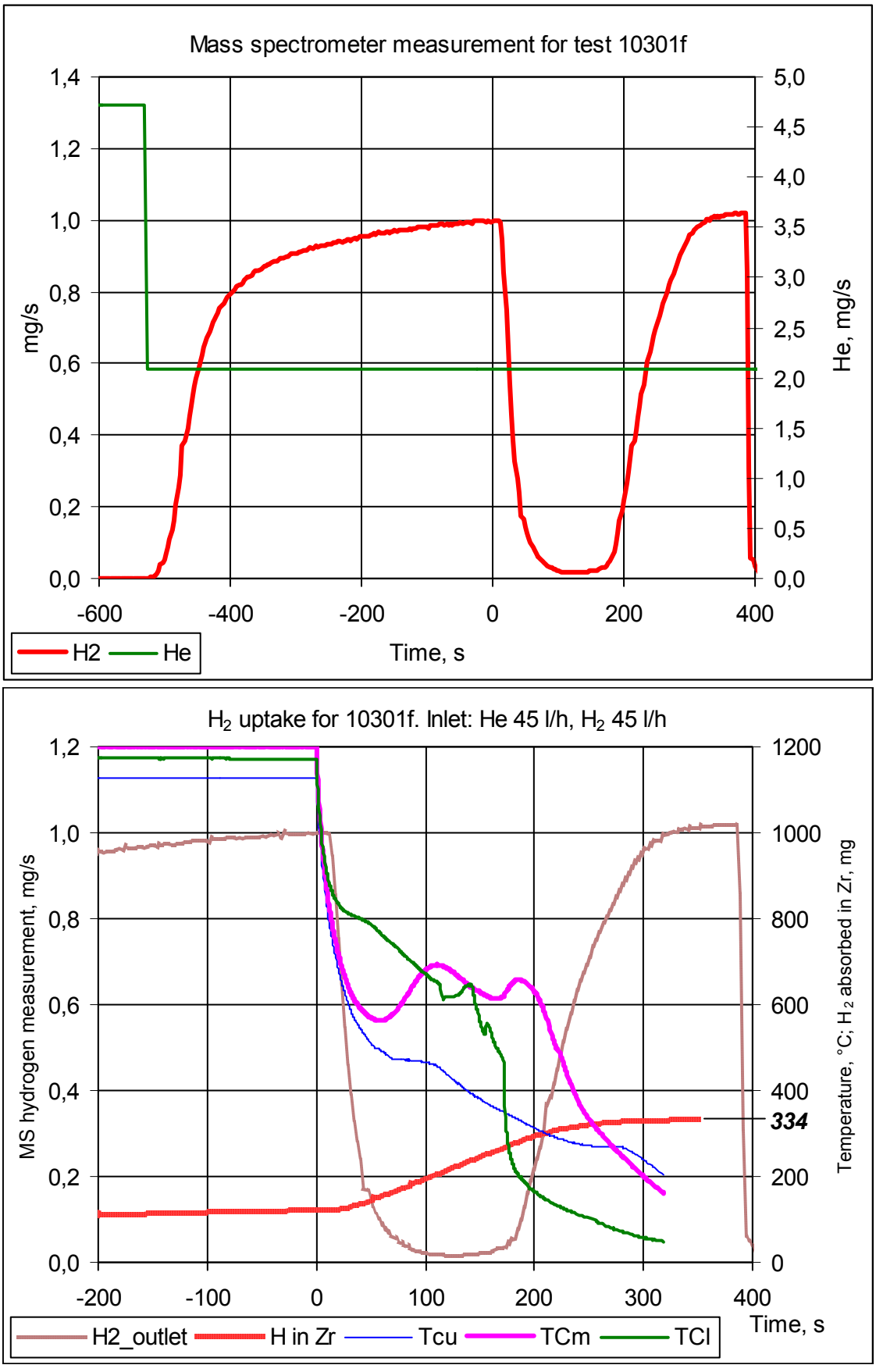

Fig. 16: Hydrogen measurement at the outlet of the gas channel and hydrogen uptake by Zr during the test 10301f ($He+H_2$).

There is less hydrogen absorbed than during the test 10223f because of the higher temperature TCl during the heating phase of the test 10301f

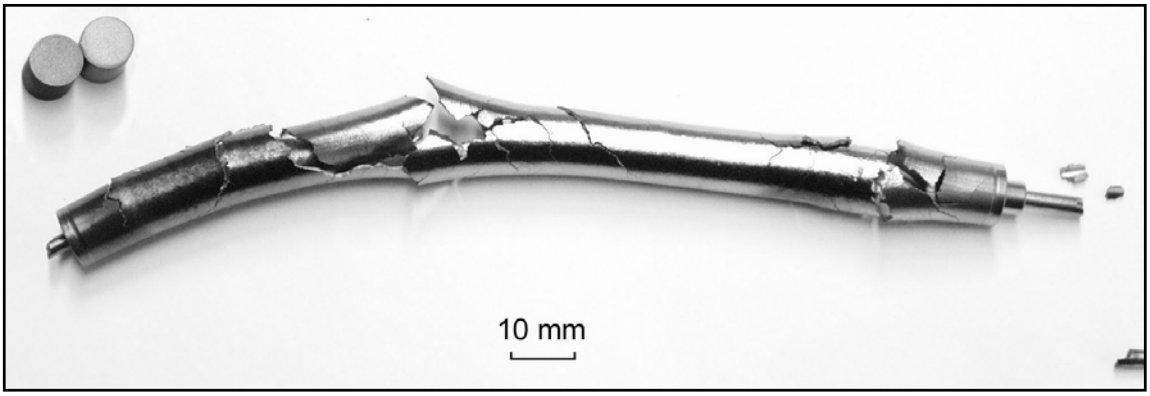

Test 10221c: Ar, H_2

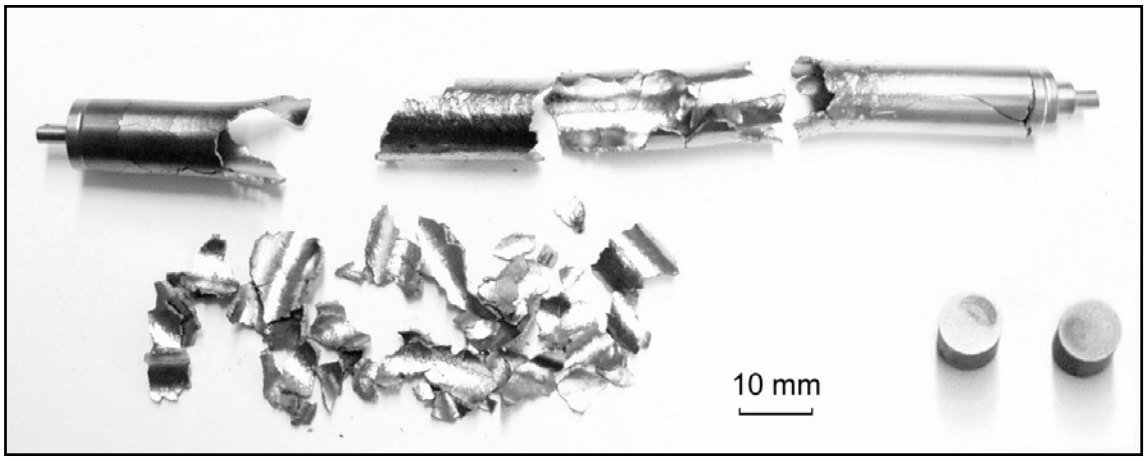

Test 10223c: He, H_2

Fig. 17: Rods <u>with pellets</u> after the tests at 1200°C in the mixture of inert gases and hydrogen

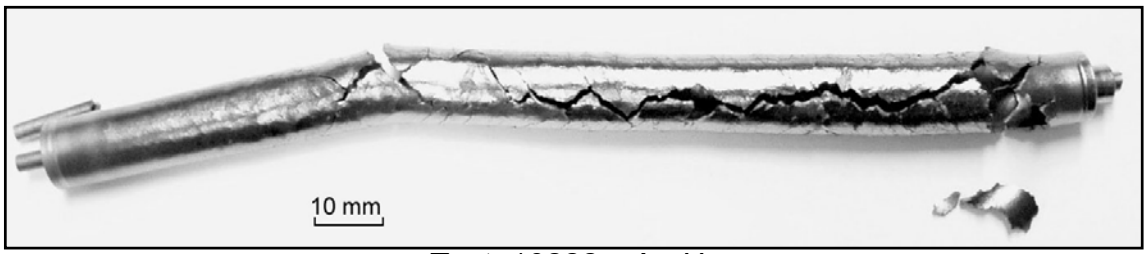

Test 10222c: Ar, H_2

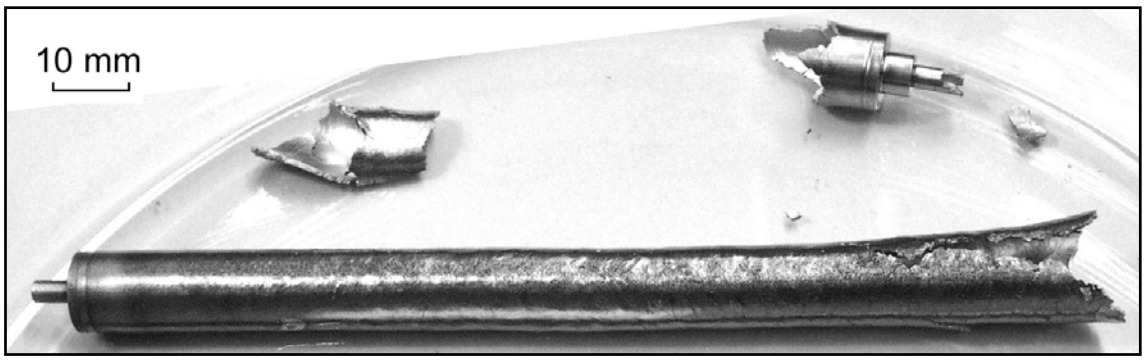

Test 10301c: Ar, H_2

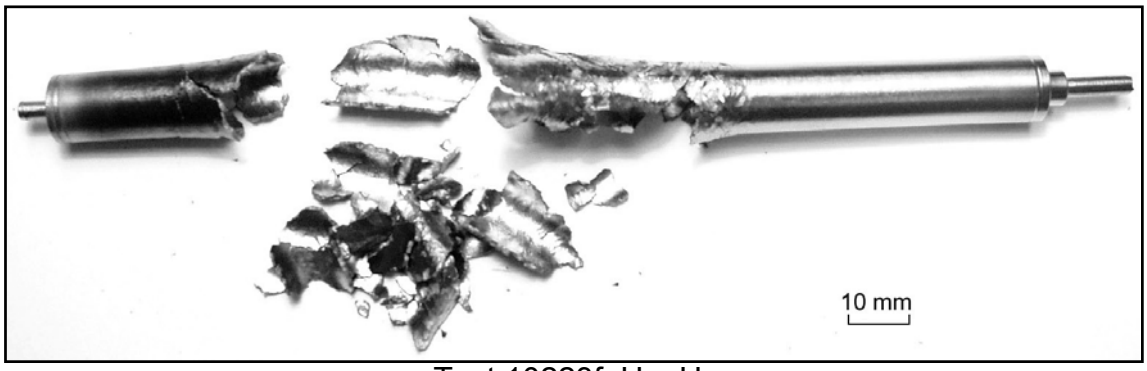

Test 10223f: He, H_2

Test 10301f: He, H_2

Fig. 18: Rods <u>without pellets</u> after the tests at 1200°C in the mixture of inert gases and hydrogen.

In Ar+H_2 the upper part of the rod became very brittle; whereas it was the lower part in He+H_2 atmosphere

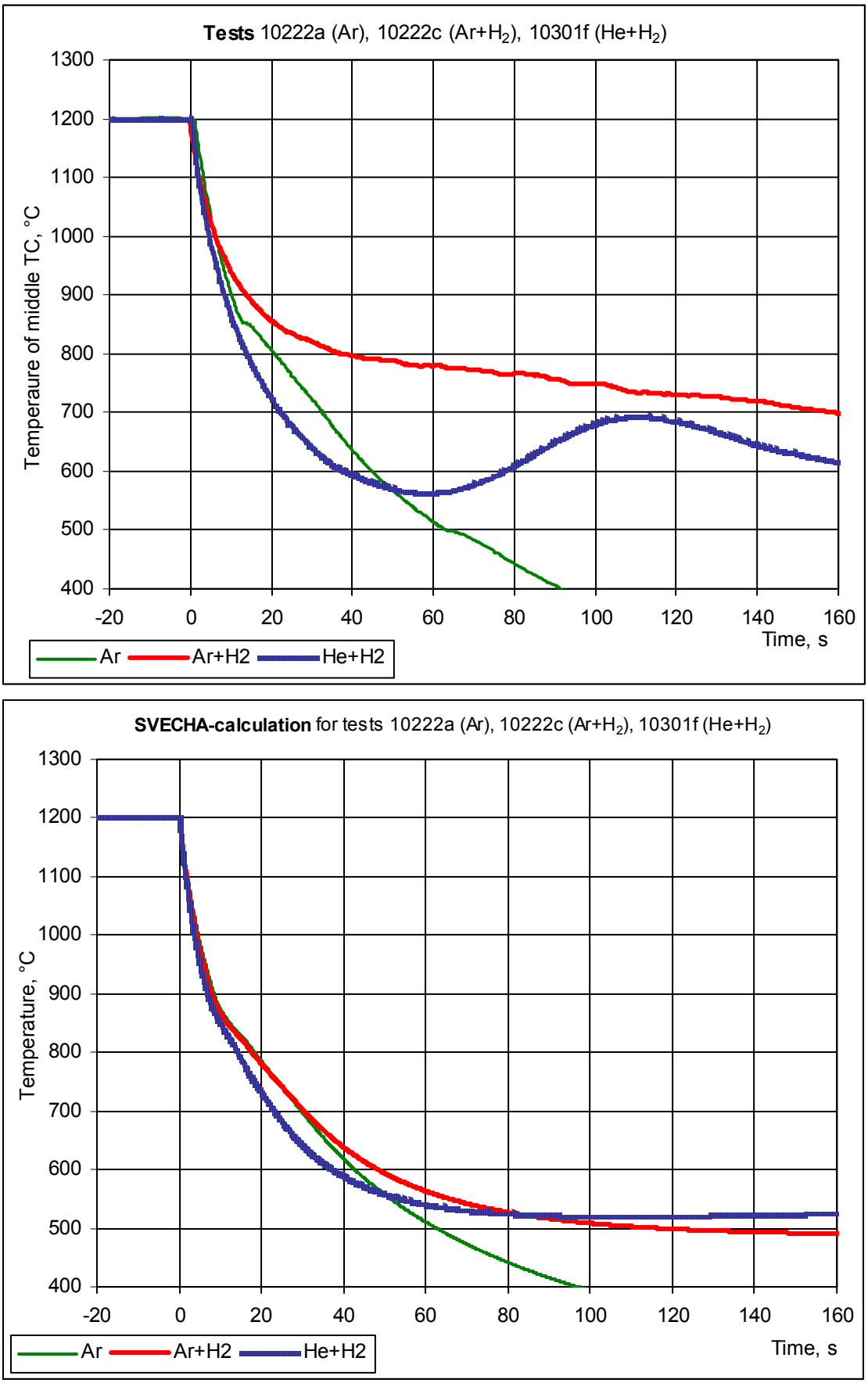

Fig. 19: Comparison of the test results with the corresponding SVECHA (version 2001) calculations.

Modelling should be corrected by including the exothermic effect of the hydrogen uptake

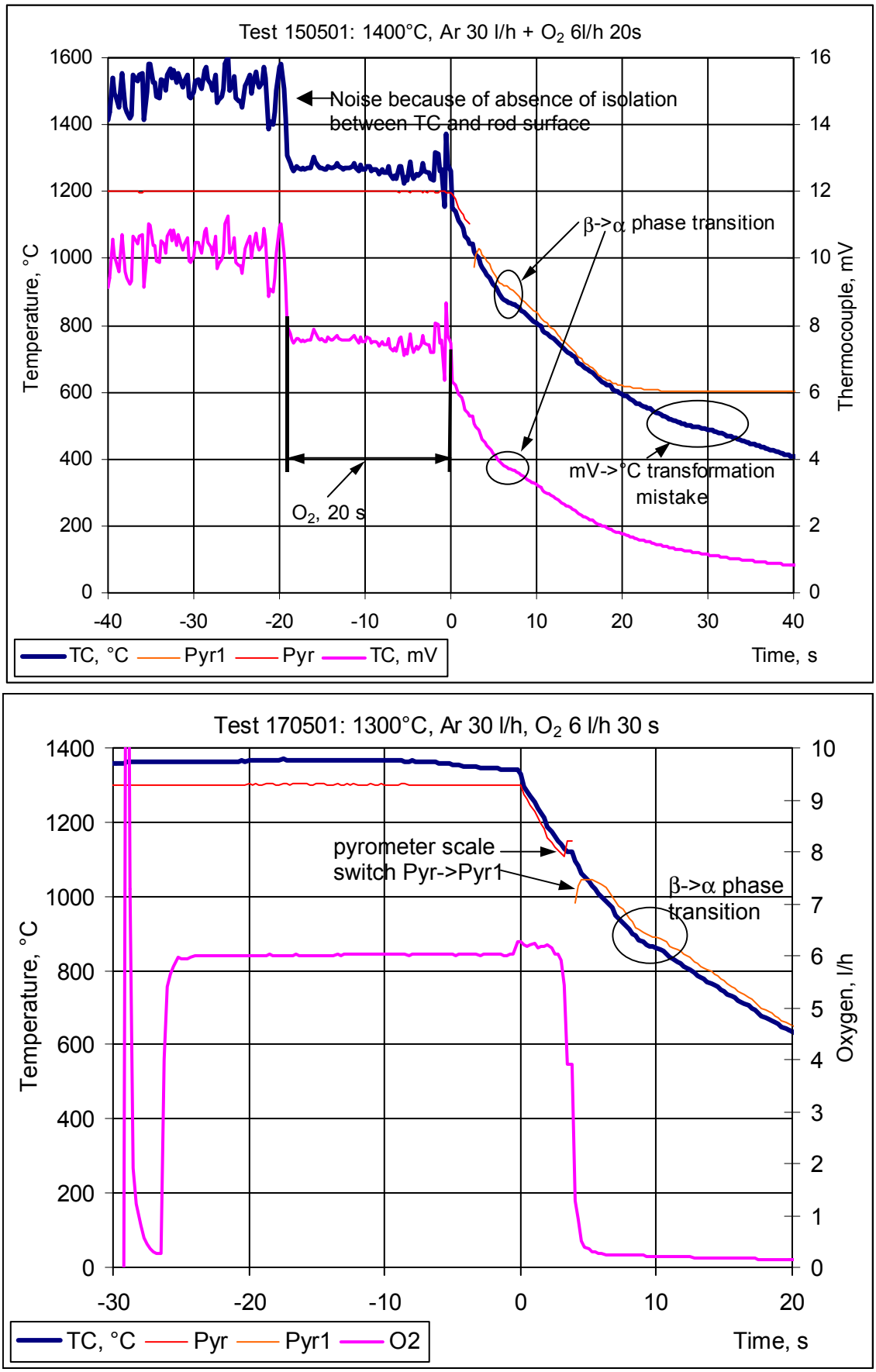

Fig. 20: Two tests on the cool-down of an empty oxidised Zry-tube in Ar atmosphere. (Final oxide layers thickness are 4 and 11 µm).

The lower values of surface temperature (<870°C), corresponding to the point of phase transition in Zry, shows the influence of oxide layer thermal resistivity

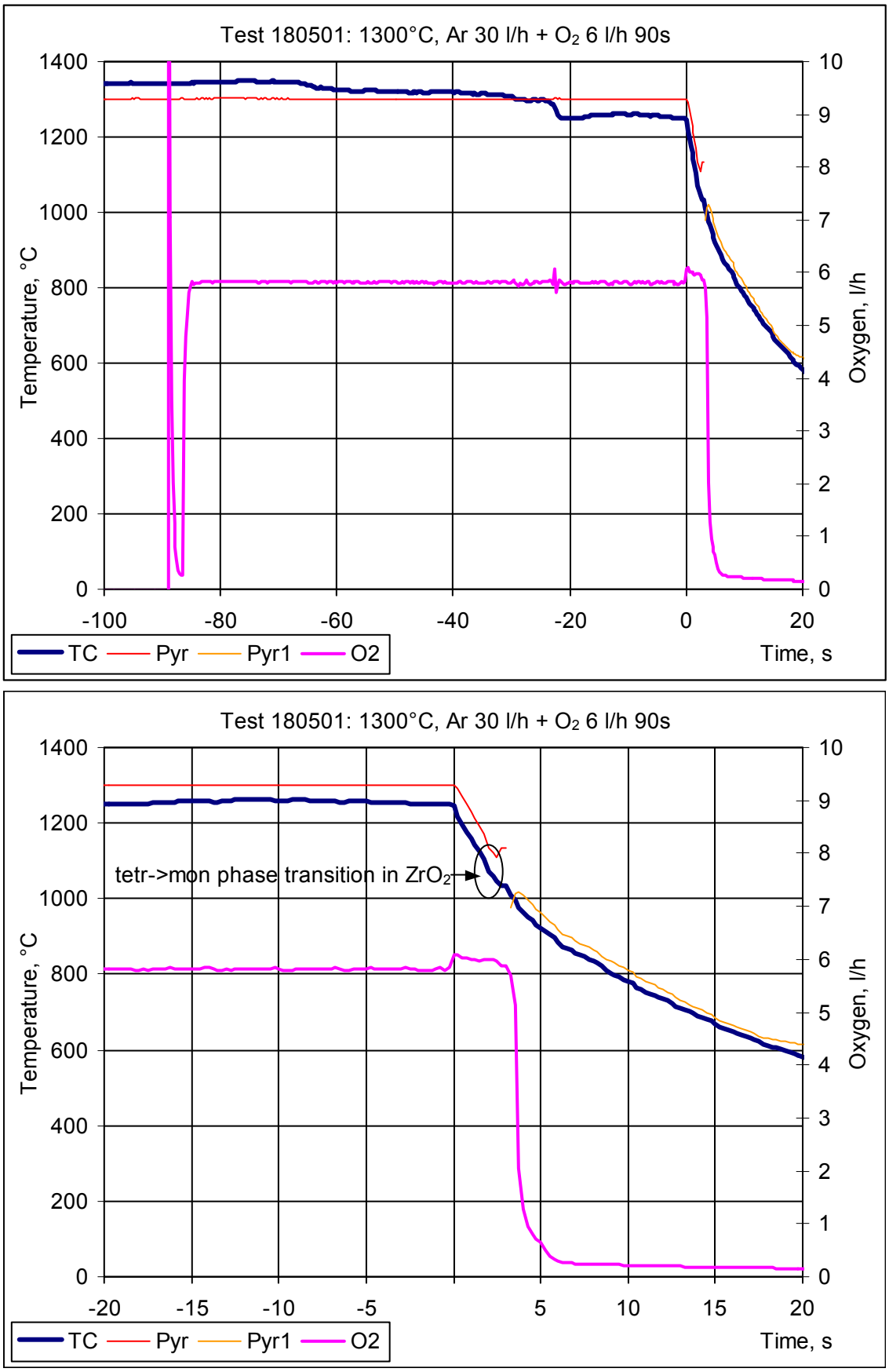

Fig. 21: Test on the cool-down of an empty oxidised Zry-tube in Ar atmosphere. (Final oxide layers thickness is 41 µm).

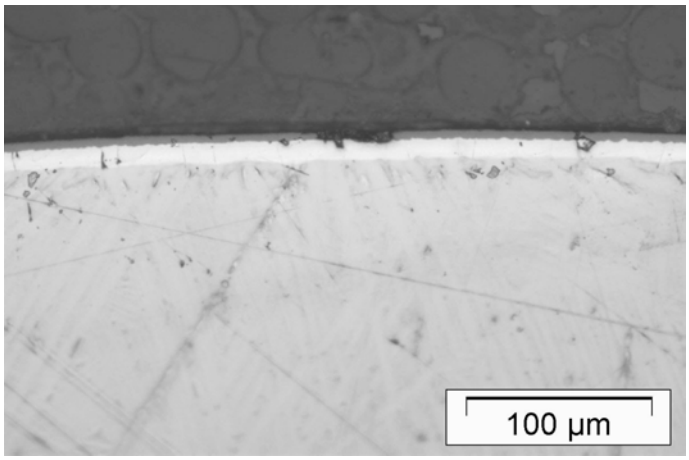

ZrO_2: 4 µm
α-Zr(O): 11 µm

β-Zr: residual

Test 150501: oxidation at 1260°C during 20s

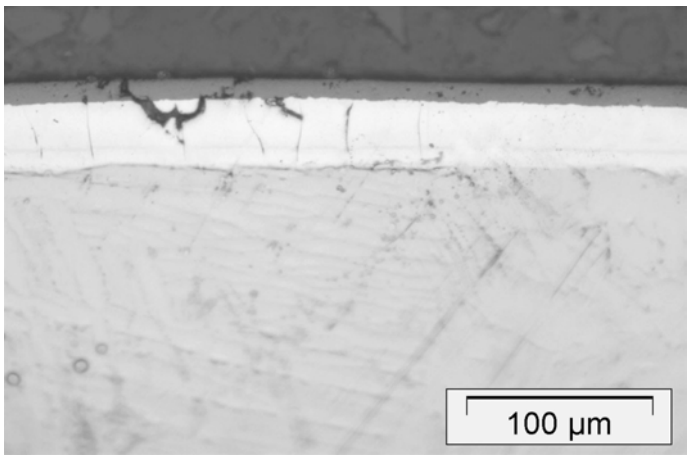

ZrO_2: 11 µm

α-Zr(O): 39 µm

β-Zr: residual

Test 1705011: oxidation at 1360°C during 30s

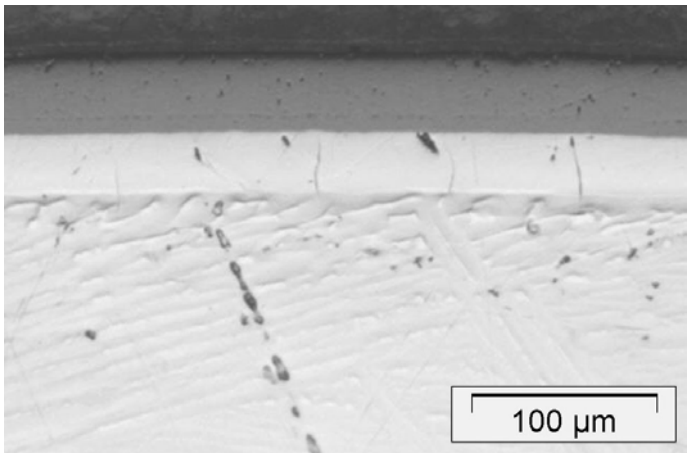

ZrO_2: 41 µm

α-Zr(O): 33 µm

β-Zr: residual

Test 1805011: oxidation at 1320°C during 90s

Fig. 22: Tests with Zry-cladding oxidation in Ar (30 l/h) + O_2 (6 l/h) gas mixture. The tests were performed with hermetically sealed and air-filled rods

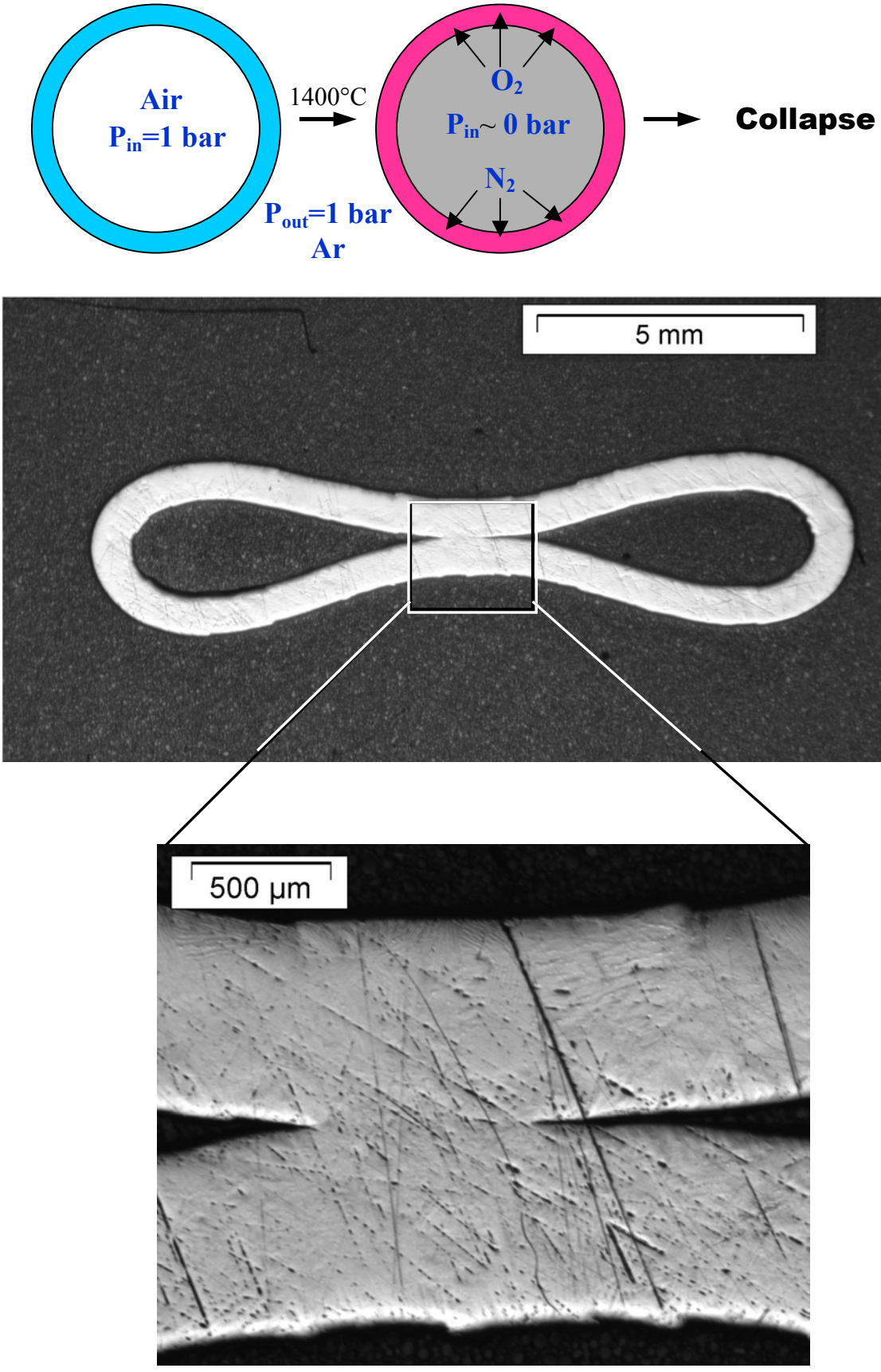

Fig. 23: Test 1705012. Collapse of the air filled and sealed Zry-cladding rod at 1400°C.

During the heating the oxygen and nitrogen were dissolved by the metal. The outer atmosphere pressure caused the collapse

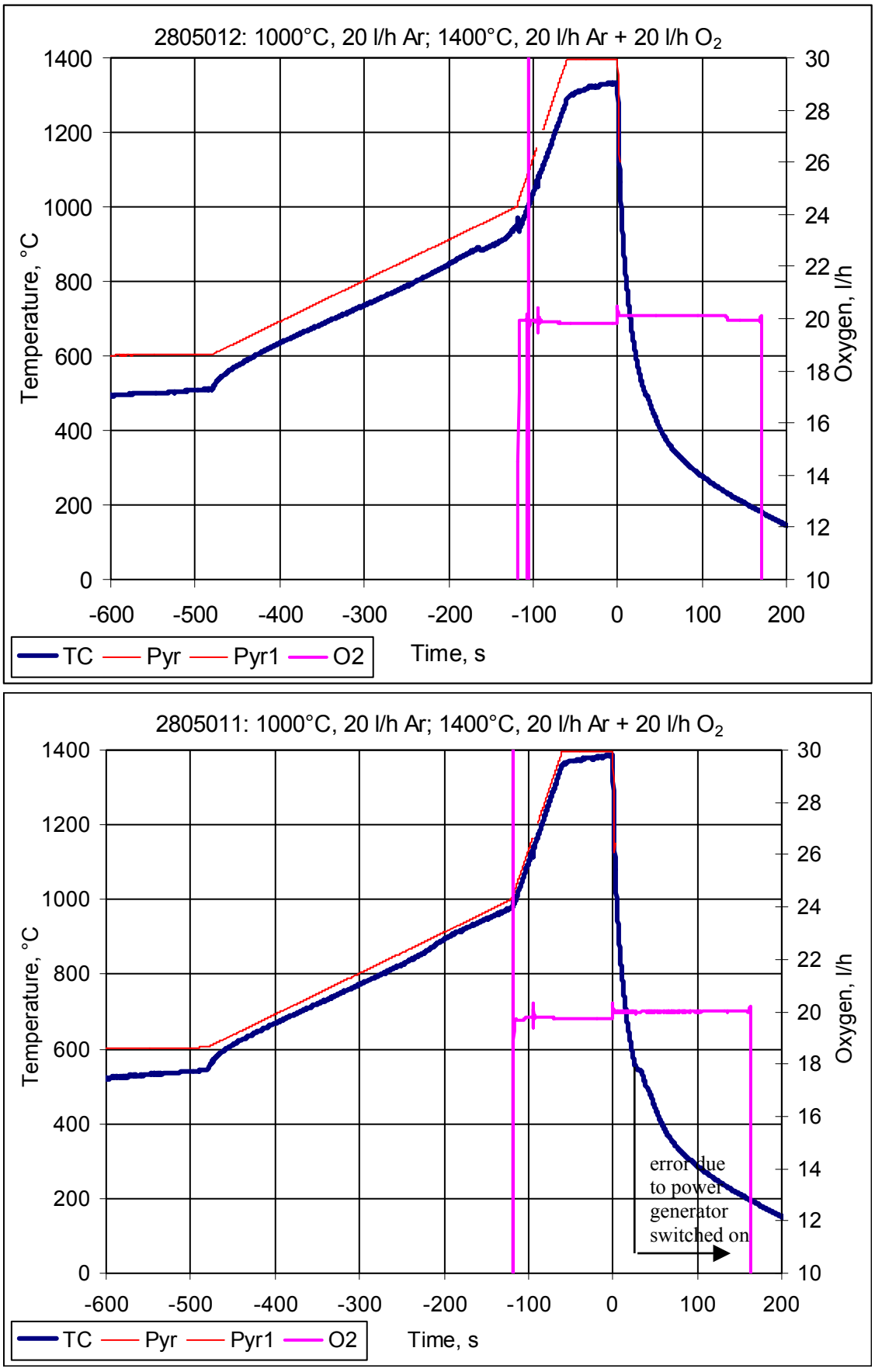

Fig. 24: Two tests on cool-down of empty Zry-tube in Ar and O_2 gas mixture. (Final oxide layer thickness is 65 µm).

Oxygen supply during transient, constant temperature and cool-down phases

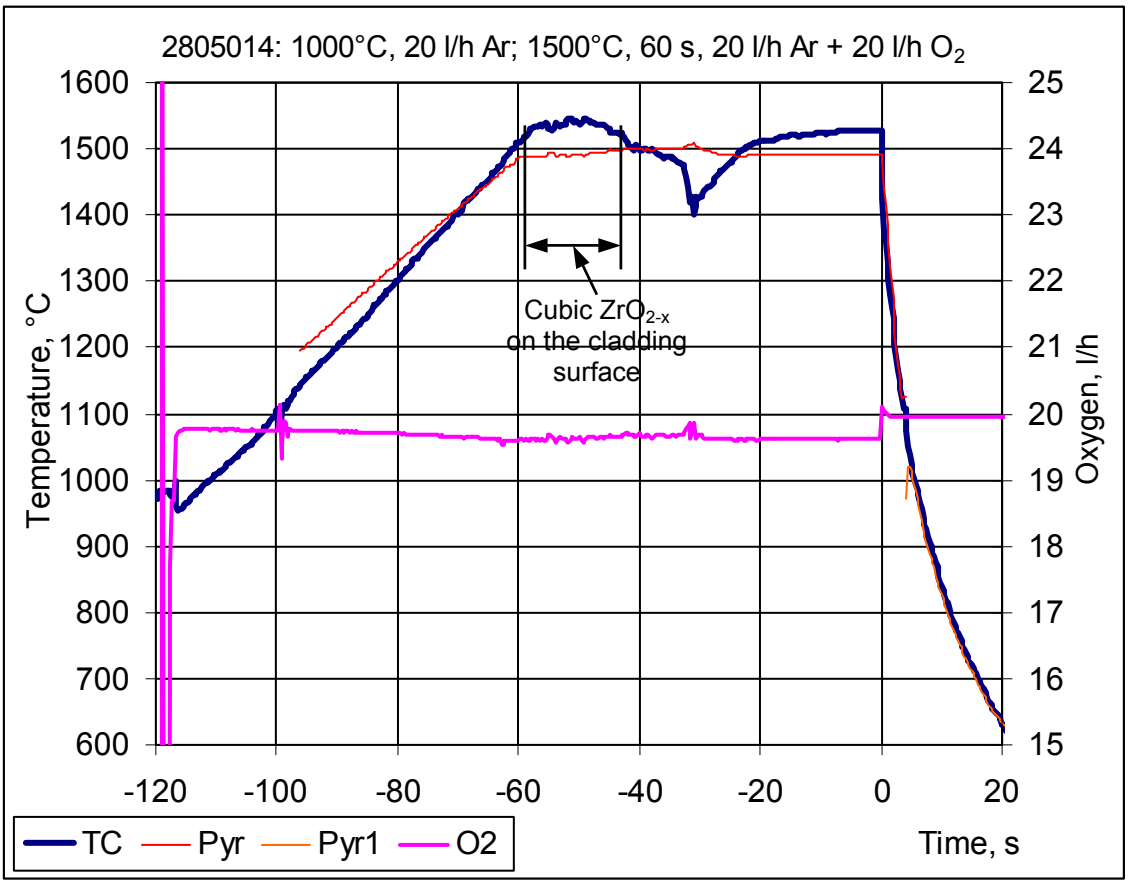

Fig. 25: High temperature test on cool-down of an empty Zry-tube in Ar and O_2 gas mixture. (Final oxide layer thickness is 100 µm).

Oxygen supply during transient, constant temperature and cool-down phases.

Formation of the cubic ZrO_{2-x} phase on the rod surface at temperature above 1525°C changes the optical properties of oxide layer and influences the pyrometer measurement

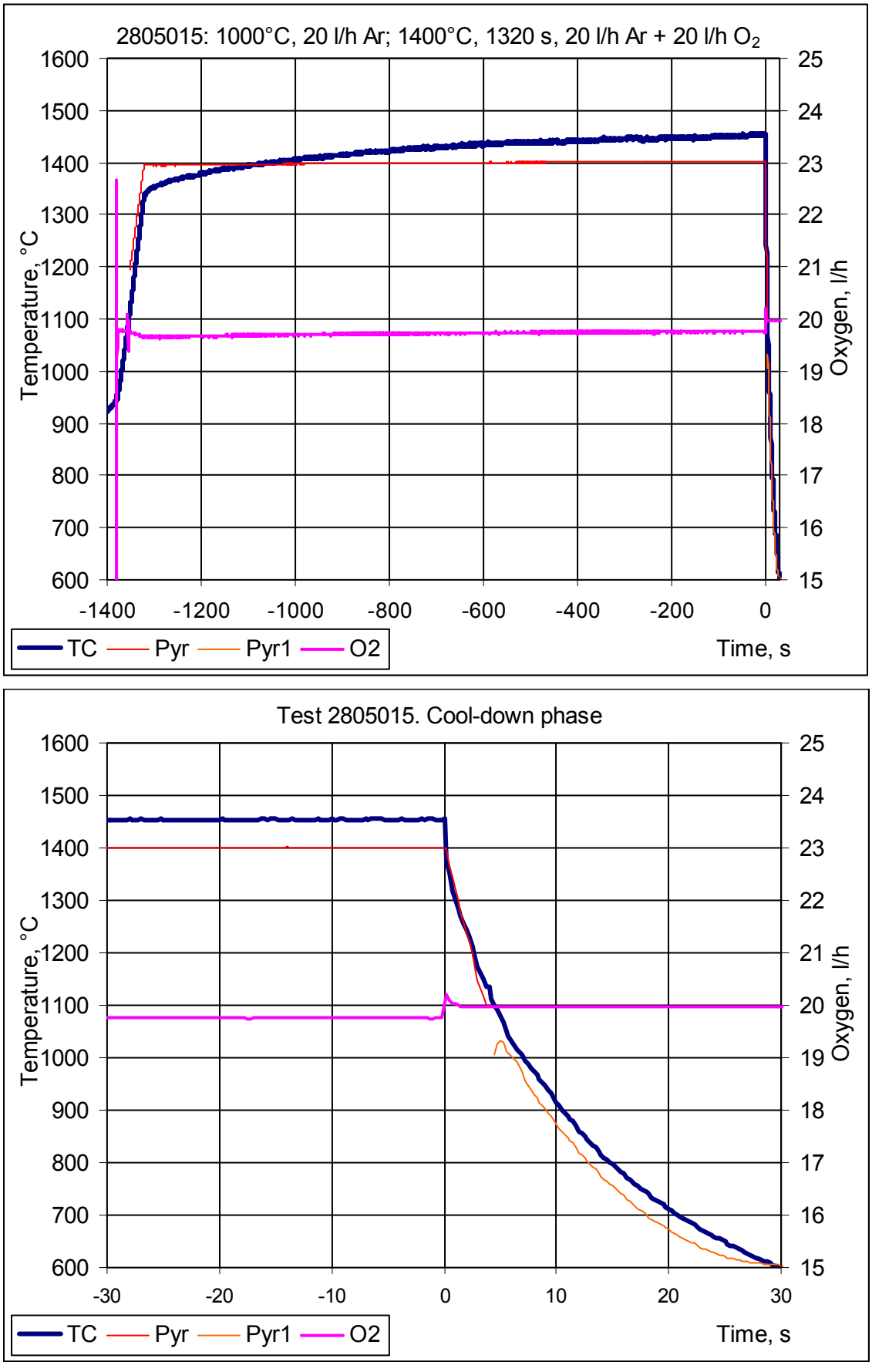

Fig. 26: Test on cool-down of an empty Zry-tube in Ar and O_2 gas mixture. (Final oxide layer thickness is 300 µm).

Oxygen supply during transient, constant temperature and cool-down phases

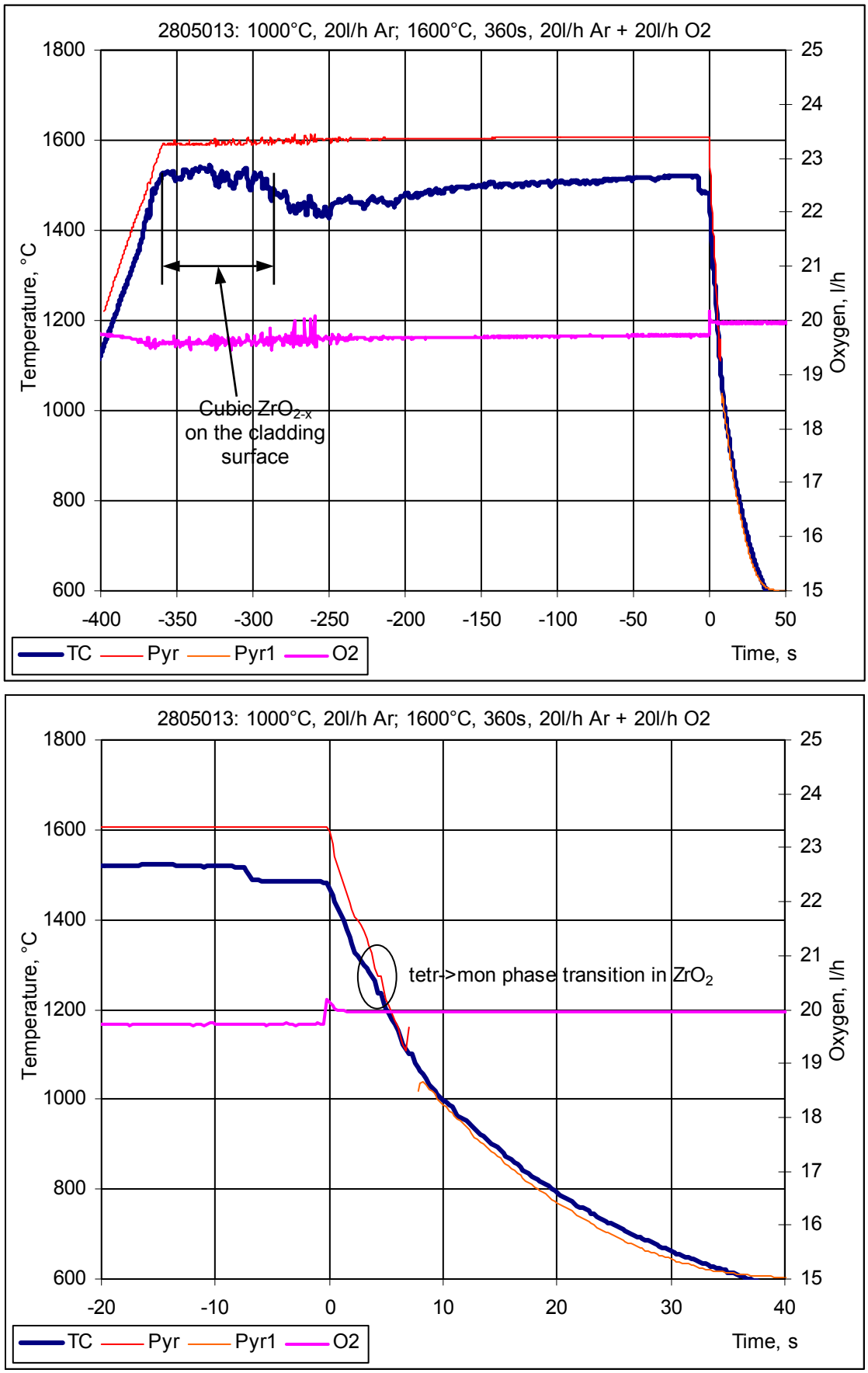

Fig. 27: Test on cool-down of an empty Zry-tube in Ar and O_2 gas mixture. (Final oxide layer thickness is 570 µm).

Oxygen supply during transient, constant temperature and cool-down phases

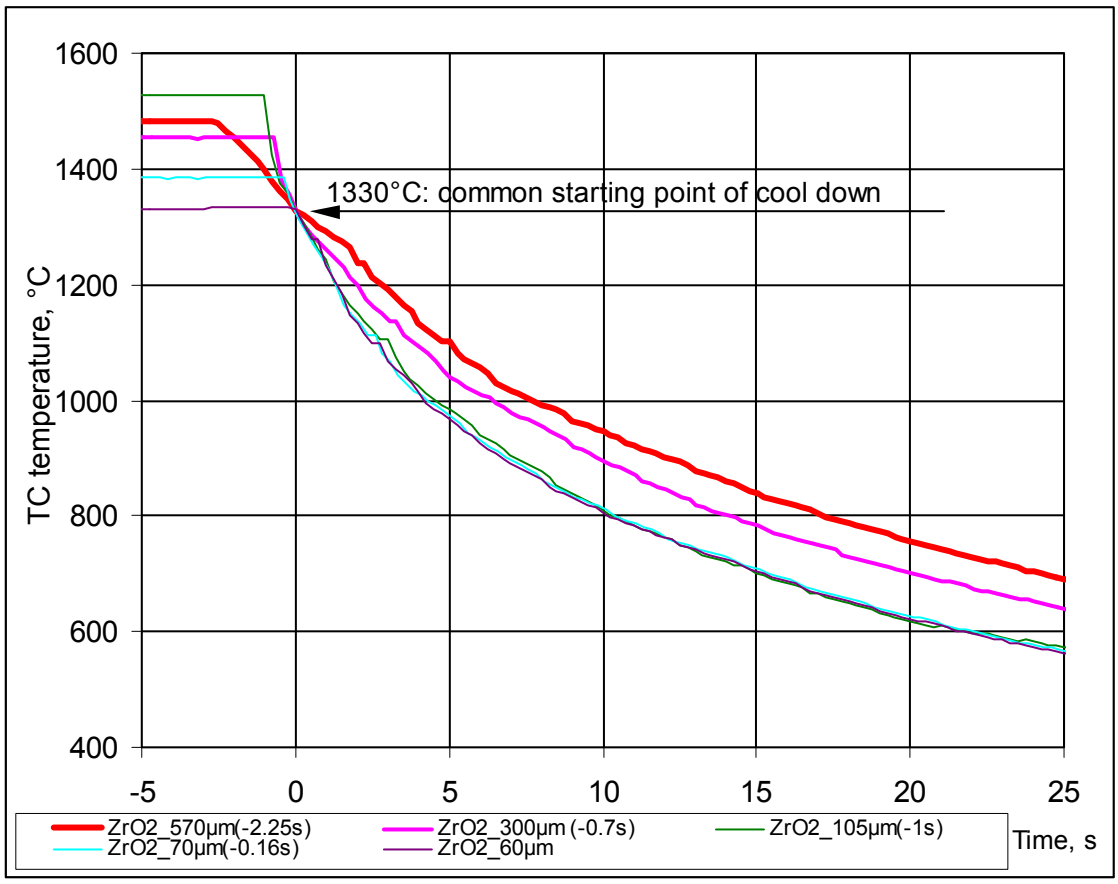

Fig. 28: Comparison of the cool-down of oxidised Zry tubes in an Ar (20 l/h) and O_2 (20 l/h) gas mixture.

The curves for the tests 2805013, 2805015, 2805014, 2805011, 2805012 are shown. Time offsets correspond to test 2805012.

The tubes with the oxide layer thickness of more 100 µm cool slower than the tubes with the thinner oxide layer.

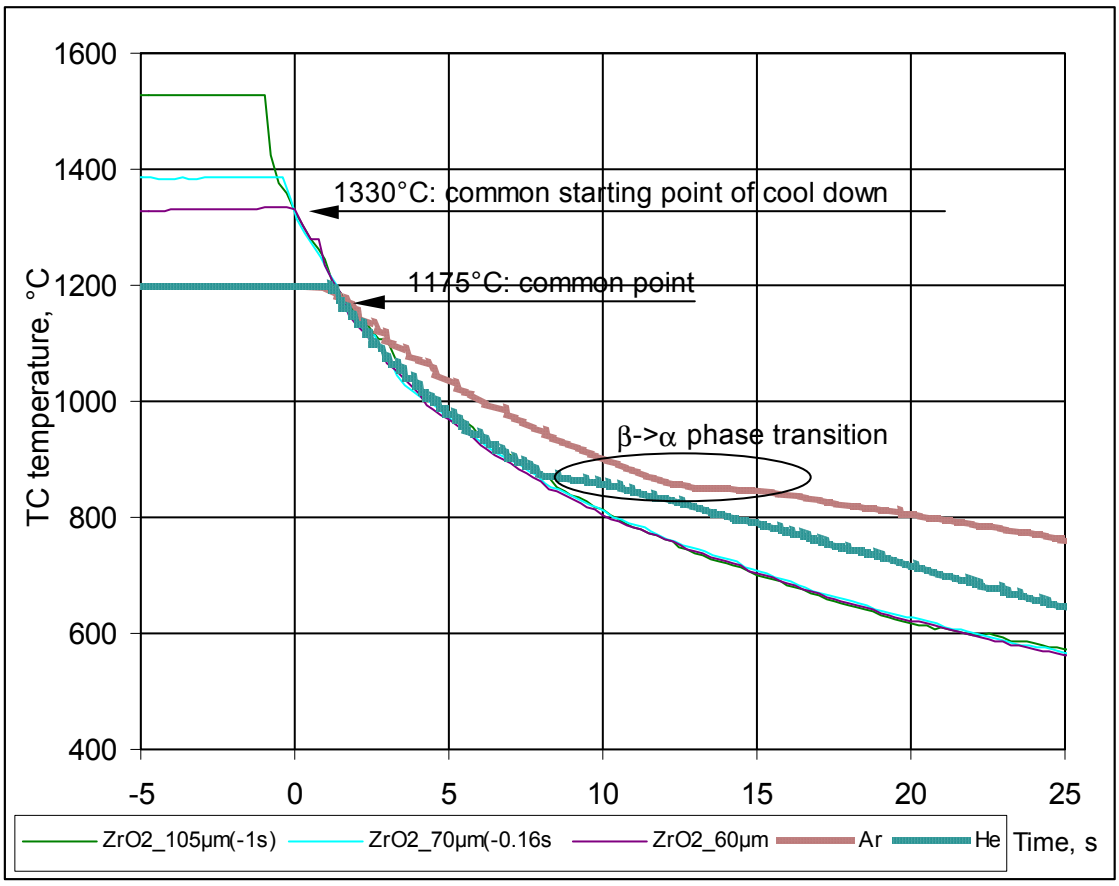

Fig. 29: Comparison of the cool-down of oxidised tubes in the Ar and O_2 gas mixture with the cool-down of unoxidised tubes in inert gases.

The curves for tests 2805014, 2805011, 2805012, 10223D, 10222A are shown.

The oxidised samples show no exothermic effect of phase transition in metal.

Competition of two phenomena:

1) **The sample cools slower in Ar-atmosphere, than in another atmospheres because of the low thermal conductivity of Ar (λ=49.2 mW/(m*K) at 1000°C) in comparison to He (λ=429.9 mW/(m*K) at 1000°C) and O_2 (λ=88.9 mW/(m*K) at 1000°C);**
2) **The emissivity of ZrO_2 is higher (ε~0.6) than the emissiviy of Zry (ε~0.3)**

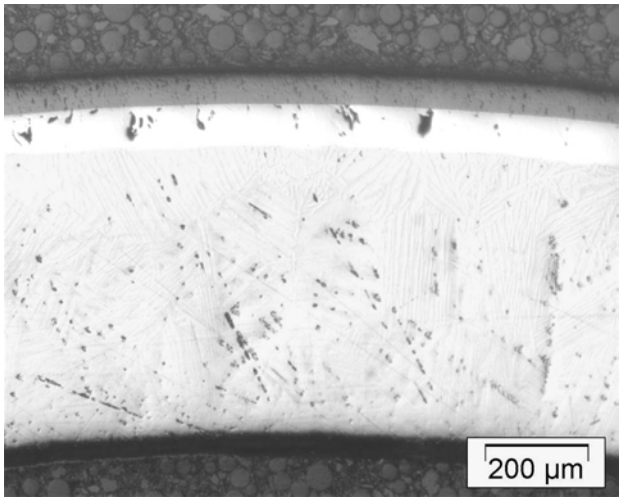

ZrO_2: 58 µm

α-Zr(O): 85 µm

β-Zr: 565 µm

Test 280501_2: oxidation 1320°C during 60 s

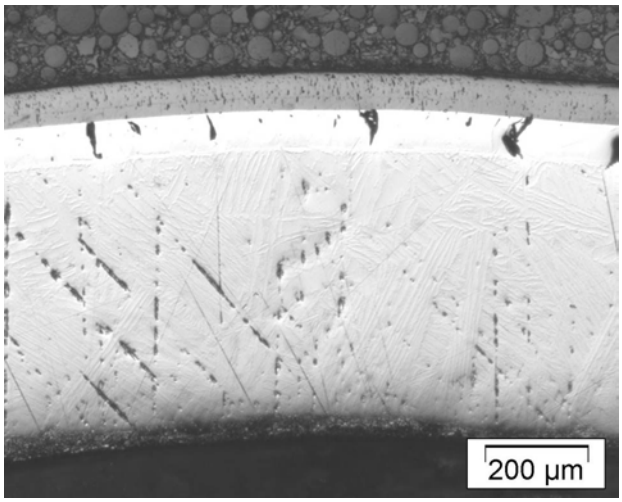

ZrO_2: 71 µm

α-Zr(O): 83 µm

β-Zr: 549 µm

Test 280501_1: oxidation at 1380°C during 60 s

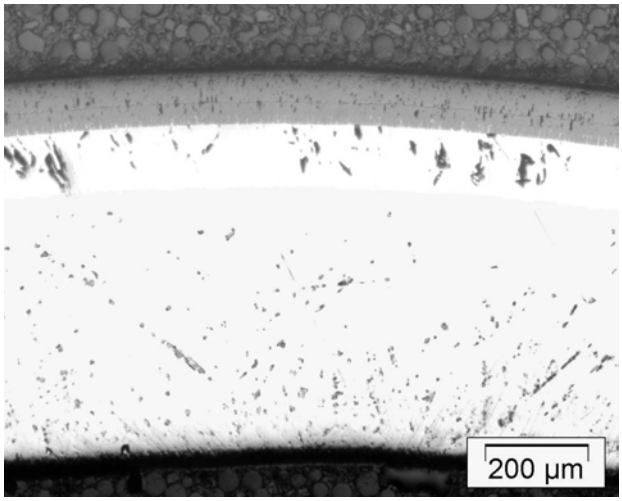

ZrO_2: 106 µm
(15 µm cubic ZrO_{2-x})

α-Zr(O): 103 µm

β-Zr: 538 µm

Test 280501_4: oxidation at 1520°C during 60 s

Fig. 30: Tests with oxidation of Zry-tubes in Ar (20 l/h) and O_2 (20 l/h) gas mixture during 60 s at different temperatures

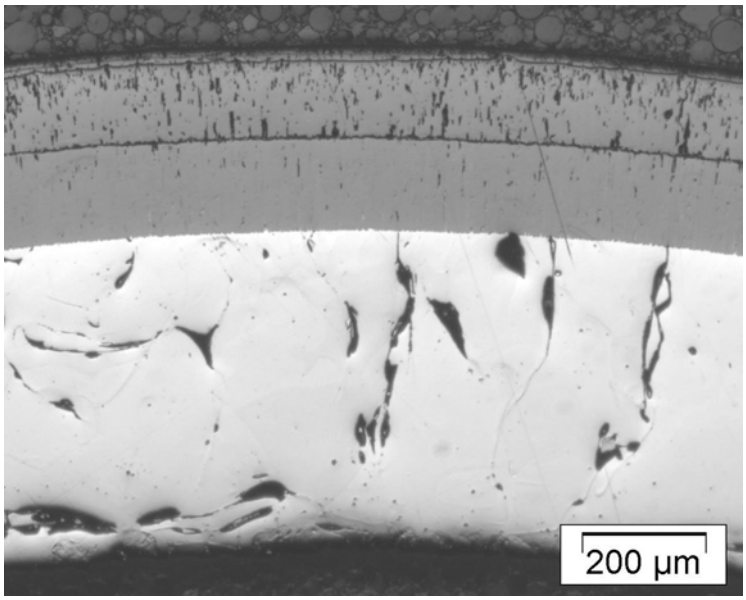

ZrO_2: 298 µm;
two sub layers
because of the Sn
redistribution

α-Zr(O): 513 µm

Test 280501_5: oxidation 1420°C during 1320 s

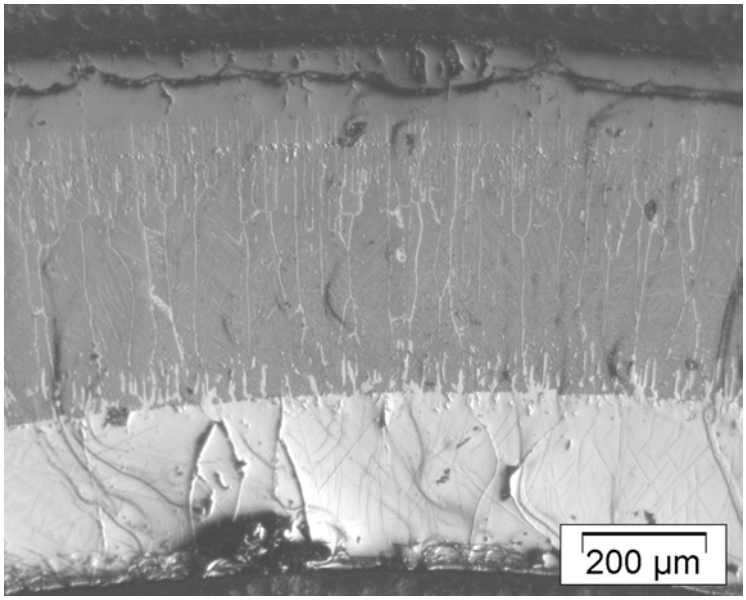

tetragonal ZrO_2:
123 µm

cubic ZrO_2:
446 µm

α-Zr(O): 286 µm

Test 280501_3: oxidation at 1500°C during 380 s

Fig. 31: Long duration tests with oxidation of Zry-tubes in the Ar (20 l/h) + O_2 (20 l/h) gas mixture

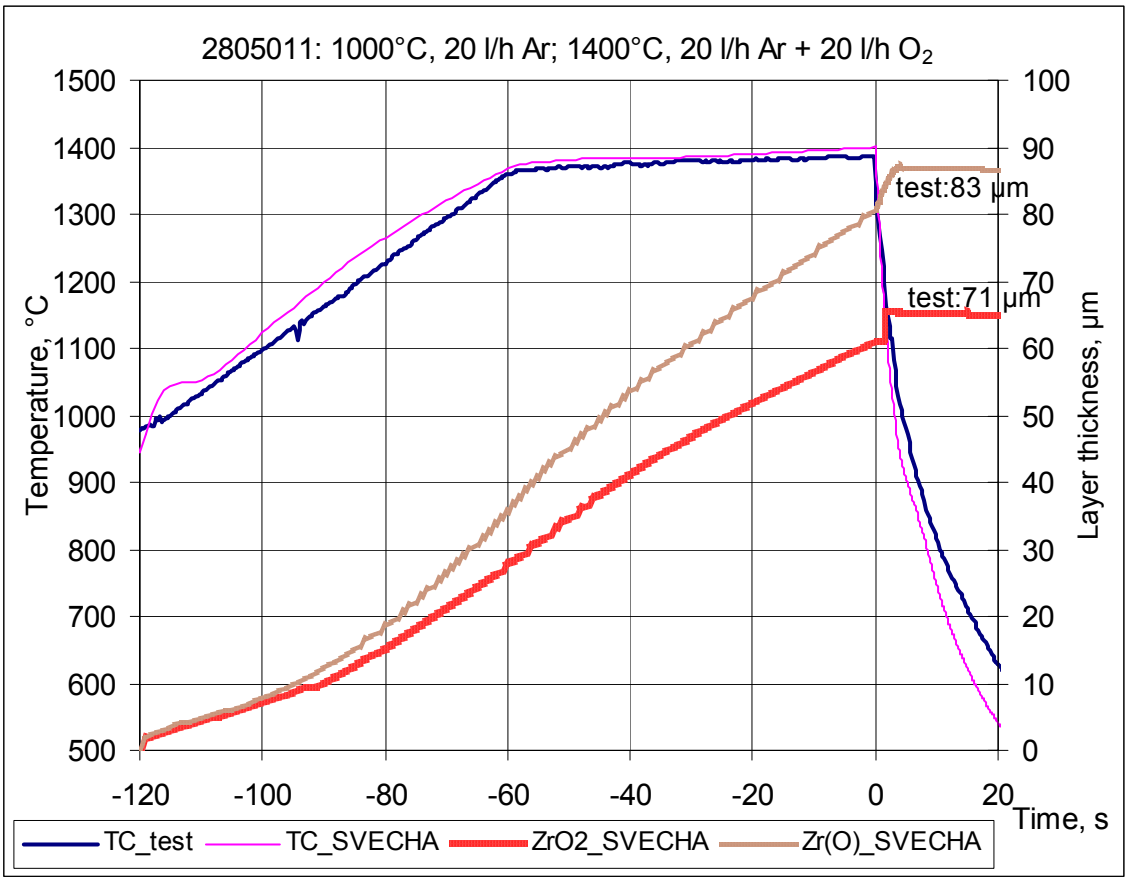

Fig. 32: SVECHA-modeling of the oxide layer growth during the test 2805011 (short time oxidation at temperature under 1500°C).

Picture shows the good agreement between experimental and modelling results

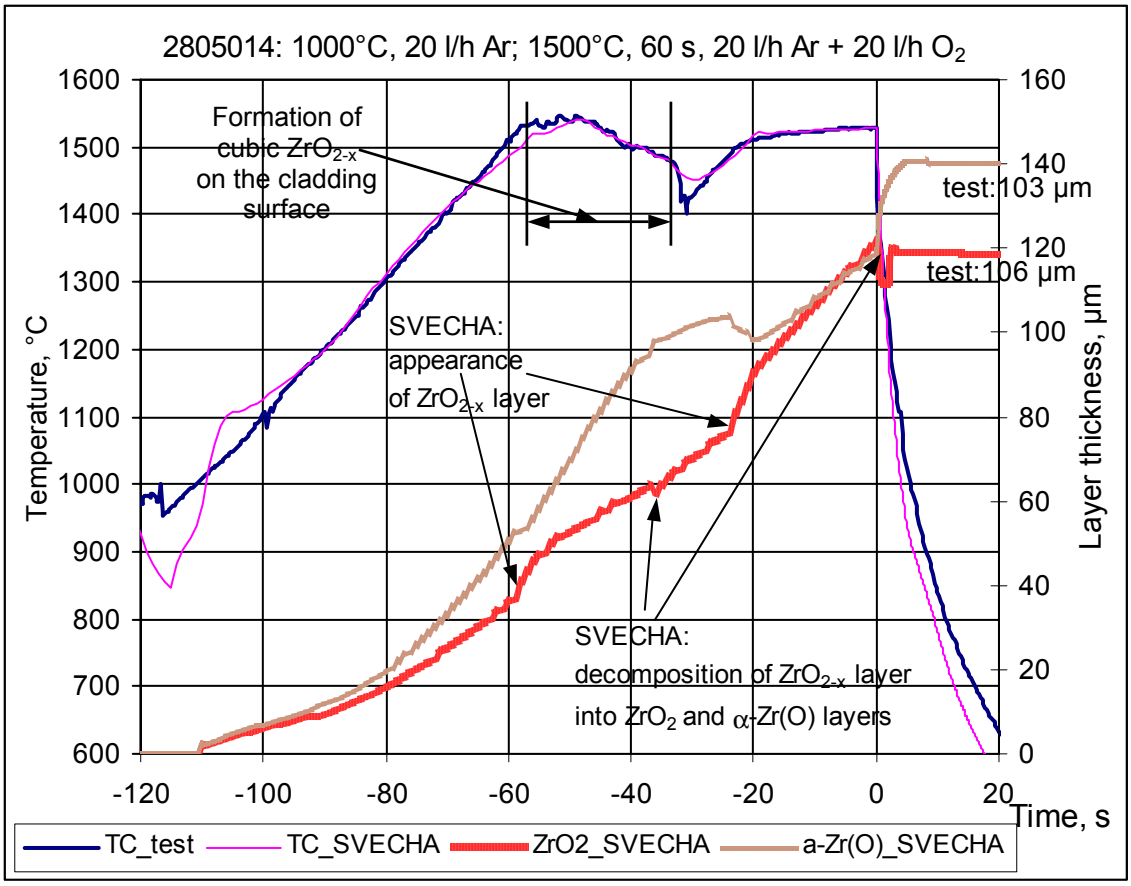

Fig. 33: SVECHA-modelling of the oxide layer growth during the test 2805014 (short time oxidation at temperature above 1500°C). Formation of cubic ZrO_{2-x} layer.

The model overestimates the layers thickness

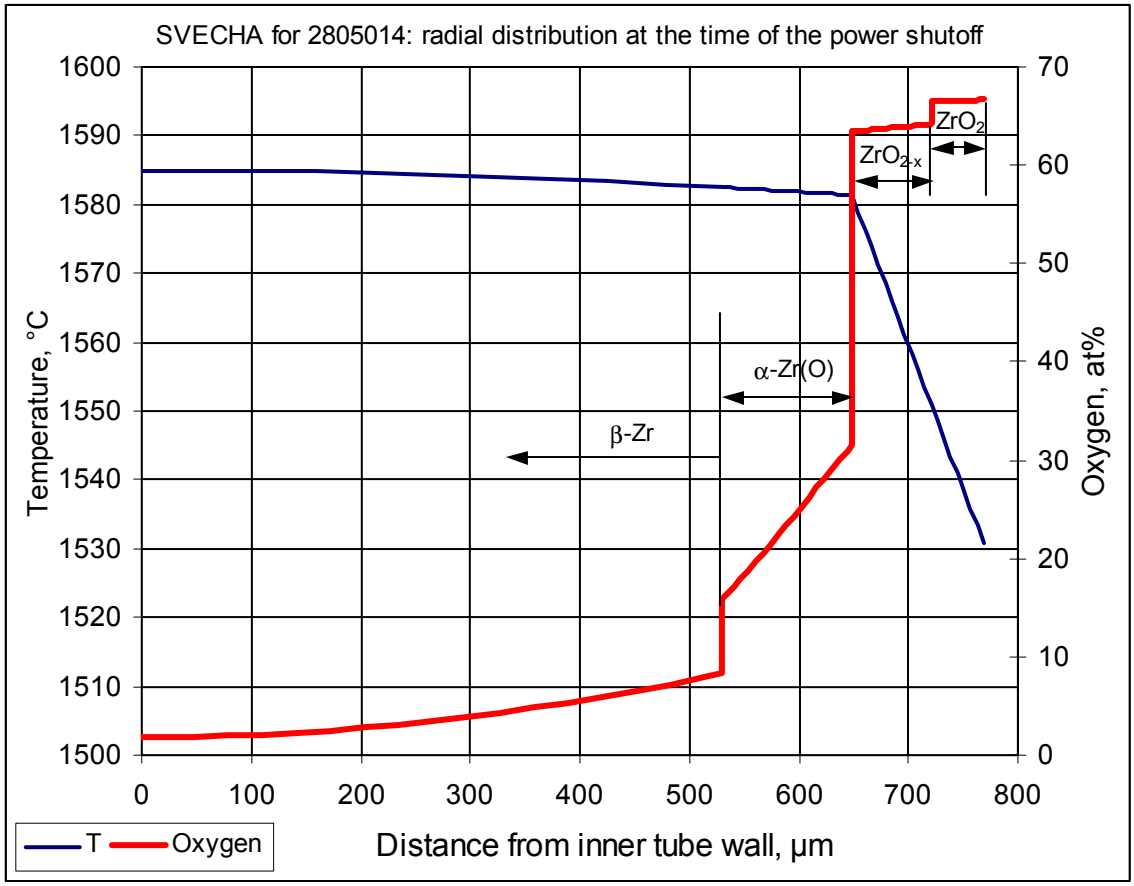

Fig. 34: SVECHA-modeling of the radial temperature and oxygen distributions at the time of the generator shutoff (test 2805014).

Strong overestimation of the cubic ZrO_{2-x} layer thickness: calculated value 70 µm, test value 15 µm

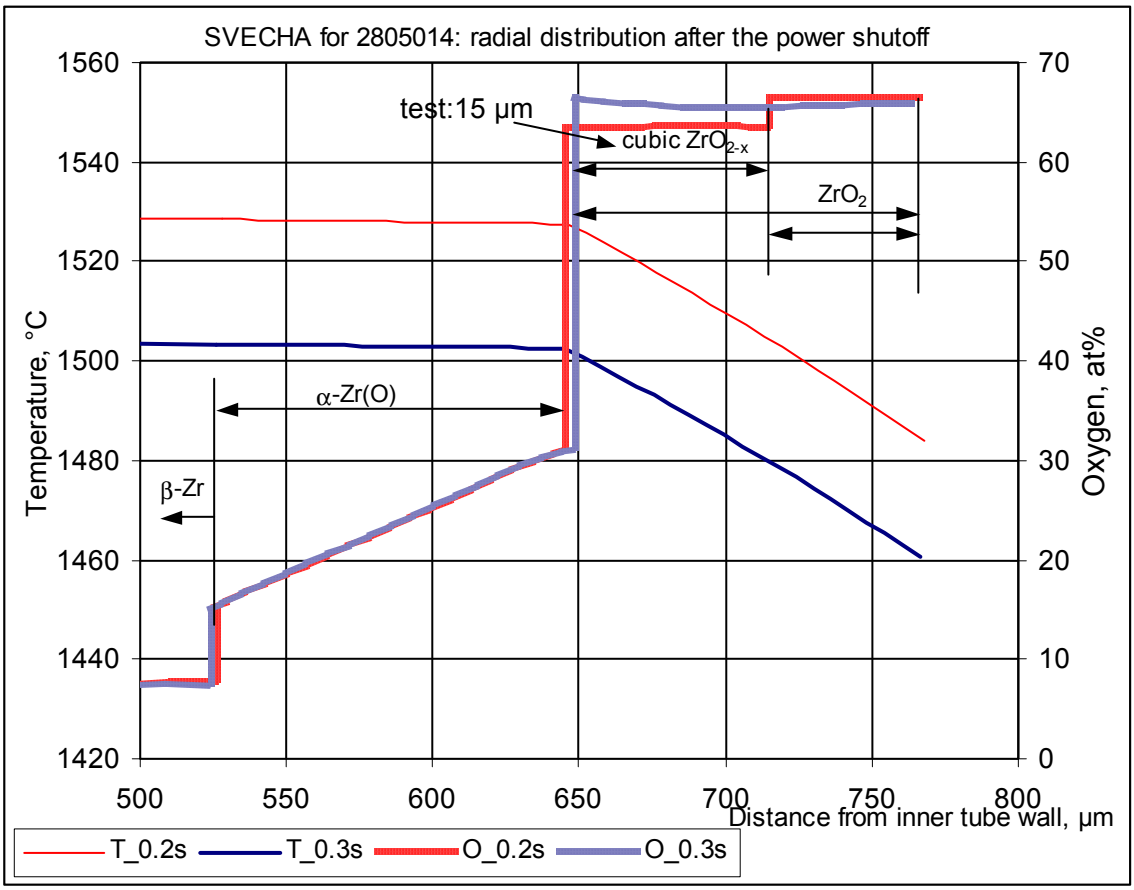

Fig. 35: SVECHA-modelling of the radial distribution of temperature and oxygen in the cladding at the time points 200 and 300 ms after the generator shutoff.

Model suggestion: transition of the ZrO_{2-x} layer in homogeneous ZrO_2 and α-Zr(O) layers

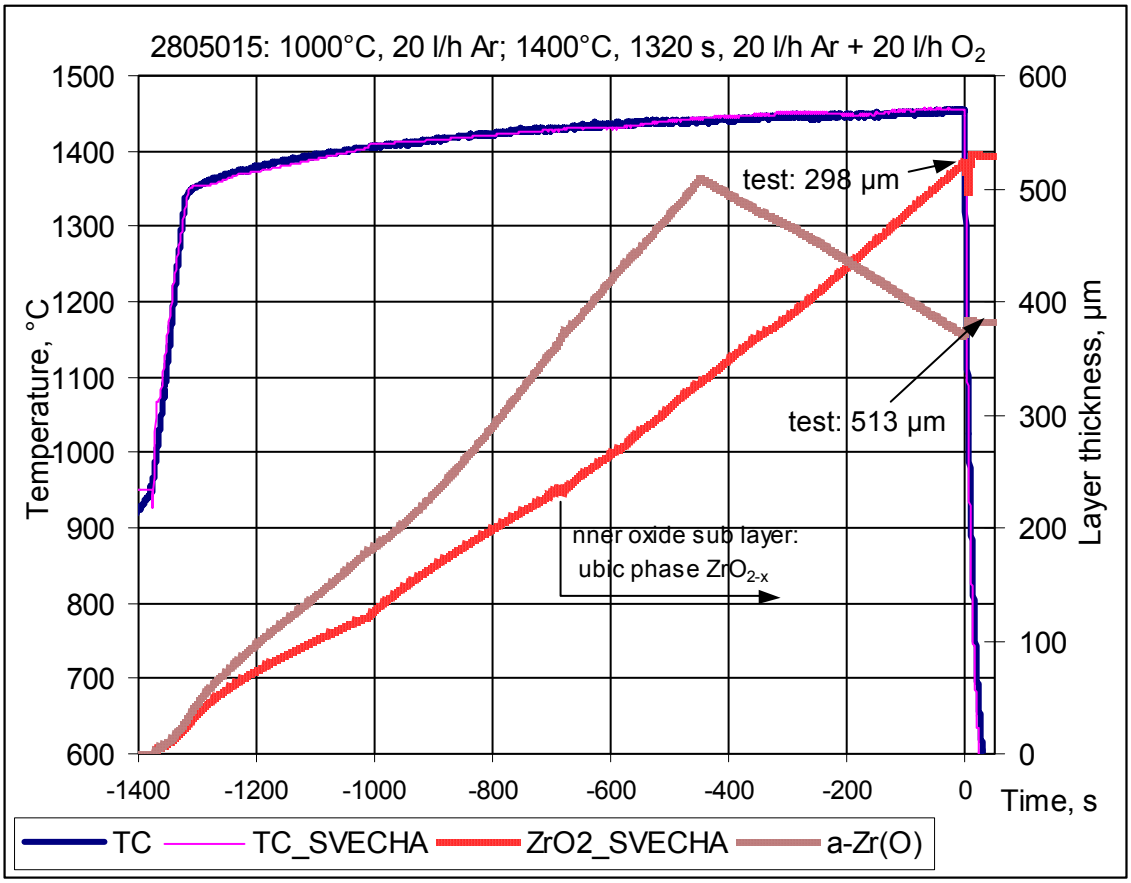

Fig. 36: SVECHA-modeling of the layer thickness growth during the test 2805015 (short time oxidation at temperature below 1500°C). Formation of cubic ZrO_{2-x} layer in contradiction to the test results.

The model overestimates the final layers thickness

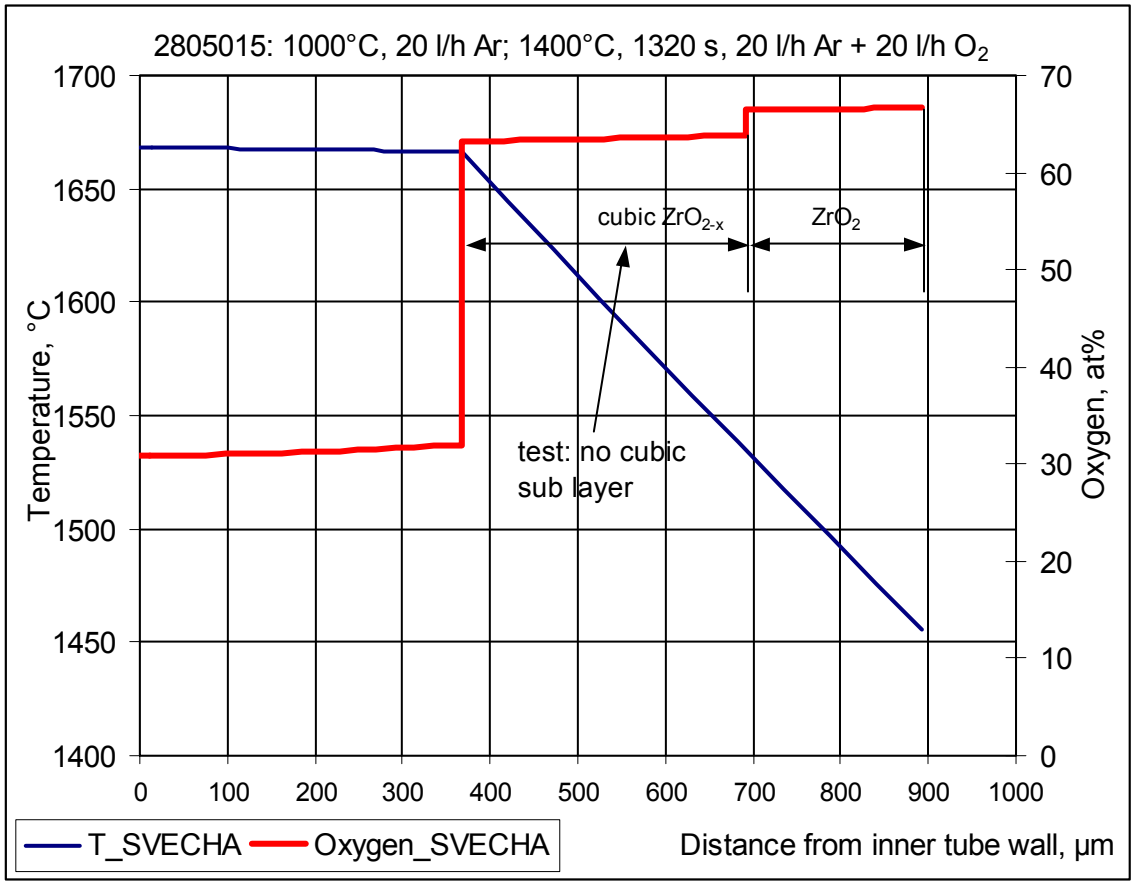

Fig. 37: SVECHA-modeling of the radial temperature and oxygen distributions at the time moment of the generator shutoff (test 2805015).

The temperature at the inner region of the oxide layer is higher than 1525°C. Cubic oxide should be formed in that region. But the experiment showed no formation of cubic oxide

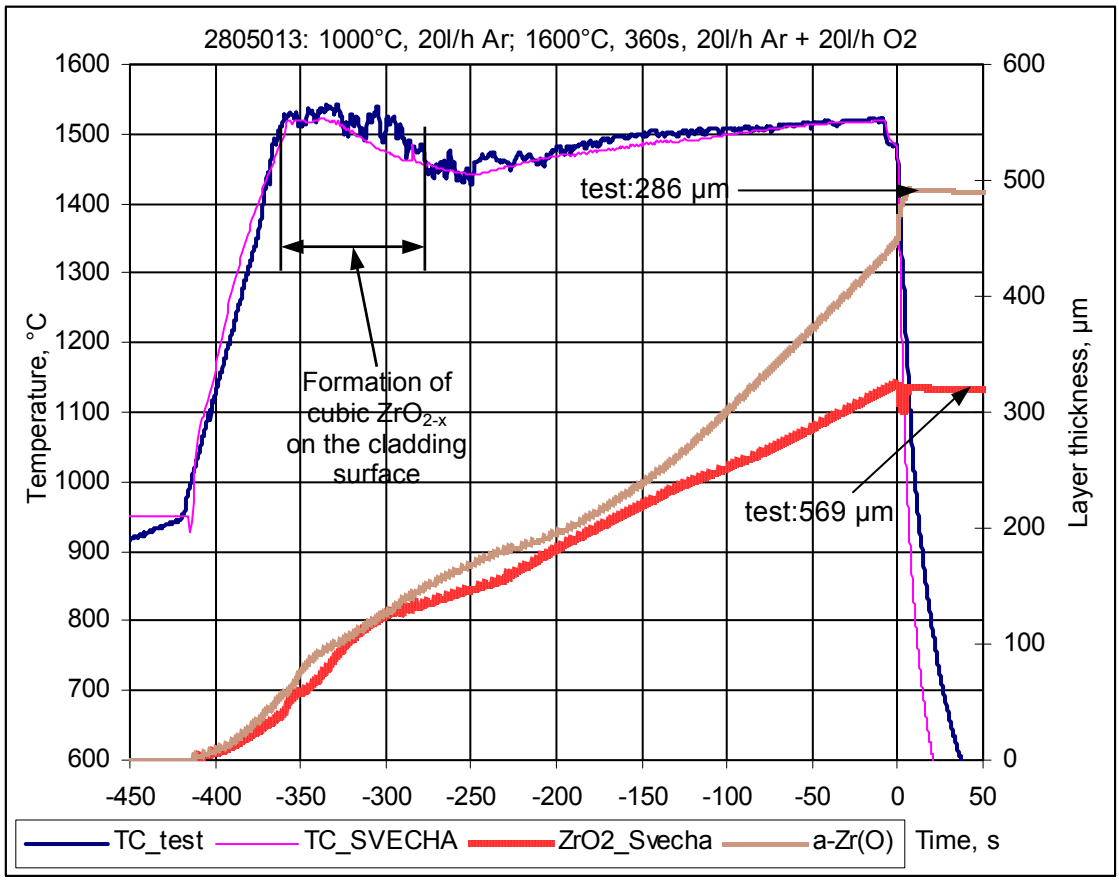

Fig. 38: SVECHA-modeling of the layer thickness growth during the test 2805013 (long time oxidation at temperature above 1500°C). Formation of cubic ZrO_{2-x} layer.

The model underestimates the layers thickness

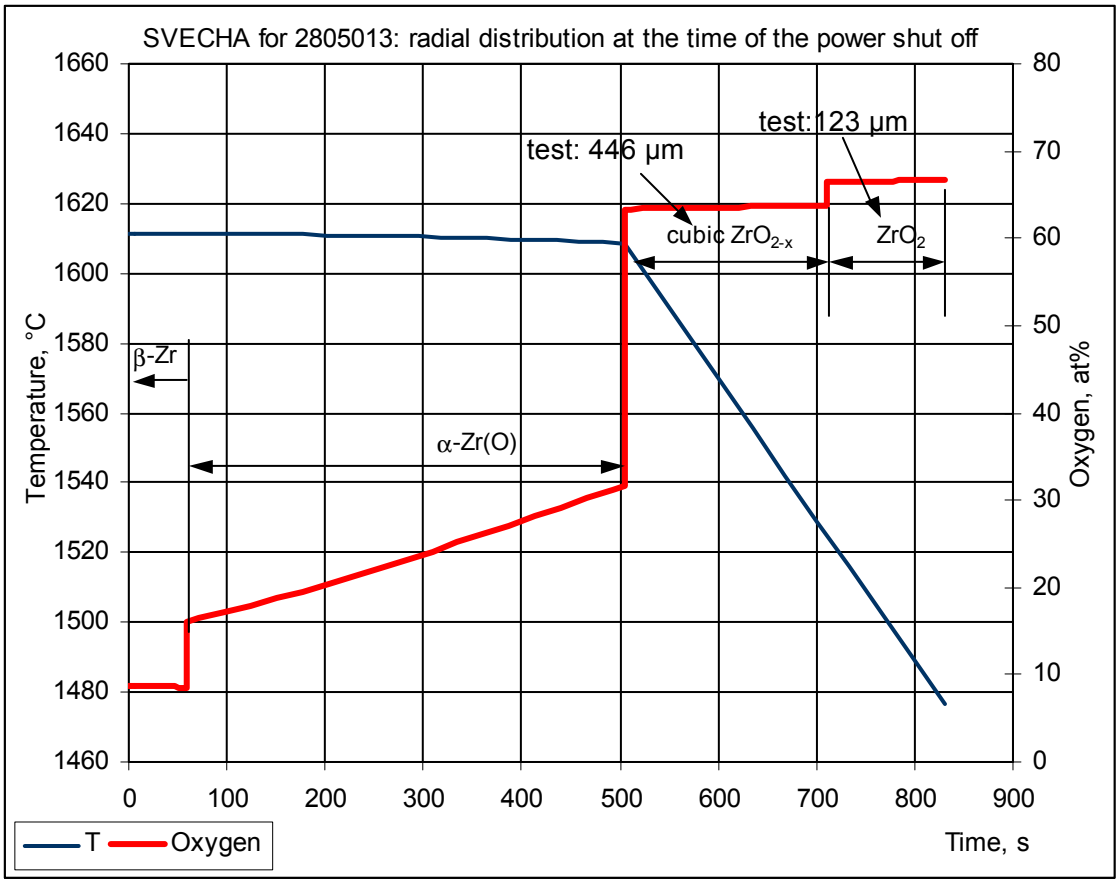

Fig. 39: SVECHA-modelling of the radial temperature and oxygen distributions at the time moment of the generator shutoff (test 2805013).

The model underestimates the thickness of the cubic oxide layer

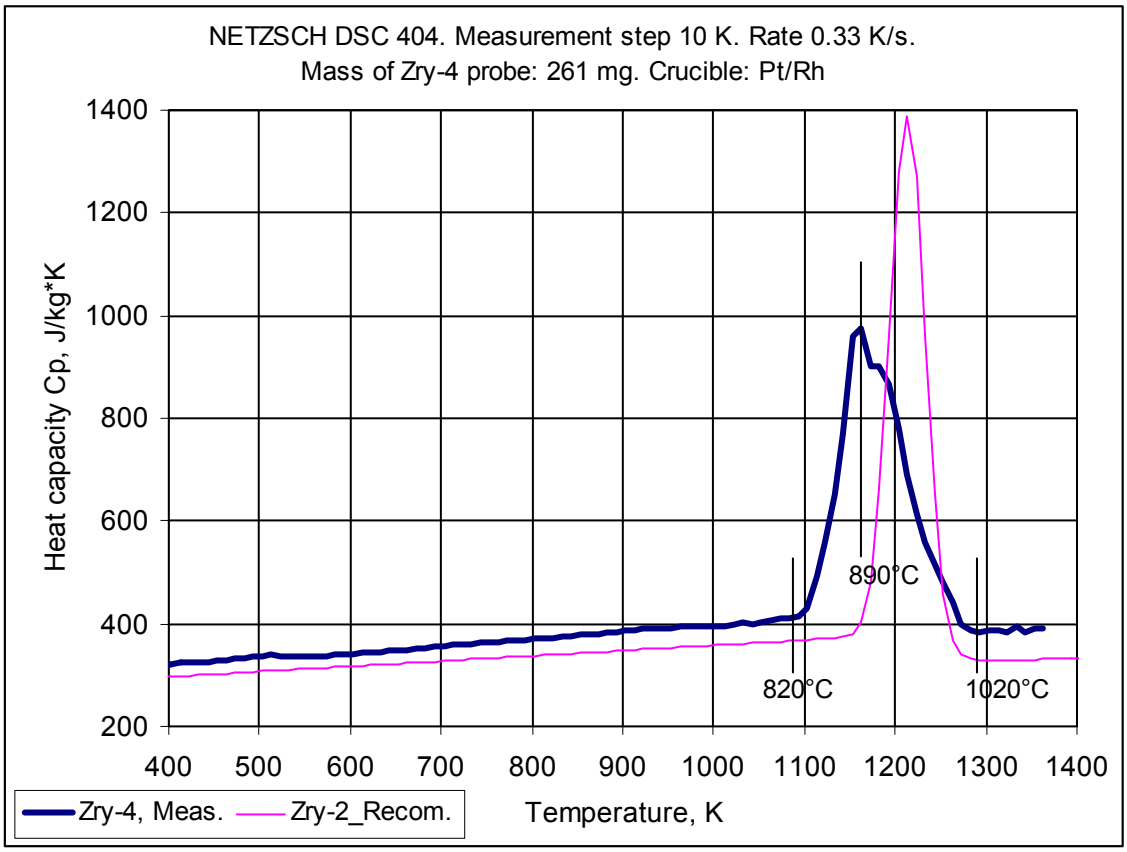

Fig. 40: Measurement of the specific heat capacity of Zry-4 gained by differential scanning calorimetric analysis

The curve recommended in the MATPRO (ANL) version for Zry-2 [8] is shown for comparison

Fitting curve for Zry-4:

For the α-phase, from 273 K < T < 1093 K,

$$C_p = 260.85 + 0.1371 \cdot T \tag{1}$$

with temperature in K and the heat capacity in J kg^{-1} K^{-1}.
For the β-phase from 1293 K < T< 2000 K

$$C_p = 634.6 - 0.4 \cdot T + 1.6 \cdot 10^{-4} \cdot T^2 \tag{2}$$

From 1093 K through 1173 K, in the α–β phase-transition region, the heat capacity of Zircaloy-4 calculates from the sum of Eq.(1) and a Gaussian function:

$$f(T) = 565 \cdot \exp\left[-\frac{(T-1163)^2}{1100}\right] \tag{3}$$

From 1173 K through 1293 K, in the α–β phase-transition region, the heat capacity of Zircaloy-4 calculates from the sum of Eq.(2) and a Gaussian function:

$$f(T) = 530 \cdot \exp\left[-\frac{(T-1183)^2}{2390}\right] \tag{4}$$

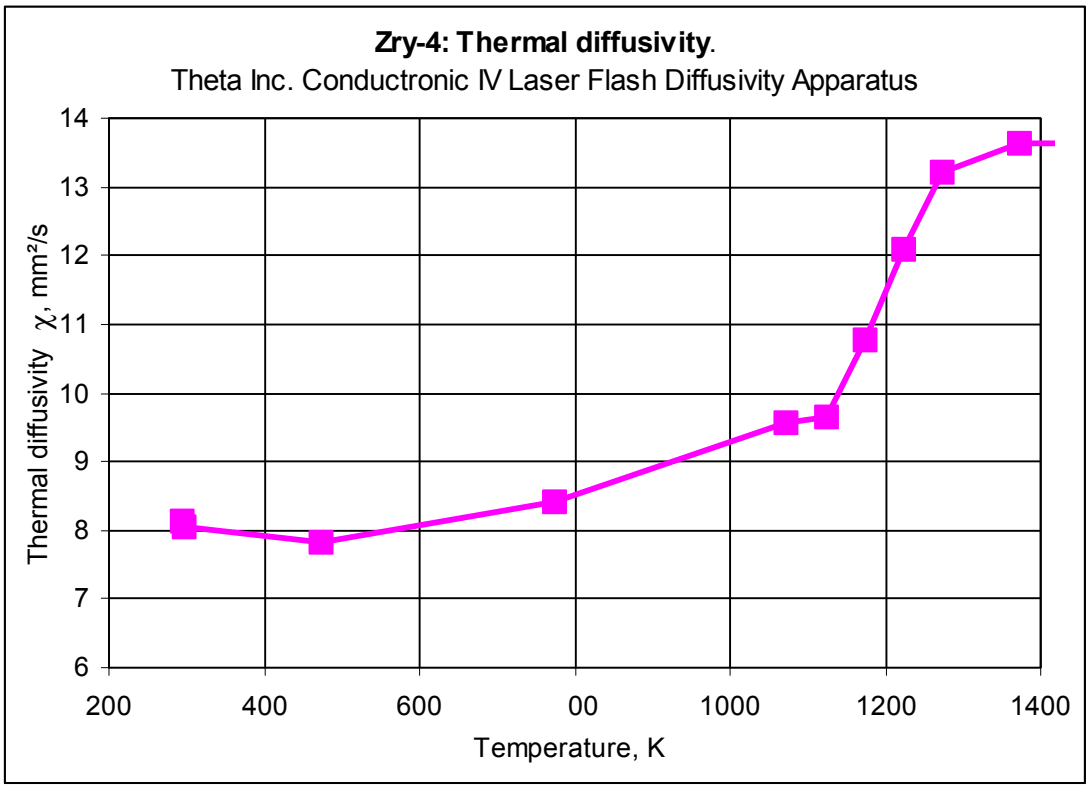

Fig. 41: Measurement of Zicaloy-4 thermal diffusivity as a function of temperature. Sample: disc with diameter 6 mm and thickness 0.3 mm

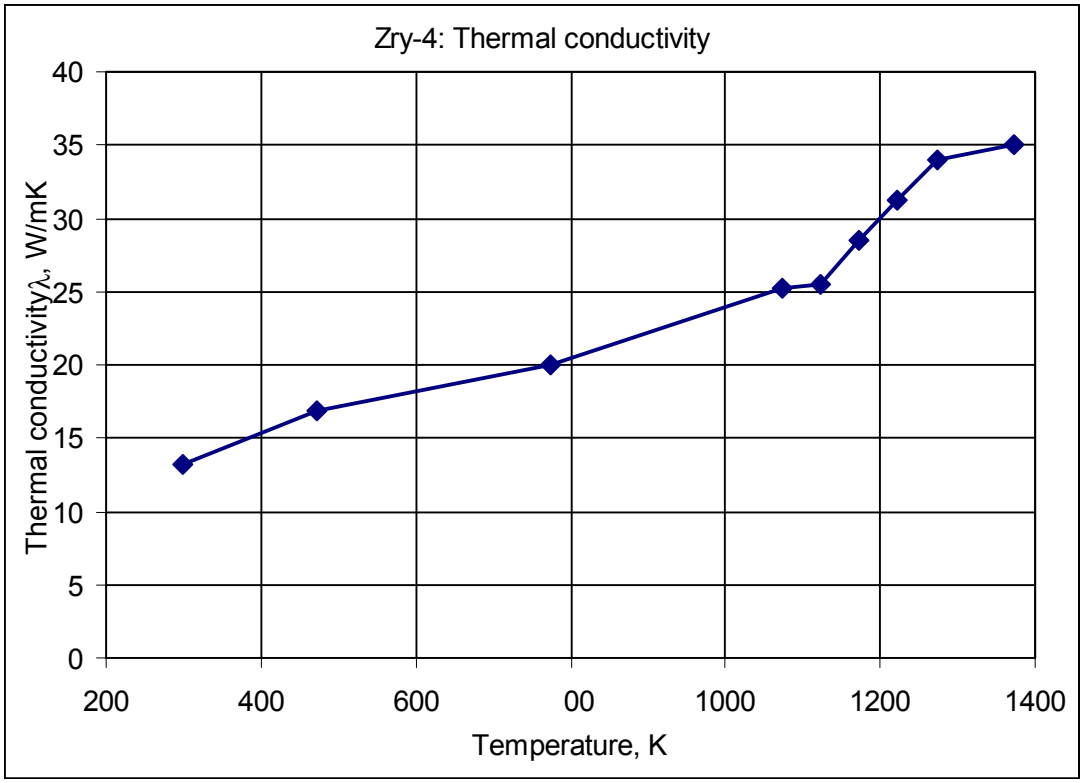

Fig. 42: Thermal conductivity of Zircaloy-4 as a function of temperature.

$\lambda = \rho \cdot C_p \cdot D$ (formula is valid outside of phase transition region), where specific heat C_p is given by Eq. (1)–(4), thermal diffusivity is presented in Fig. 41, density (for Zr) $\rho = 6595.2 - 0.1477 \cdot T$ if $T < 1173\,K$, $\rho = 6690 - 0.1855 \cdot T$ if $T \geq 1173\,K$ [3].

Part II: Determination of Zircaloy and ZrO_2 emissivities using experimental data of empty rods cool-down tests

A. V. Palagin

Nuclear Safety Institute
Russian Academy of Sciences, Moscow

1. Introduction

Emissivity is an important property of the reactor-related materials. Under severe accident conditions the temperature of the core may reach 1500-2000 K or even more. At such high temperatures the main role in the heat exchange play radiative heat flows. In order to describe adequately the temperature distribution inside the core and predict the evolution of severe accident it is necessary to know the temperature dependence of the emissivity of the materials used in reactor design. The most important is cladding material – Zirconium or Zirconium Dioxide, which appears as a result of cladding oxidation in steam atmosphere.

It should be noted that existing data concerning Zr and ZrO_2 emissivity at high temperatures can not be characterised as complete. Thus, in SCDAP/RELAP5 code materials properties database MATPRO [1] only ZrO_2 emissivity is cited, based on the works published before 1977. Zr emissivity data are absent in [1].

In some recent works measurements of Zr emissivity were performed. In [2] the spectral emissivity at wavelengths 1.0 μm and 2.3 μm in the temperature interval 1373-1923 K was measured. In [3] the total emissivity of Zr in the temperature interval 1400-2000 K was determined. In [4] the spectral emissivity of Zr at wavelength 0.65 μm in the temperature interval 1000-2100 K was measured.

In all these works as well as in the previously done ones the optical methods were used for the determination of the emissivity value and mainly spectral emissivity was measured. At the same time, for the description of the radiative heat exchange only total emissivity value is necessary. In this connection it seems to be interesting to determine the total emissivity value by another way: on the basis of cool-down tests data.

At high temperatures the radiative heat flow from the surface of a body exceeds considerably the heat flow to surrounding gas. By calculating the heat flow from the surface using measured surface temperature evolution one can estimate the value of emissivity. Additional accounting for the heat flow to the gas improves the accuracy of such estimation.

In the present report the first results of the determination of Zr and ZrO_2 emissivity on the basis of empty rods cool-down tests temperature data are described. The material of the rod was Zircaloy-4 (one of the Zr alloys often-used in reactor design). From here on we will use the ‘Zr’ sign to mean Zircaloy-4 material in order to save place. Quench rig experimental facility and the details of the test conduct are

described in the Part I of the present report. The calculation of the heat flow from the rod surface was performed with the help of SVECHA/QUENCH code (S/Q) [5]. The data used cover temperature interval 700-1800 K.

On the basis of four cool-down tests with non-oxidised Zr rod the value of emissivity was estimated and 9-parameters fitting curve for the its temperature dependence was proposed. Using five cool-down tests with oxidised Zr rod the value of ZrO_2 emissivity was also estimated. However, due to large data scattering, no fitting curve was proposed. The uncertainty factors which affect the accuracy of the described method are discussed.

2. Theory

Heat flow from the rod surface is given by the sum of radiative heat flow and convective heat flow:

$$F_s = F_{s,rad} + F_{s,cond} = \frac{\sigma\left(T_s^4 - T_{env}^4\right)}{\frac{1}{\varepsilon_s} + \left(\frac{1}{\varepsilon_{env}} - 1\right)\frac{R_s}{R_{env}}} + Nu \cdot \lambda_g \frac{T_s - T_g}{h} \quad (1)$$

Here ε_s, T_s and R_s are the emissivity coefficient, temperature and radius of the rod outer surface; ε_{env}, T_{env} and R_{env} are the emissivity coefficient, temperature and radius of the structure which surrounds the rod in the experimental facility, Nu is Nusselt number, characterising convective heat exchange in the channel, λ_g is the thermal conductivity of the gas, T_g is the gas temperature, h is hydraulic diameter.

Rod surface emissivity ε_s may be expressed in terms of the above heat flow parameters:

$$\varepsilon_s = \left[\frac{\sigma\left(T_s^4 - T_{env}^4\right)}{F_s - Nu \cdot \lambda_g \frac{T_s - T_g}{h}} - \left(\frac{1}{\varepsilon_{env}} - 1\right)\frac{R_s}{R_{env}}\right]^{-1} \quad (2)$$

Time dependence of the rod surface temperature $T_s = T_s(t)$ is known from the experimental measurements. The value of heat flow from the rod surface $F_s = F_s(t)$ may be calculated by the S/Q code by specifying experimentally measured temperature of the rod surface $T_s = T_s(t)$ as input boundary condition. Channel gas temperature $T_g = T_g(t)$ also may be calculated by the S/Q code.

Thus, all the parameters needed for the determination of the emissivity value may be determine on the basis of the rod cool-down temperature measurements and S/Q code calculations.

3. Non-oxidised rod cool-down tests

3.1. Test data used

Heat flow to the gas is one of the factors which affect the accuracy of the present method. The errors in estimation of the gas temperature or the value of Nusselt

number will lead to the errors in the emissivity coefficient determination. At the same time, since heat flow to the gas is proportional to the temperature difference between the rod surface and the gas, increase of the gas temperature will result in the decrease of the heat flow to the gas, and consequently, in the decrease of the uncertainty introduced by this heat flow.

Since the highest gas temperature during the test was at the upper part of the channel, the temperature data measured by the upper TC (130 mm elevation) in the non-oxidised rod cool-down tests were used for Zr emissivity coefficient determination. The tests under consideration are presented in Table 1.

Test	**10222a**	**10222b**	**10301a**	**10301b**
Initial temperature, C	**1140.9**	**1144.4**	**1090.0**	**1087.8**

Table 1. Cool-down tests with non-oxidised rods

3.2. Smoothing of the temperature data

In the experiments with cool-down of empty rods the heat flow from the rod surface is connected very closely with the time derivative of the surface temperature dT_s/dt (in the limit of very thin rod and temperature-independent heat capacity these values are proportional to each other). In order to perform the preliminary estimation of the value of the heat flow the time derivative of the rod surface temperature was calculated. As one can see (Fig.1, red curve), the value of dT_s/dt experiences very sharp oscillations.

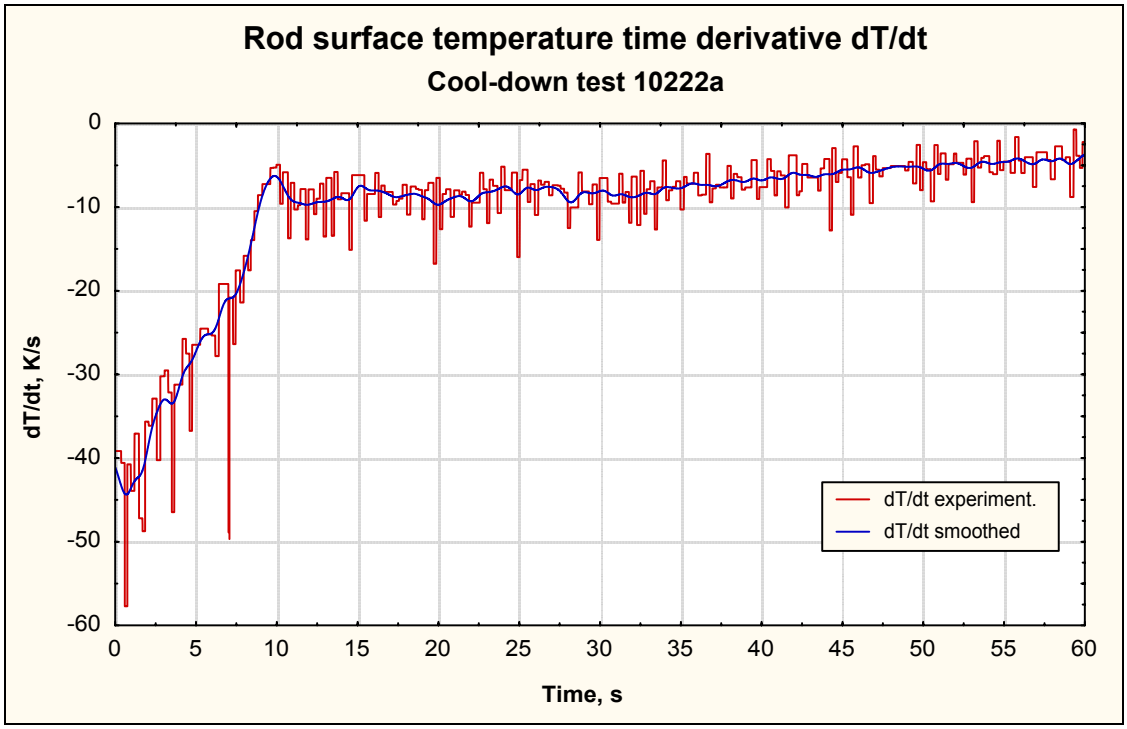

Fig. 1. Rod surface temperature time derivative for 10222a cool-down test. Experimental measurements (red curve) and smoothed data (blue curve)

The reason of these sharp oscillations consists in small errors in temperature measurements. As one can see in Fig.2, experimental data points deviate from some “average smooth curve” by several degrees. These small deviations do not seem to play any considerable role when estimating the whole picture of temperature evolution during cool-down. However, when calculating temperature derivative (or calculating heat flow from the rod surface with the help of S/Q code) these small deviations result in rather big and sharp oscillations of the above values.

In order to avoid large data scattering some smoothing of the temperature cool-down curves were performed. Due to the fact that experimental data deviations are rather small, standard smoothing procedures (described, for example in [7]) can not be applied directly in this situation. That is why as a first step the temperature derivative curve was smoothed (see Fig.1), and then this smoothed curve was integrated in order to obtain the new temperature curve (Fig.2 and Fig.3).

These smoothed temperature evolution curves were used for the calculation of the heat flow from the rod surface described in the next subsection. The original (non-smoothed) experimental curves were also used for the heat flow calculations in an effort to estimate the effect of temperature measurement errors.

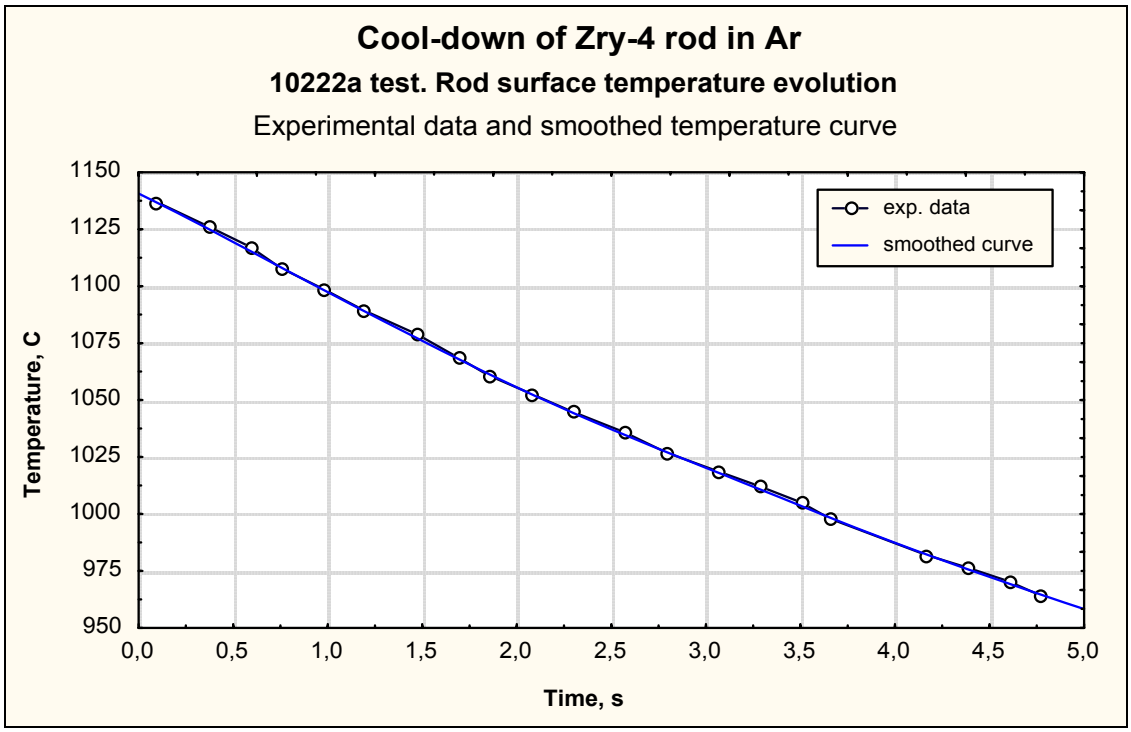

Fig. 2. Rod surface temperature evolution. 10222a cool-down test. Experimental measurements and smoothed curve. Time interval 0 – 5 sec

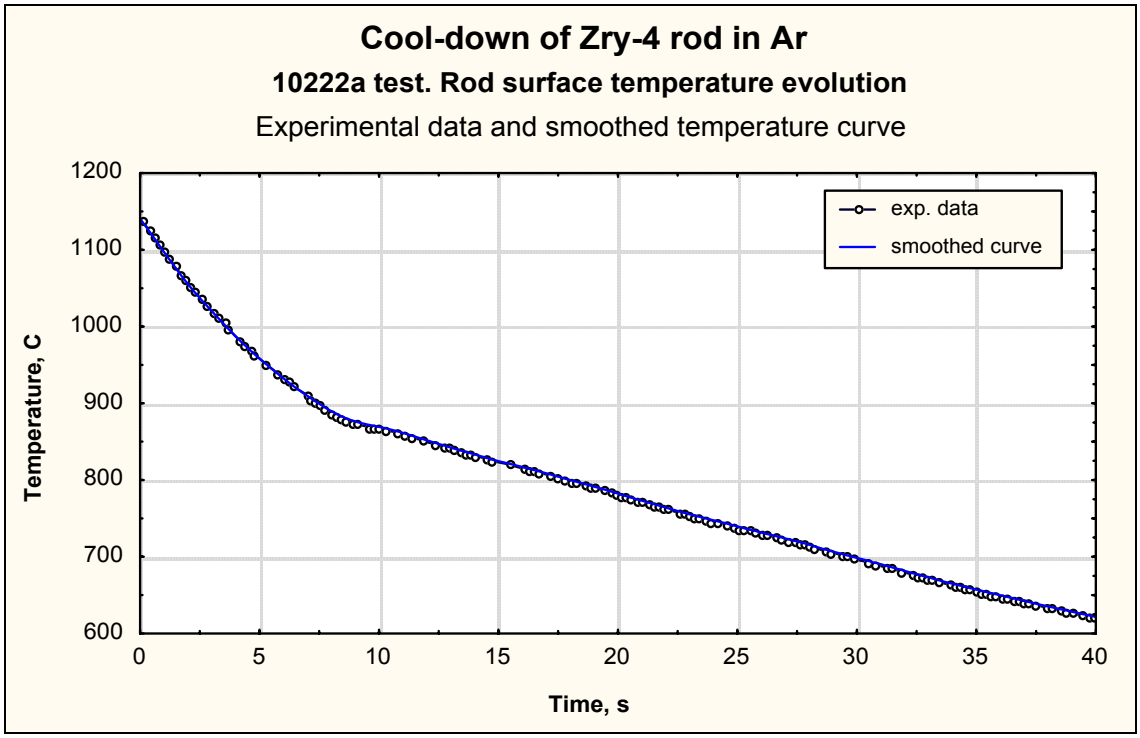

Fig. 3. Rod surface temperature evolution. 10222a cool-down test. Experimental measurements and smoothed curve. Time interval 0 – 40 sec

3.3. Heat flow calculation procedure

For the adequate description of the rod cool-down process and determination of the heat flow from the rod surface it is very important to know:

- thermal properties of the rod material,
- temperature distribution inside the rod at the moment of cool-down beginning (initial conditions).

In the case of non-oxidised rod there was only one Zr metal phase with well-defined thermal properties. The only parameter to control at the pre-heating stage of the test simulation was the rod external surface temperature.

In the real experiment conditions the external surface temperature is constantly checked by a pyrometer connected by a feed-back link with the power generator and so, heat generation rate is automatically tuned in order to keep the desired rod temperature.

In the course of test simulation the value of the heat generation rate density ($J/m^3 s$) should be specified in the S/Q code input file. We note here, that heat generation rate is not measured during the test and so, one has to determine this parameter independently.

Since the thickness of the metal layer in the course of preheating at some fixed temperature does not changed, the heat generation rate density in such stationary situation should be also constant. Thus, in the case of the tests with non-oxidised rods, one have to evaluate only one fixed value – heat generation rate density – which determine the heat exchange of the rod. Due to the accounting for the real thermal properties of the rod (heat capacity, density, thermal conductivity), the

temperature distribution inside the rod at the pre-heating stage will be self-consistently calculated by the code.

In the course of the test simulation performed in the present work, the rod was heated up with a certain internal heat generation to the desired temperature (equal to the initial temperature at the beginning of cool-down) and kept at this temperature for 60 sec.

After that the cool-down stage of the test simulation was started using temperature distribution inside the rod established at the end of pre-heating stage as initial conditions. As for the boundary conditions, they were determined by the temperature cool-down curves. The rod surface temperature was set equal to the measured one and the heat flow from the rod surface in the course of cool-down was calculated by the S/Q code.

It should be noted, that the description of the rod heat exchange process in the S/Q code is based on the specification of the *heat flow* from the rod surface. Within the framework of the S/Q thermal-hydraulic model the heat flow from the rod surface is determined as a function of gas flow parameters. From the mathematical point of view specification of the heat flow from the surface (more accurately, specification of the temperature radial gradient on the surface at the heat conduction module time step) represents boundary condition of the *second kind*. Indirect specification of the rod surface temperature as boundary condition for the heat conduction problem (boundary conditions of the *first kind*) was realised by introduction certain modifications in the S/Q code.

So, in the performed calculations this indirect specification of the rod surface temperature as boundary condition for the calculation of the heat flow was used. Calculated heat flow at the upper TC elevation in 10222a test is presented in Fig.4.

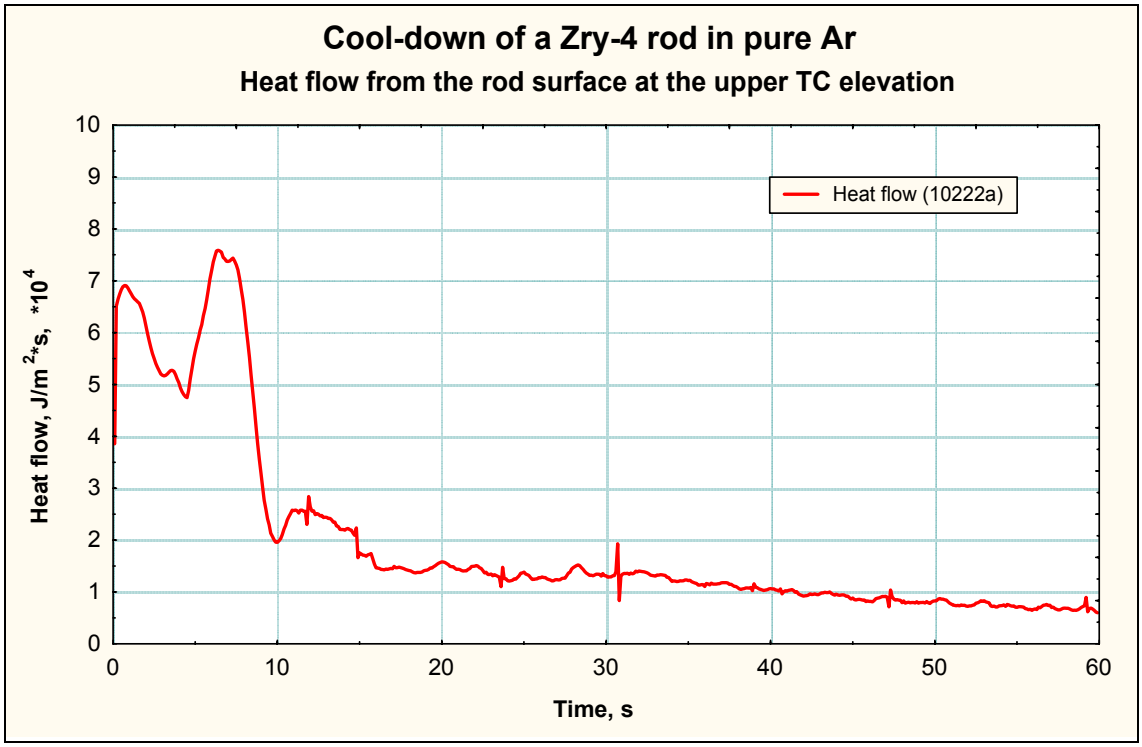

Fig. 4. Heat flow form the rod surface at the upper TC elevation in 10222a test

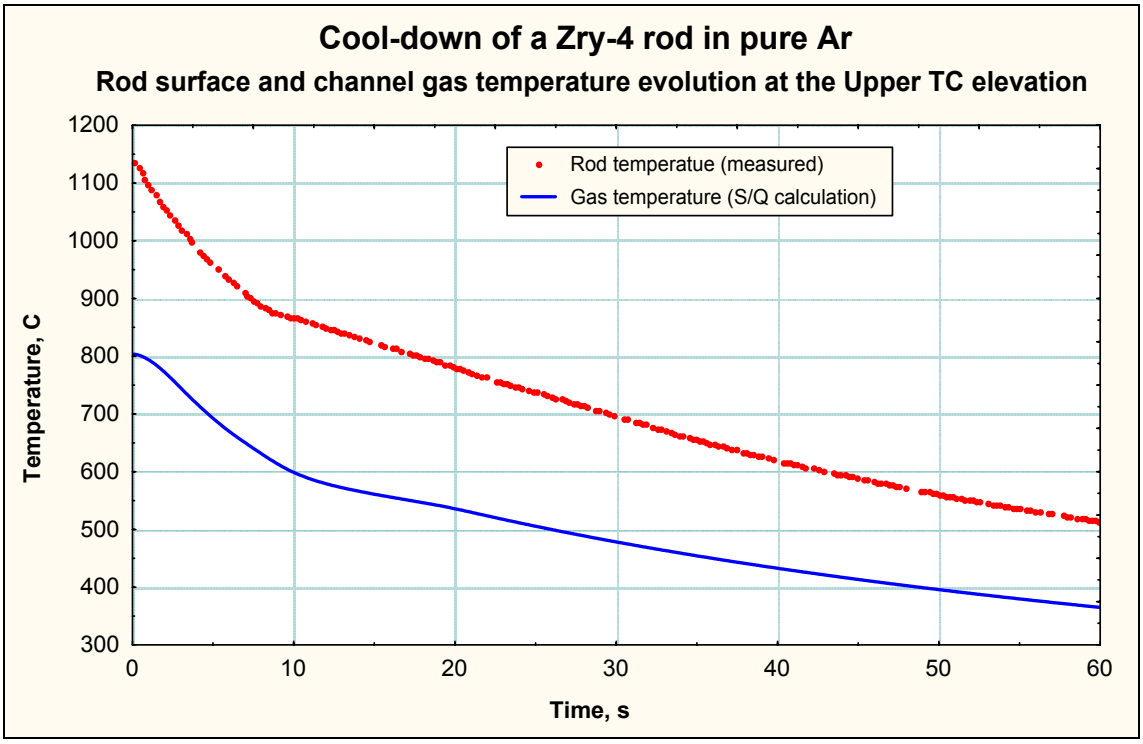

Fig. 5. Measured rod surface temperature (10222a test) and calculated gas temperature at the elevation of the upper TC (130 mm)

The gas temperature time dependence necessary for the emissivity calculation (see eq. (2)) was taken from direct simulation of the cool-down process by the S/Q code. In Fig.5 one can see time evolution of measured rod surface temperature (10222a tests) and calculated gas temperature at the elevation of the upper TC (130 mm).

3.4. Zr emissivity calculation

After determination of the heat flow the emissivity coefficient value was calculated in accordance with eq.(2).

The obtained results for all four non-oxidised rod tests are presented in Fig.6 (based on the non-smoothed original experimental curves) and Fig.7 (based on smoothed curves). One can see huge data scattering in the case of non-smoothed original experimental curves. At the same time, in the case of smoothed curves data scattering is rather small and all four curves perfectly correlate with each other.

The obtained temperature dependence of Zr emissivity has considerable maximum at about 1180 K. The position and the magnitude of this maximum correlates with the maximum in the temperature dependence of Zr heat capacity $C_{Zr}(T)$. In S/Q code calculations the temperature dependence of $C_{Zr}(T)$ given in SCDAP/RELAP5 code materials properties database MATPRO [1] was used (see Fig.8).

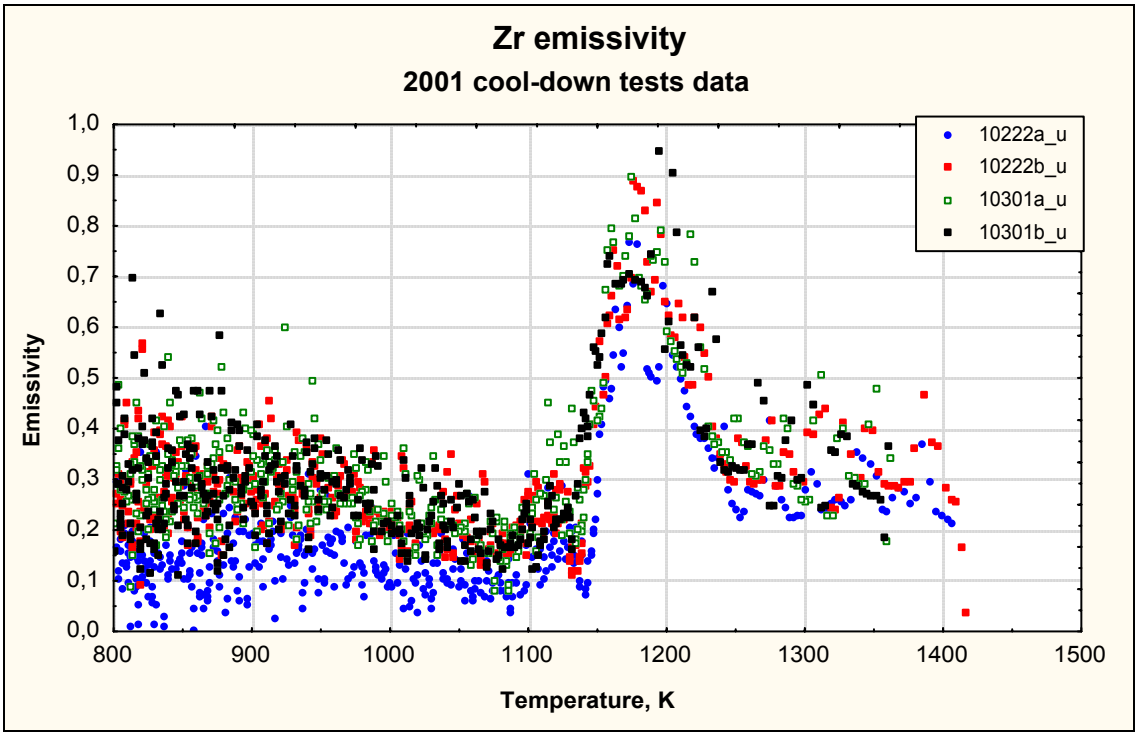

Fig. 6. Zr emissivity coefficient calculated on the basis of non-smoothed original experimental temperature curves

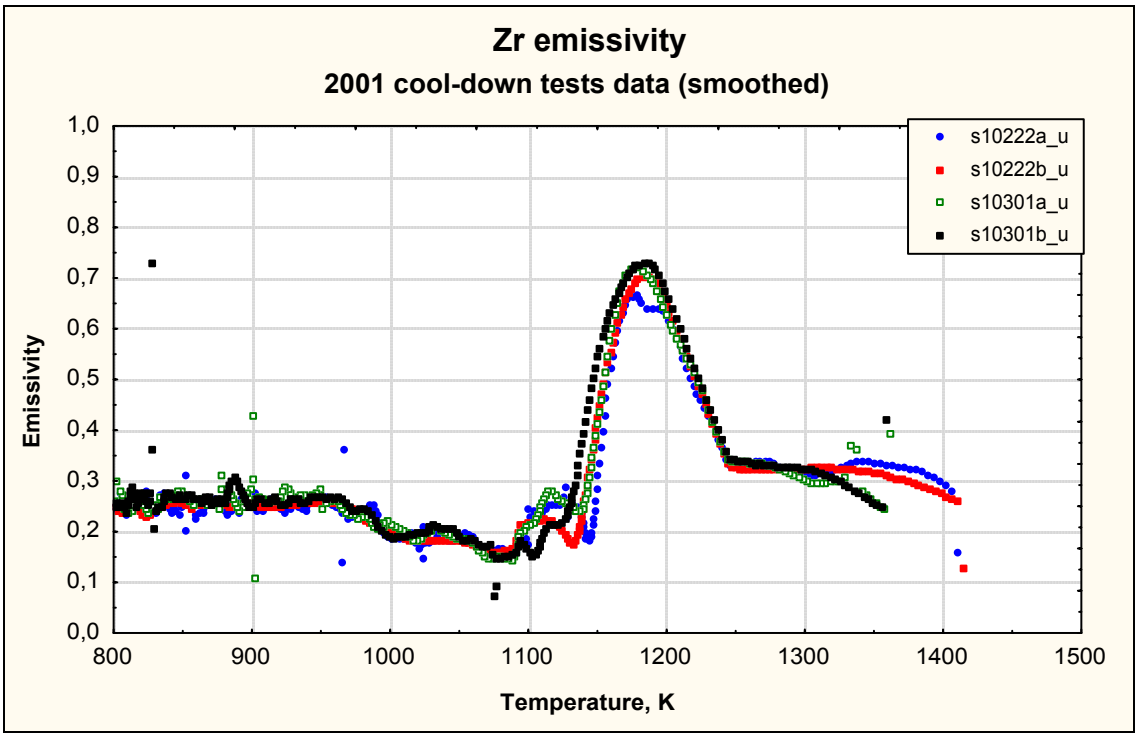

Fig. 7. Zr emissivity coefficient calculated on the basis of smoothed temperature curves

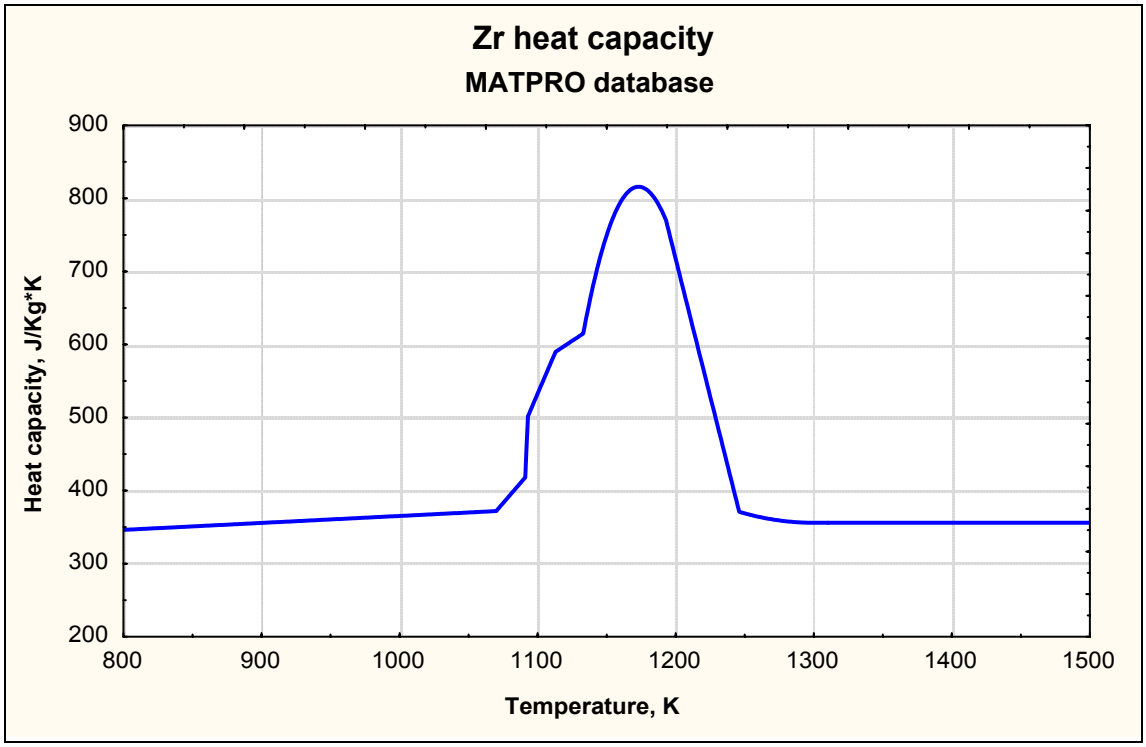

Fig. 8. Zr Heat capacity temperature dependence (from MATPRO [1])

The reason of this maximum in temperature dependence of $C_{Zr}(T)$ is $\alpha \rightarrow \beta$ phase transition. Zr emissivity may also experience some kind of peculiarity in the phase transition temperature region. However, if temperature dependence of heat capacity of the real material used in the cool-down tests under consideration differs from the one given in MATPRO [1], such difference may lead to errors in the emissivity value in this temperature region. Thus, deficient knowledge of real heat capacity temperature dependence is one of the factors which limit the accuracy of the our method and introduce an uncertainty in the results.

3.5. Comparison with other experimental data

In Fig. 9 one can see the comparison of the described cool-down tests data with the available emissivity data obtained by optical methods in the recent work [3], and also in the work [8] cited in the handbook [9] and in the book [10] cited in the handbook [11].

One can say, that generally the results obtained in the present work are not in a contradiction with the previous ones. The only exception is one point from [10], measured at 1200 K ($\varepsilon = 0.214$). At this temperature the emissivity temperature curve obtained in the present work experiences rather sharp maximum. This maximum correlates with similar maximum of heat capacity temperature dependence (see above, subsec. 3.4). Contradiction between cool-down tests data and optical measurements in this temperature region may indicate that, as it was pointed out in subsec. 3.4, there were certain errors in heat capacity temperature dependence determination, resulting in too sharp maximum of the emissivity temperature curve.

On the other hand, there is only one point measured at 1200 K, which 'drops out' from the general tendency and which seems to be inconsistent with the data from [8] measured at 1140 K ($\varepsilon = 0.33$) and 1300 K ($\varepsilon = 0.39$).

In order to clarify this situation new tests are necessary, both cool-down and optical ones. Also, independent measurements of Zr heat capacity in the temperature interval of interest would be very helpful for the improvement of the cool-down method accuracy.

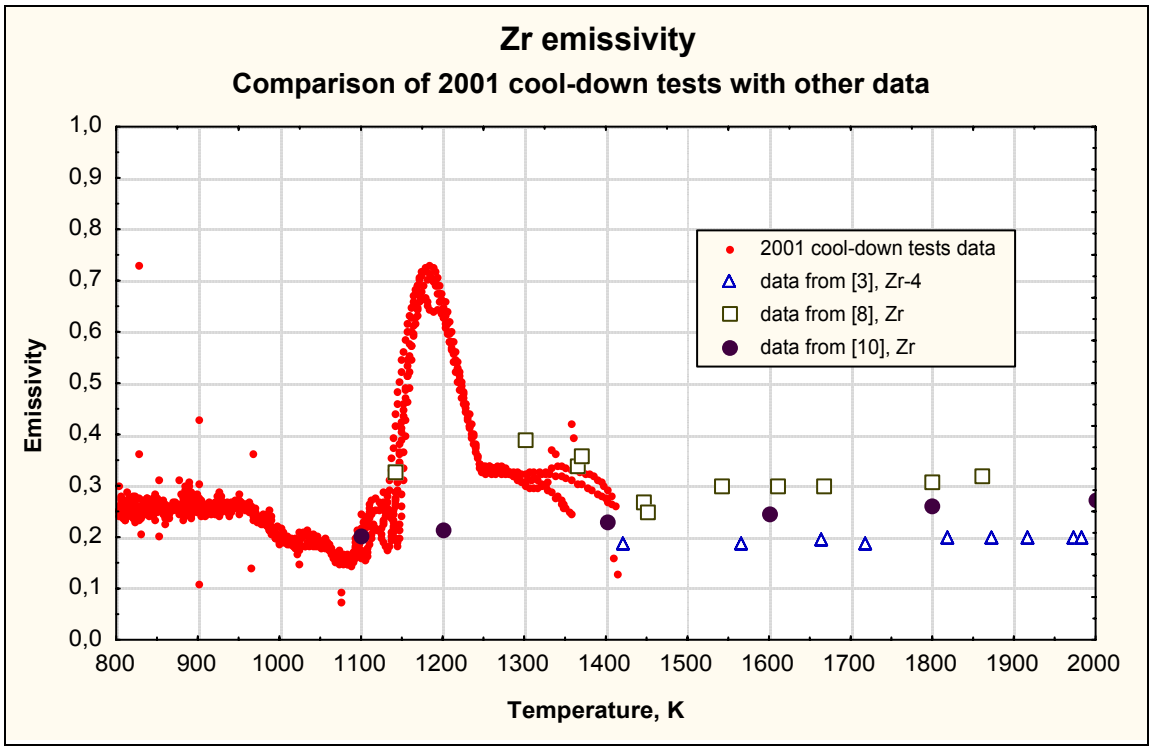

Fig. 9. Comparison of the present cool-down tests data with the results of emissivity determination by optical methods

3.6. Effect of heat flow to the gas

Using the obtained data the effect of heat flow to the gas on the calculated Zr emissivity can be estimated. In Fig.10 the results of three calculations in accordance with relation (2) are presented. In the first calculation heat flow to the gas was not accounted for (i.e. second term in relation (1) was omitted). In the second calculation heat flow to the gas was accounted for and gas was heated (gas temperature time dependence was calculated by S/Q code, see Fig.4). In the third calculation heat flow to the gas was accounted for, but gas temperature was fixed (300 K).

As one can see, heat flow to the gas doesn't change the shape of the emissivity curve, whether it was accounted for or not. Since in the test conditions gas was heated up considerably (Fig.4), heat flow to the gas was relatively small and so, the difference between the first calculation (when heat flow to the gas was ignored) and the second one is also small. However, as the rod temperature goes down, the role of the heat flow to the gas increases and the difference between the results of calculations with and without accounting for heat flow to the gas also increases.

So, one can say, that at high temperatures the errors in the emissivity value determination introduced by uncertainty in the heat exchange with the gas are negligible. At low temperatures gas heating plays more important role, but also not a critical one.

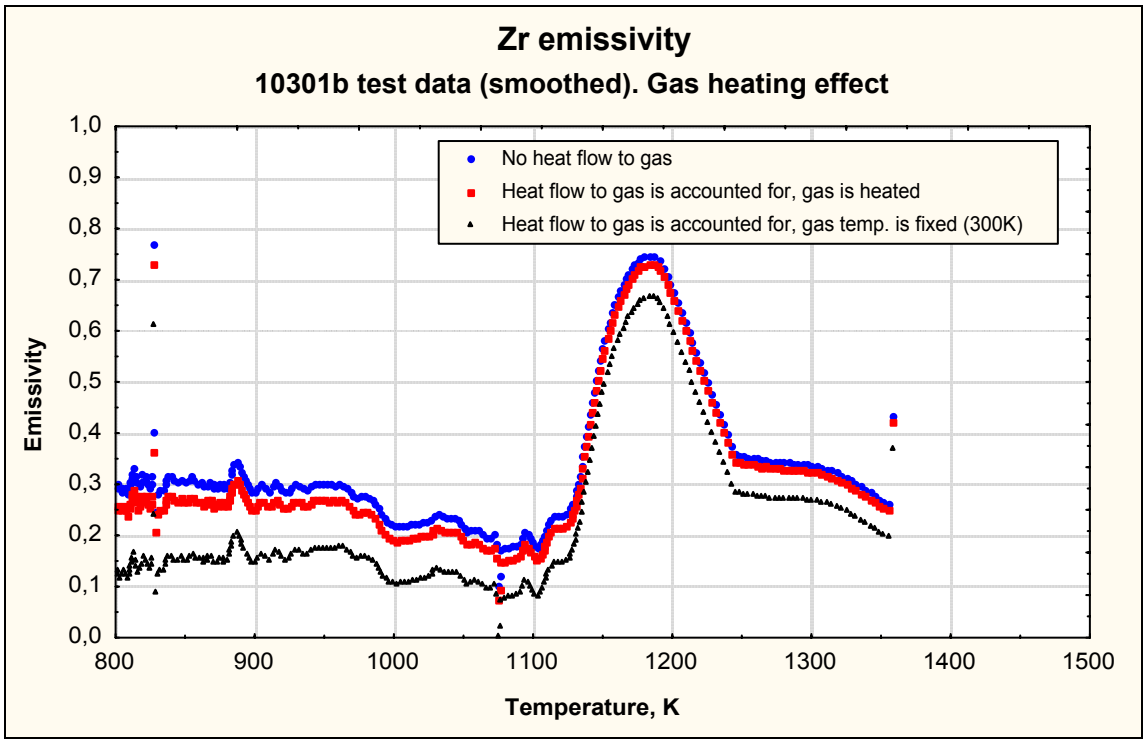

Fig. 10. Effect of heat flow to the gas on the emissivity temperature dependence. No heat flow to the gas (blue points), heat flow to the gas is accounted for and gas is heated (red points), heat flow to the gas is accounted for, but gas temperature is fixed (black points)

3.7. Emissivity fitting curve

The following 9-parameters fitting curve which accounts for maximum in the vicinity of 1180K, small minimum in the vicinity of 1060 K and assumes different constant values at low and high temperature regions was obtained.

$$\varepsilon(T) = p_0 + \frac{1}{2}(p_1 - p_0)\cdot\left(\tanh\left(\frac{T-p_2}{p_3}\right)+1\right)+ \\ +(p_4-p_1)\cdot\exp\left[-\frac{(T-p_2)^2}{p_3^2}\right]-(p_5-p_6)\cdot\exp\left[-\frac{(T-p_7)^2}{p_8^2}\right] \quad (3)$$

$p_0 = 0.25505,$ $p_1 = 0.31783,$ $p_2 = 1184.78,$

$p_3 = 34.5649,$ $p_4 = 0.76264,$ $p_5 = 0.19449,$

$p_6 = 0.10137,$ $p_7 = 1063.73,$ $p_8 = 62.0845.$

The parameters p_0 - p_8 were determined using statistical methods. The fitting curve together with experimental data are presented in Fig.11.

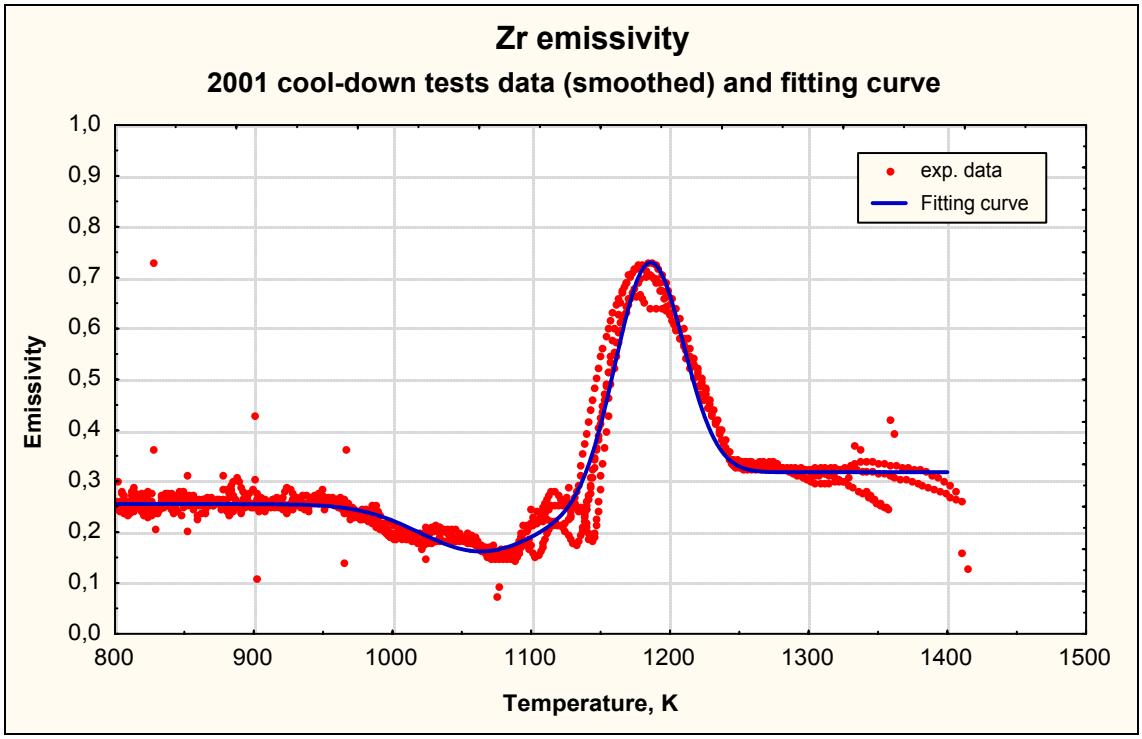

Fig. 11. Zr emissivity experimental data and fitting curve

3.8. Validation of the results obtained

The obtained fitting curve for Zr emissivity was implemented in the working version of S/Q code and then direct simulation of cool-down test was performed. The results of this simulation are presented in Fig.12. As one can see, experimental points and calculated curve practically coincide in the whole temperature interval with the only exception for small deviation at 400 – 500°C, i.e. outside temperature interval of interest.

Thus, from the point of view of the description of heat exchange under severe accident conditions, the results obtained seem to be wholly satisfactory. Better knowledge of other Zr properties, primarily the heat capacity will make it possible to improve them further.

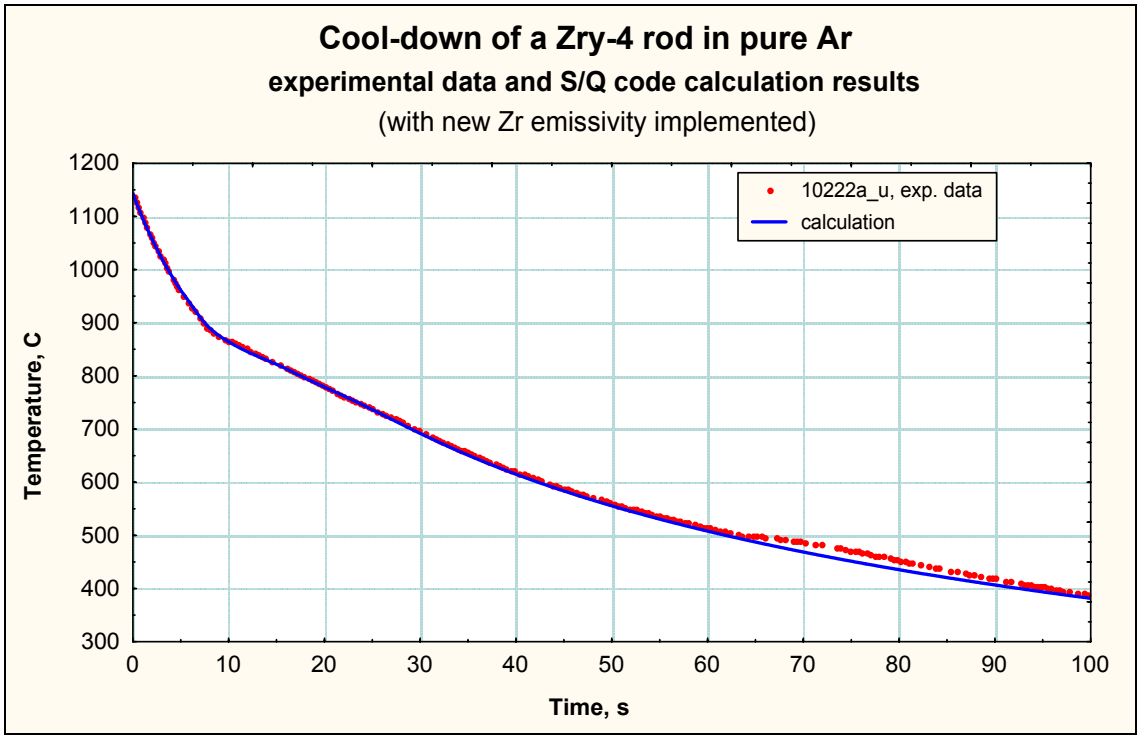

Fig. 12. Cool-down of Zr rod in pure Argon. Experimental data (10222a test) and S/Q code calculation with the new Zr emissivity temperature dependence (eq.(3)) implemented

4. Cool-down tests with oxidised rods

4.1. Test data used

The results of five cool-down tests with oxidised rods were used for the determination of ZrO_2 emissivity coefficient. The initial rod temperatures and thicknesses of oxide, alpha- and beta- layers at the beginning of cool-down phase are collected in Table 2.

As it was already mentioned, in the tests with oxidised rods only one TC located at the middle of rod on its outer surface was used.

Test	L280501	L2805012	L2805013	L2805014	L2805015
Initial temperature, C	1386.8	1334.6	1516.4	1527.3	1454.5
Oxide layer thickness, μm	75	61	598	108	304
alpha layer thickness, μm	88	89	300	105	523
beta layer thickness, μm	576	595	0	549	0

Table 2. Cool-down tests with oxidised rods

4.2. Pre-oxidation process

As it was discussed in subsection 3.3, for the adequate description of the rod cool-down process and determination of the heat flow from the rod surface it is very important to know the temperature distribution inside the rod at the moment of cool-down beginning, the thickness of the layers (i.e. the initial conditions) and also the thermal properties of the rod.

In the case of non-oxidised rod one has stationary conditions at the preheating stage with only one fixed parameter (heat generation rate density) which determines the temperature distribution inside the rod.

In the case of oxidised rod situation is much more complex. The fact is that even if the temperature of the outer surface of the rod remains constant in the course of pre-oxidation, heat generation rate density can not be constant. With growing of the oxide layer the metal layer decreases, and so, in order to keep the total heat generation at the same level, heat generation density should be increased.

Furthermore, all three different layers (oxide, alpha- and beta-) which appear due to oxidation have different heat capacity temperature dependencies. That is why, depending on their thicknesses, they contribute differently to the total rod heat capacity. So, when evaluating heat generation density one has to account for the changing of the total rod heat capacity during oxidation.

With increasing of the oxide layer the radial temperature profile inside the rod changes. The point is that thermal conductivity of oxide is smaller than the metal one almost by an order, and if the temperature of the oxide outer surface is fixed during

oxidation, the metal temperature will grow up as oxide layer grows. (The temperature difference across oxide layer grows with its thickness). Since all the thermal properties are temperature-dependent, changing of the temperature profile will also affect the heat generation rate.

Finally, in the tests under consideration the temperature was not fixed during pre-oxidation, but experienced some variations.

All the above factors make it impossible to evaluate the heat generation rate during pre-oxidation stage of the test simulation 'by hands', with the help of tuning of the S/Q code input data file parameters. That is why a special procedure for the determination of the heat generation rate evolution was developed with the help of MCAD_2000 package. This procedure is briefly described in the following subsection.

4.3. Determination of the heat generation rate density

According to the heat balance equation which describes the heat exchange of the rod at the pre-oxidation stage of the test

$$\rho_\beta(\overline{T_\beta})\cdot C_\beta(\overline{T_\beta})\cdot V_\beta \frac{d\overline{T_\beta}}{dt} + \rho_\alpha(\overline{T_\alpha})\cdot C_\alpha(\overline{T_\alpha})\cdot V_\alpha \frac{d\overline{T_\alpha}}{dt} + \\ + \rho_{ox}(\overline{T_{ox}})\cdot C_{ox}(\overline{T_{ox}})\cdot V_{ox} \frac{d\overline{T_{ox}}}{dt} = Q(t)\cdot(V_\alpha + V_\beta) - F_s \cdot S \tag{4}$$

the heat generation rate $Q(t)$ can be expressed in terms of the average temperatures of the layers, their thermal properties and heat flow from the rod surface $F_s(t)$ (1). In order to do that, the material properties currently used in the S/Q code were introduced in MCAD files and interpolated for the temperature interval of interest.

The time evolution of the layers radii was estimated on the basis of parabolic laws approximation:

external radius: $$r_3(t) = \frac{3}{2} r_3(0) - \frac{1}{2} r_2(t)\,, \tag{5}$$

oxide thickness: $$r_3(t) - r_2(t) = \delta_{ox}\cdot\sqrt{t}\,, \tag{6}$$

alpha layer thickness: $$r_2(t) - r_1(t) = \delta_\alpha \cdot \sqrt{t}\,, \tag{7}$$

Relations (5) - (6) give:

$$r_1(t) = r_3(0) - \frac{2}{3}\delta_{ox}\cdot\sqrt{t} - \delta_\alpha\cdot\sqrt{t}\,, \tag{8}$$

$$r_2(t) = r_3(0) - \frac{2}{3}\delta_{ox}\cdot\sqrt{t}\,, \tag{9}$$

$$r_3(t) = r_3(0) + \frac{1}{3}\delta_{ox}\cdot\sqrt{t}\,. \tag{10}$$

Growth rates of oxide and alpha phases δ_{ox} and δ_{α} were evaluated using the final thickness of the these layers and total oxidation time value.

Temperature distribution inside the cladding in quasi-stationary approximation with accounting for a certain heat generation in the metal phases $Q(t)$ is given by (see [6]):

$$T_2(r,t) = T_{ex}(t) + Q(t)\cdot\left(f_3(r_3(t),t) - f_2(r)\right) \qquad \text{(alpha + beta layers)} \qquad (11)$$

$$T_3(r,t) = T_{ex}(t) + Q(t)\cdot\left(f_3(r_3(t),t) - f_3(r,t)\right) \qquad \text{(oxide layer)} \qquad (12)$$

where

$$f_2(r) = \frac{1}{4}\frac{r_0^2}{\lambda_2}\cdot\left[\left(\frac{r}{r_0}\right)^2 - 2\ln\left(\frac{r}{r_0}\right) - 1\right], \qquad (13)$$

$$f_3(r,t) = \frac{1}{2}\frac{r_0^2}{\lambda_2}\cdot\left\{\left[\left(\frac{r_2(t)}{r_0}\right)^2 - 1\right]\left(\frac{\lambda_2}{\lambda_3}\ln\left(\frac{r}{r_2(t)}\right) + \frac{1}{2}\right) - \ln\left(\frac{r_2(t)}{r_0}\right)\right\}. \qquad (14)$$

In the above equations $T_{ex}(t)$ is the experimentally measured temperature of the rod outer surface at the pre-oxidation stage (Fig. 13), r_0 is internal radius of the cladding; λ_2 and λ_3 are the thermal conductivities of metal and oxide layers, respectively.

The average temperature of the layers is then given by:

$$\overline{T_2(t)} = T_{ex}(t) + Q(t)\cdot F_2(t) \qquad \text{average temperature of alpha + beta layers} \qquad (15)$$

$$\overline{T_3(t)} = T_{ex}(t) + Q(t)\cdot F_3(t) \qquad \text{average temperature of oxide layer} \qquad (16)$$

where

$$F_2(t) = f_3(r_3(t),t) - \frac{2}{r_2(t)^2 - r_0^2}\int_{r_0}^{r_2(t)} f_2(r)\cdot r dr, \qquad (17)$$

$$F_3(t) = f_3(r_3(t),t) - \frac{2}{r_3(t)^2 - r_2(t)^2}\int_{r_2(t)}^{r_3(t)} f_3(r,t)\cdot r dr. \qquad (18)$$

The values $F_2(t)$ and $F_3(t)$ were estimated with accounting for relations (8) – (10).

Finally, the heat generation rate was found from the system of equations (4), (15) – (18):

$$q(t) = \frac{B(t) + D(t)}{A(t)} \qquad (19)$$

where

$$A(t) = r_2(t)^2 - r_0^2 -$$
$$-\left[\rho_1(\overline{T_2(t)})C_1(\overline{T_2(t)})(r_1(t)^2 - r_0^2) + \rho_2(\overline{T_2(t)})C_2(\overline{T_2(t)})(r_2(t)^2 - r_1(t)^2)\right]\cdot\frac{dF_2(t)}{dt} - \quad (20)$$
$$-\rho_3(\overline{T_3(t)})C_3(\overline{T_3(t)})(r_3(t)^2 - r_2(t)^2)\cdot\frac{dF_3(t)}{dt}$$

$$B(t) = \left[\begin{array}{c}\rho_1(\overline{T_2(t)})C_1(\overline{T_2(t)})(r_1(t)^2 - r_0^2) + \rho_2(\overline{T_2(t)})C_2(\overline{T_2(t)})(r_2(t)^2 - r_1(t)^2) \\ + \rho_3(\overline{T_3(t)})C_3(\overline{T_3(t)})(r_3(t)^2 - r_2(t)^2)\end{array}\right]\cdot\frac{dT_{ex}(t)}{dt} \quad (21)$$

$$D(t) = \left[\varepsilon\sigma T_{ex}(t)^4 + \lambda_g Nu\frac{T_{ex}(t) - T_g}{R_{ch} - r_3(t)}\right]\cdot 2r_3(t) \quad (22)$$

Since the emissivity of ZrO_2 was yet to be determined, in relation (22) some preliminary fixed value ($\varepsilon = 0.8$) was used.

The calculated heat generation density is shown in Fig.14.

After some additional iteration procedure the obtained heat generation density was used in the S/Q code input data files for the simulation of the pre-oxidation phase of the test. The initial conditions for the cool-down stage phase simulation were stored in the form of the S/Q code restart file.

Calculated rod surface temperature and thickness of layers at the beginning of cool-down phase are collected in Table 3. As one can see from the comparison of data from Tables 2 and 3, the results of the pre-oxidation phase simulation are very close to the experimentally measured ones. The only exception is the L2805015 test, where the alpha layer thickness was underestimated and as a result, beta layer appears.

In general, the description of the pre-oxidation phase given by the above method and the calculated state of the rod at the beginning of cool-down phase may be considered as adequate to the experimental conditions.

Test	**L2805011**	**L2805012**	**L2805013**	**L2805014**	**L2805015**
Initial temperature, C	**1391.1**	**1338.4**	**1508.0**	**1532.6**	**1457.1**
Oxide layer thickness, μm	**78.5**	**64.1**	**601.3**	**109.4**	**295.0**
alpha layer thickness, μm	**98.0**	**82.4**	**326.0**	**126.7**	**429.2**
beta layer thickness, μm	**570.0**	**604**	**0**	**528.3**	**107.1**

Table 3. Cool-down tests with oxidised rods. Simulation results

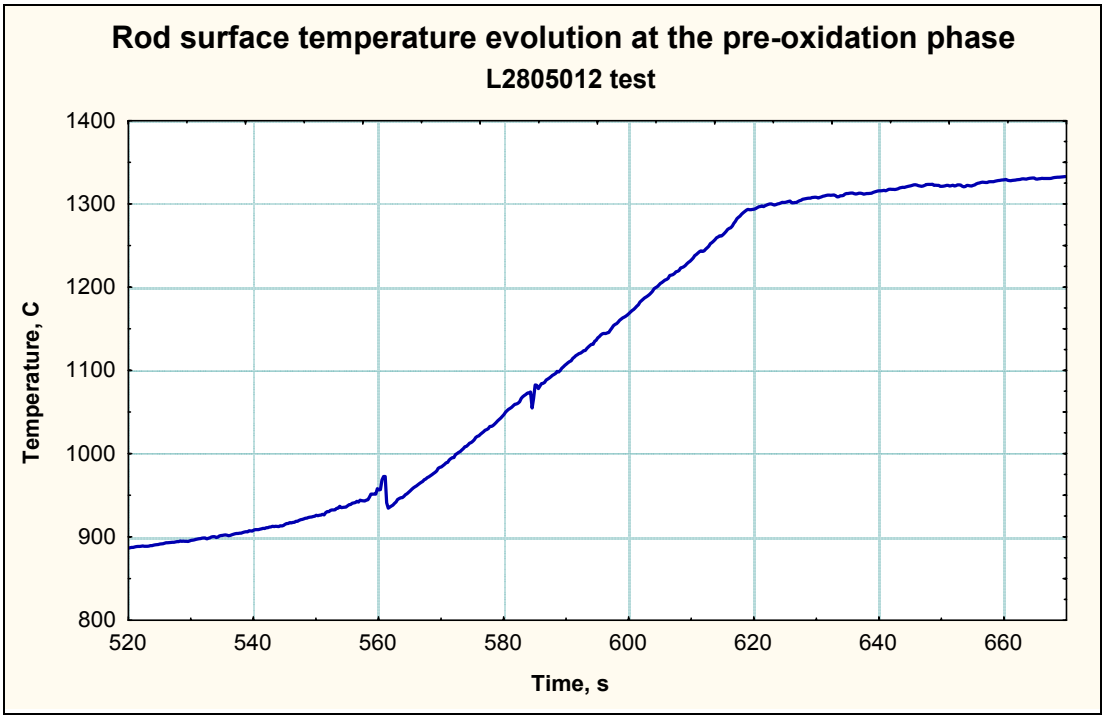

Fig. 13. Rod surface temperature evolution at the pre-oxidation phase of L2805012 test

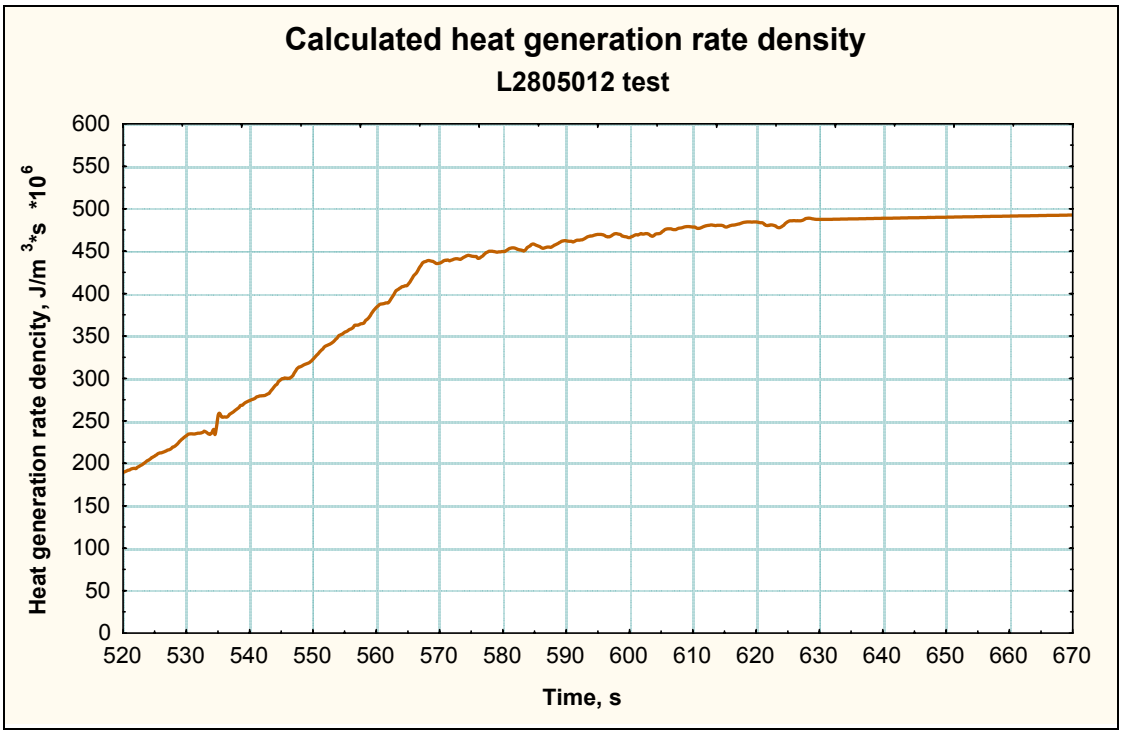

Fig. 14. Calculated heat generation rate density for the L2805012 test

4.4. ZrO_2 emissivity calculation

Smoothing of the temperature curves, simulation of the cool-down phase, determination of the heat flow from the rod surface and calculation of ZrO_2 emissivity coefficient were performed in the same way as in the case of non-oxidised rod. The obtained results are presented in Fig.15.

As one can see, data scattering in the case of ZrO_2 emissivity determination is rather high. The two curves representing tests with thick oxide layers (L2805013 and L2805015) seem to correlate with each other. As for the curves representing tests with relatively thin oxide layers and thick beta layers, they have maximum in the vicinity of 1150 K similar to that in the case of non-oxidised rods. Obviously, here one has an error introduced by overestimation of Zr (beta) heat capacity maximum. Thus, independent measurements of Zr thermal properties is necessary for the successful application of the present method.

The most general conclusion about the obtained results may be the following: ZrO_2 emissivity coefficient is more or less close to the value of 0.6 in the whole considered temperature interval. However, due to high data scattering it is not possible to deduce a fitting curve similar to that in the case of Zr.

In Fig. 16 one can see the comparison of the described cool-down tests data with the emissivity data obtained by optical methods in the work [12] cited in the handbook [9] and in the book [13] cited in the handbook [11].

As one can see, the available ZrO_2 emissivity data contradict each other. The data obtained in the present work are somewhere in the middle between two other data sets. However, one can not make a definite conclusion about the real behaviour of the value of ε on the basis of these data.

Further experiments and calculations are necessary for more accurate determination of ZrO_2 emissivity.

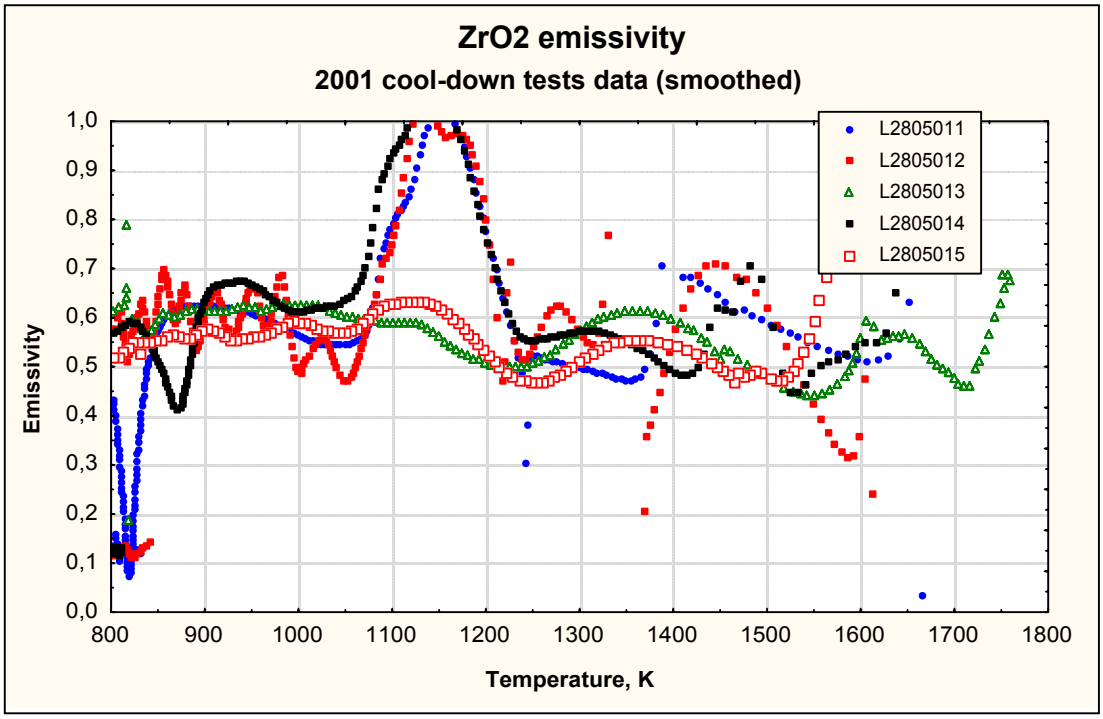

Fig. 15. ZrO_2 emissivity coefficient calculated on the basis of smoothed temperature curves

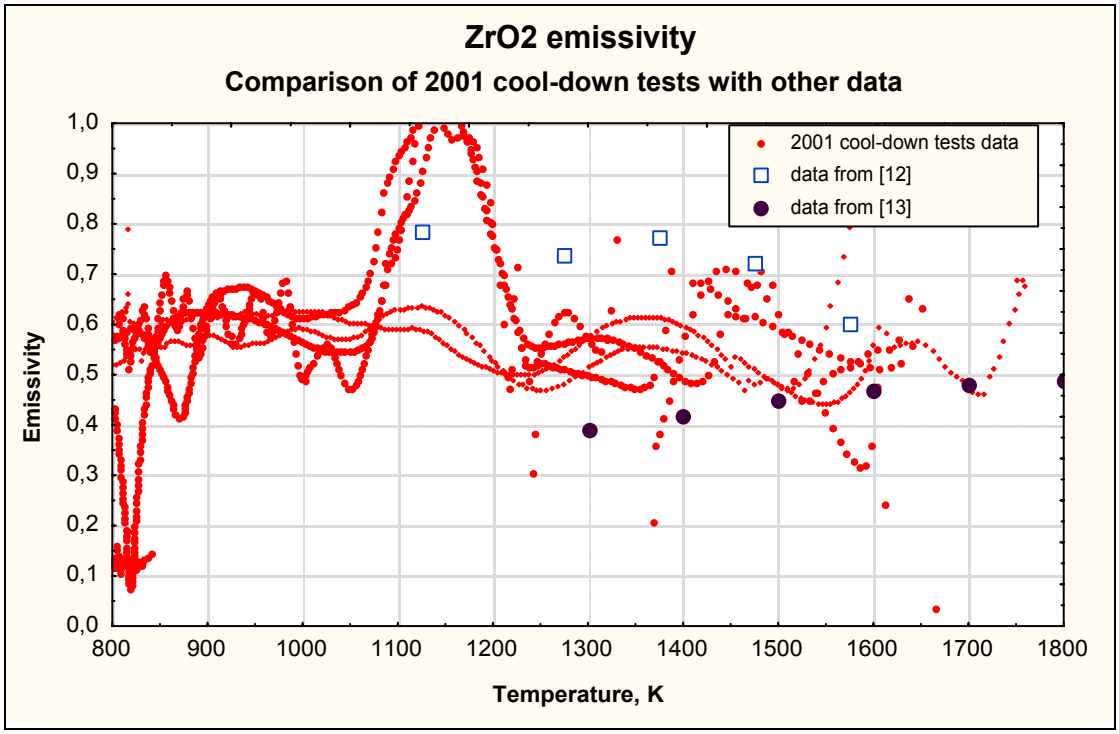

Fig. 16. Comparison of the present cool-down tests data with the results of emissivity determination by optical methods

Summary and conclusions

- The first results of the determination of Zr and ZrO_2 emissivity on the basis of empty rods cool-down tests data were presented. The proposed method is based on the determination of the emissivity using the value of heat flow from the rod surface. The calculation of the heat flow from the rod surface were performed with the help of S/Q code.
- The numerical procedure includes smoothing of the original temperature curves in order to avoid data scattering introduced by small errors in the temperature measurements.
- On the basis of four cool-down tests with non-oxidised Zr rod the value of emissivity was estimated and 9-parameters fitting curve for the its temperature dependence was deduced.
- After the implementation of the obtained fitting curve in the S/Q code the direct simulation of the cool-down test showed very good agreement with the experimental data.
- The method for the determination of the heat generation rate for the pre-oxidation phase simulation by S/Q code was developed.
- Using five cool-down tests with oxidised Zr rod the value of ZrO_2 emissivity was also estimated. However, due to large scattering of the data, no fitting curve was proposed.
- The uncertainty factors which affect the accuracy of the described method are discussed. The effect of the heat flow to the gas was estimated and found to be negligible at high temperatures.
- The errors introduced by deficient knowledge of the thermal properties of the materials involved (especially Zr heat capacity) were found to be rather big.
- Further investigations, including independent measurements of Zr thermal properties are necessary for more accurate determination of Zr and ZrO_2 emissivities.

References

1. SCDAP/RELAP5/MOD2 Code Manual, Volume 4: MATPRO – A Library of Materials Properties for Light-Water-Reactor Accident Analysis. NUREG/CR-5273 EGG-2555. Vol.4. 1990;
2. *P.M.Mathew, M.Krause, M.Dean, M.H.Schankula*, “Emittance of Zircaloy-4 sheath at high temperatures in argon and steam atmospheres”, Proc., Annu. Conf. - Can. Nucl. Soc. (1989), 10th(Vol. 2), 9/12-9/17;
3. *P.M.Mathew, I.M.George*, “Total emissivity of Zircaloy-4 at high temperatures”, Annu. Conf. Proc. – Can. Nucl. Soc. (1996), 17th(Vol. 2). Paper D.3/1, 10 pp.;
4. *I.I.Petrova, V.E.Peletskii, B.N.Samsonov,* “Investigation of the thermophysical properties of zirconium by subsecond pulsed heating technique” High Temp. (2000), 38(4), 560-565;
5. *A.V.Berdyshev, A.V.Boldyrev, A.V.Palagin, V.E.Shestak, M.S.Veshchunov*, SVECHA/QUENCH Code for The Modeling of Reflooding Phenomena in Severe Accidents Conditions. Proceedings of the Ninth International Topical Meeting on Nuclear Reactor Thermal Hydraulics (NURETH-9), paper Log_19 (CD-ROM edition), San Francisco, California, USA, October 1999;
6. *P.Hofmann, V.Noack, M.S.Veshchunov, A.V.Berdyshev, A.V.Boldyrev, L.V.Matweev, A.V.Palagin, V.E.Shestak,* “Physico-Chemical Behavior of Zircaloy Fuel Rod Cladding Tubes During LWR Severe Accident Reflood”, FZKA 5846, 1997;
7. *A.V.Palagin, M.S.Veshchunov, A.V.Berdyshev, A.V.Boldyrev, V.E.Shestak*, “Investigation of an Overheated PWR-Type Fuel Rod Simulator Bundle Cooled Down by Steam. Part II: Application of SVECHA/QUENCH code to the analysis of QUENCH-01 and QUENCH-04 bundle tests”, FZKA 6412, 2001.
8. *S.Konopken, R.Klemm*, North Am. Aviation, Inc., NASA, NBS, and USAF, NASA-SP-31, 505-13, 1963.
9. Thermophysical Properties of High Temperature Solid Materials, Vol.1, *Y.S.Touloukian*, editor, The Macmillan Company, New York, Collier-Macmillan limited, London, 1967.
10. *L.Z.Kriksunov*, A handbook of fundamentals of infrared instruments, Sovetskoye radio, Moscow, 1978 (in Russian).
11. Handbook of Physical Quantities, *I.S.Grigoriev and E.Z.Meilikhov*, editors, CRC Press, 1997.
12. *E.F.Juenke, L.H.Sjodahl*, “Physical and Mechanical Properties: Emittance Measurements”, AEC Fuels and Materials Development Program, GEMP-1008, 1968, pp. 239-242.
13. *V.A.Petrov*, Radiating power of high-temperature materials, Nauka, Moscow, 1969 (in Russian)